The Search for Lyman Alpha Escape from Nearby Starforming Galaxies

by

Brian T. Fleming

A dissertation submitted to The Johns Hopkins University in conformity with the requirements for the degree of Doctor of Philosophy.

Baltimore, Maryland

September, 2013

Abstract

Lyman alpha emission from starforming galaxies is a potential proxy for the ionizing radiation responsible for the re-ionization of the universe at z $\sim$ 6. How this radiation escapes from the neutral hydrogen clouds where stars are formed is not well understood, however. This thesis outlines two separate projects that aim to map Lyman alpha emission from nearby starforming galaxies, and to search for a relation between the Lyman alpha escape fraction and the underlying galaxy environment. The first project combines ultraviolet imaging from the *Hubble Space Telescope* - Advanced Camera for Surveys, and optical spectral data cubes from the *Apache Point Observatory*, to map the Lyman alpha escape fraction in 11 galaxies. The second project is a sounding rocket-borne instrument, the *Far-ultraviolet Off Rowland-circle Telescope for Imaging and Spectroscopy*, developed at the Johns Hopkins University, which utilizes multi-object spectroscopy to probe the Lyman alpha emission, and the far-uv continuum, spectroscopically.

This dissertation has been completed under the supervision of Prof. Stephan R. McCandliss.

ABSTRACT

Primary Reader: Stephan R. McCandliss

Secondary Reader: Paul D. Feldman

Secondary Reader: Timothy Heckman

Secondary Reader: Darrel F. Strobel

Secondary Reader: Harold A. Weaver

Acknowledgments

There are many people without whom this thesis would not have come to be. Most importantly, the confidence the led me to take the leap to Astronomy came from my lovely wife, who has supported my every decision (even the bad ones) and carried the weight of the world for me. I might have got here without her, but my life, and who I am, would not be the same. There are no words to thank her for all that she has given to me.

To my son Martin, who was born in my fourth year and lived his entire life bouncing from parent to parent to grandparent and back while we juggled our graduate school careers. I am so blessed to have a son of such resiliance and adaptability, who has spent a good chunk of my final year, without complaint, building "rockets" in my office while I worked.

To my daughter, Penelope, who I have only just began to get to know, but who has already proven herself to be a loving and remarkably self-reliant little girl. If she had not been such a wonderful baby, born just after we thought we would finish, but before either of us actually did, I do not think we would have made it.

ACKNOWLEDGMENTS

To my Mother-in-law, Ilinca Nicolaescu, who has sacrificed so much, without ever complaining, to help us raise our kids while both working. She has taken care of us both when we have needed it most, and without her we surely would have given up.

To Russ Pelton, who taught me everything from soldering to machining and, while he occasionally lost his patience with some of the equipment, never lost his patience with me.

To Roxana Lupu, who mentored me when I was a wide-eyed youth, Kevin France, who prodded me though my first science project and has been a stalwart mentor throughout, and my mentee, Keith Redwine, who has patiently let me unload everything I know on him in short, incomprehensible bursts.

To the two professors that got me into first physics, and then Astronomy. Professor Chistopher White, who taught three of my most enjoyable courses at IIT and inspired me to take up Physics as a second major, and Professor Julia Kennefick, who took me under her wing for a summer of research and taught me about quasars.

To my sister, Angela, who always amazes me with her ability to do the things that I find hardest. Her courage and creativity has been inspiring me since before I could crawl.

To my parents, John and Nancy, who have supported me unconditionally throughout this endeavor. Their love, care and attention shaped me as a scholar, a parent and a person, and they are still the first people I turn to when I need some advice about life.

ACKNOWLEDGMENTS

To everyone else who has helped me along the way, and there have been many, from my wonderful teachers in high school, to my grandparents and extended family, and to my friends.

Finally, to my advisor, Stephan McCandliss, who taught me when I needed to be taught, let me go when I needed to figure it out on my own, and who never once complained when Martin played on the floor of his office while we talked.

Dedication

Who else but my wonderful wife, Ioana, who has given me so much, and who came with me on this crazy voyage, with love.

Contents

CONTENTS

List of Tables

LIST OF TABLES

List of Figures

Chapter 1

The Search for Lyman Alpha Escape

In the period between $\sim$ 20 minutes and 380,000 years after the Big Bang, the matter content of the universe consisted of a plasma of primarily hydrogen and helium nuclei and free electrons. As the universe expanded, the density and temperature of this plasma dropped to the point that the electrons and nuclei could combine for the first time to form atoms. Astronomers often refer to the age of the universe in terms of a redshift, a scaling of the shifting of light towards longer wavelengths due to the expansion of the universe. By this measure, this combination of nuclei and electrons occurred at a redshift of z $\sim$ 1100. Thus began the Dark Ages - a period in the history of the universe devoid of nuclear fusion processes. It is during this era that the matter in the universe transitioned from being homogeneously distributed

to forming both large- and small-scale structure under the influence of gravity. A theoretical spectrum of objects from this period would show thermal and collisional emission signatures, but no evidence of the fusion processes that happen in stars. The Dark Ages end with the first bursts of hydrogen fusion in the cores of the earliest stars at some time between $12 \leq z \leq 20$ (180 – 380 Myrs after the Big Bang).

The earliest stars and galaxies observed to date are at redshifts ~ 12 [1]. Observations at these high redshifts are marked by the absence of radiation at wavelengths shorter than the rest-frame H I λ 1216 Lyman Alpha (Lyα) line due to the high optical depth of neutral hydrogen to this transition. As the wavelengths emitted shortwards of Lyα are redshifted to 1216 Å by the expansion of the universe, the neutral hydrogen in the universe absorbs those wavelengths and blackens the spectrum. This phenomenon, known as a Gunn-Peterson trough [2], was first observed by Becker et al. (2001) in a quasar spectrum at a redshift of $z = 6.28$, but was not observed in quasar spectra at lower redshift, indicating that the Intergalactic Medium (IGM) was largely ionized at $z \leq 6$, or $\sim$1 Gyr after the Big Bang [3]. Therefore, sometime between 400 Myr – 1 Gyr after the Big Bang ($6 \leq z < 12$) the univserse transitioned from a neutral state back to an ionized state. This period is known as the Epoch of Reionization.

1.1 Reionization of the Universe

How the universe came to be reionized is one of the great mysteries of Astronomy. Cosmic Microwave Background (CMB) polarization measurements by the *Wilkinson Microwave Anisotropy Probe* have indicated the first stages of reionization occurred at a redshift of z $\sim 10.9 \pm 1.4$, corresponding to an age of 430 Myr [4,5]. Quasars, which are efficient creators of H I ionizing radiation (Lyman Continuum (LyC), $\lambda \leq 912$ Å), were the natural candidates as the source of this ionizing radiation [6], however quasar counting studies show that the number density of quasars falls short of reionizing the universe by nearly an order of magnitude [7, 8]. It is possible that a large number of small Active Galactic Nuclei (AGN) make up for this shortfall, however they have not been observed [9].

A second source of LyC photons is the first stars in the earliest galaxies [10, 11]. Mathematical models of star-formation in the early universe have predicted that, given the proper initial mass function (IMF), enough hot stars could form by z ~ 11 to reionize the universe [12, 13], however the first stars form deep in dense, neutral clouds having large H I column densities ranging from $N_{HI} \sim 10^{21}$ – 10^{24} cm^{-2} [14]. A neutral hydrogen column density of only $N_H \sim 10^{17}$ cm^{-2} is the equivalent of a $\tau_{912} \sim 1$, therefore the amount of LyC photons escaping from a uniform star-forming region of typical N_{HI} will be suppressed by many orders of magnitude.

There have been a number of mechanisms proposed that would aid in the escaping of LyC photons. The high star formation rate (SFR) and hot star fraction in the

early universe would undoubtedly lead to a high rate of supernovae that could drive superwinds and clear out bubbles in the interstellar medium (ISM) [15,16]. Starburst driven galactic winds appear to be a ubiquitous in galaxies with high star-formation densities [17, 18]. The natural clumpiness of the ISM could also lead to either lower LyC escape fractions (f_{esc}) [19] or higher f_{esc} [9, 20] depending on the density and clumping factor. Halo mass, metalicity, morphology, star formation rate, and many other factors all play a role in the determination of f_{esc}.

Measurements of f_{esc} have spanned redshifts from ~ 0.02 – 3 [15, 21–28]. These studies paint a confusing picture of f_{esc}, with values ranging from $f_{esc} = 0 \rightarrow 1$. Studies at redshifts of z $\sim$ 3 are most common because at these redshifts the Lyman limit ($\lambda \leq 912$ Å) is shifted into the bandpass easily observable from optical ground-based telescopes. By imaging galaxies using a series of filters, Astronomers determine the location and strength of the Lyman break by searching for a marked drop in flux between sets of shorter and longer wavelength filters. Galaxies identified in this manner are known as Lyman Break Galaxies (LBGs), and f_{esc} can be determined by comparing the measured flux shortward of the Lyman limit to that predicted by the images taken at rest-frame wavelengths $>$ 912 Å. Steidel et al. (2001) measured $f_{esc} \geq 0.5$ for a sample of galaxies at z $\sim$ 3 by measuring the flux in images taken through filters that probe opposing sides of the Lyman break ($\sim$ 912 Å), however similar studies at the same redshifts have derived lower values, with only $\sim$ 10% of galaxies at z $\sim$ 3 exhibiting large f_{esc}. In the z $\sim$ 0.02 universe, measurements have

ranged from $f_{esc} \sim 0 - 0.2$. New instruments with spectral coverage below the Lyman limit would enable the spatially resolved study of f_{esc} from local galaxies down to a z $\rightarrow$ 0 [29]. For redshifts below a few hundred km s^{-1}, blending with the Milky Way H I absorption shadow complicates LyC measurements.

Numerical simulations have also varied in their conclusions as to the effect of the environment on f_{esc} [30, 31]. It has been shown that higher mass galaxies both decrease f_{esc} due to a greater amount of neutral gas and a tendency for larger gas clumps [32], and increase f_{esc} due to higher star formation and collisional ionization rates [33, 34]. The irregularity of the ISM in very low mass galaxies, however, leads to extreme clumpiness and higher f_{esc}, making dwarf galaxies the potential dominant source of LyC photons in the early IGM [35]. It is expected that the average f_{esc} should generally increase with redshift as the abundance of small dwarf galaxies with high star formation rates increases, but some studies have shown that a lower star-formation efficiency at high redshift would decrease f_{esc} for a high-z galaxy relative to a low-z analog [36].

The current state of the science is that f_{esc} must be ~ 0.2 for low mass galaxies in order to complete reionization by z $\sim$ 7 [34]. This assumes a certain number density of dwarf galaxies at high redshifts. Analysis of the *Hubble Space Telescope* (HST) - Ultra Deep Field suggests that galaxy formation must extend beyond z $\sim$ 12 in order for starforming galaxies to be the main driver, therefore extensive study of high-z galaxies by the *James Webb Space Telescope* (JWST) will be necessary to

fully understand this complex problem [37].

Shull et al. (2012) [34] express the critical star formation rate density, ρ_{cr}^{SFR}, required to maintain the universe in a fully ionized state as

$$\rho_{cr}^{SFR} = \left(\frac{C/3}{f_{esc}/0.2}\right)\left(\frac{0.004}{Q_{LyC}}\right)\left(\frac{1+z}{8}\right)^3 \; M_{\odot} yr^{-1} Mpc^{-3}, \tag{1.1}$$

where C represents the density clumpiness factor ($< n_{HII}^2 > / < n_{HII} >^2$) and Q_{LyC} the LyC emission rate (units of 10^{63} $M_{\odot}$ yr^{-1}). They predict that at a redshift of $z \sim 7$ and a clumping factor of $C = 3$, $f_{esc} \sim 0.2$ in order to maintain the critical star-formation rate density.

While simulations are capable of modeling starforming galaxies at $z \geq 10$, increasing H I opacity at redshifts ≥ 3 make direct observations of LyC escape practically impossible [38]. Despite the diversity of models available, with a measurement of just a few factors, such as SFR and mass, a reasonable estimation of an average f_{esc} can be made when direct measurements are impossible [30, 31]. Observational characterization of the LyC properties of the earliest galaxies will therefore be carried out by measuring observable parameters and using those to estimate f_{esc}.

1.2 Lyman Alpha Escape

The Lyα transition of hydrogen (H I λ 1216 Å), and the nearby fuv-continuum, have been suggested as a potential proxy for LyC at high redshifts [39]. At the

low densities typical in neutral gas clouds, each LyC photon that ionizes a hydrogen atom in the ISM should be totally absorbed, but then replaced by a well-defined spectrum of hydrogen electronic transitions from n = $\infty \rightarrow 0$ when the electron and proton recombine. For a temperature of 10^4 K and density of $n_H \sim 10^2$ cm^{-3} in an optically thin regime, known as "Case A" recombination, the ratio of Lyα to Balmer alpha (Hα, λ6563) to Balmer beta (Hβ, λ4861) is 32.7 : 2.86 : 1 [40]. This assumes that all photons generated in the recombination cascade escape. In the $N_{HI} \sim 10^{21}$ nebulae where stars tend to form, however, the higher order Lyman series lines have a probability of interacting with ground-state neutral H I of $\sim$ unity. Therefore, all of the Lyman series photons will undergo a continuous process of absorption by H I, and will either scatter or be converted to a set of lower energy photons via a separate allowed series of transitions to the ground state.

Hydrogen excited into the n=3 state has a probability of a transition from the $3^2P \rightarrow 1^2S$ and the release of a Lyman β photon of 0.882, while the $3^2P \rightarrow 2^2S$ transition has a probability of 0.118. Thus after an average of $\sim$ 9 scatterings, every Lyβ photon will be converted to an Hα photon and two-photon continuum ($2^2S \rightarrow 1^2S$) (Fig. 1.1). In this regime, where we assume that all Lyman series photons at energies higher than Lyα are converted into lower lines, Lyα:Hα:Hβ= 23.1 : 2.87 : 1. This is known as "Case B" recombination. In the absence of collisional excitation, knowledge of the intrinsic luminosity of any individual H I spectral line will yield the intrinsic luminosity of the entire H I spectrum (Fig. 1.2). As the only mechanism for

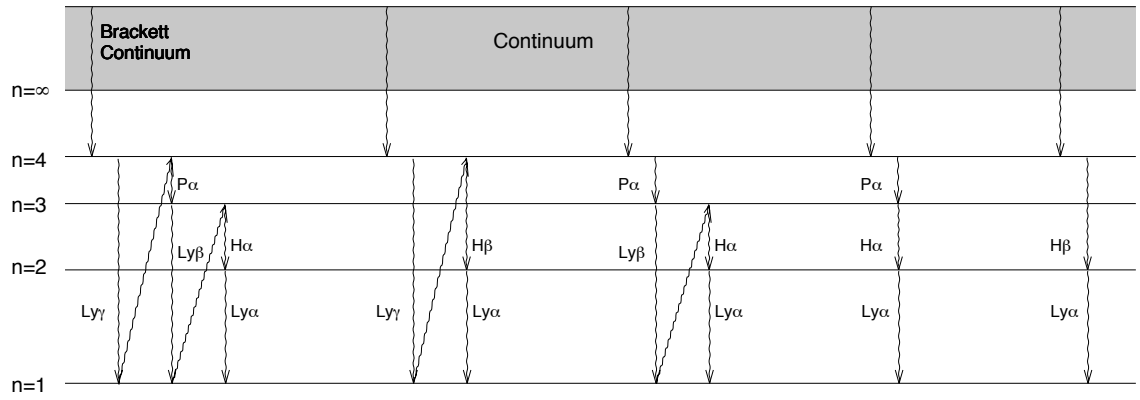

Figure 1.1: A schematic cartoon showing that in a Case B environment which is optically thick to Lyman transitions, all recombination cascades ultimately produce one Balmer series transition plus one Lyα photon ($2^2\mathrm{P} \rightarrow 1^2\mathrm{S}$), or 2 photon continuum ($2^2\mathrm{S} \rightarrow 1^2\mathrm{S}$).

H I ionization at low densities is the abosrption of LyC radiation, this is therefore a measure of the number of LyC photons that fail to escape from a nebular region.

In the era of JWST, the Lyα emission line is likely to be the strongest, and potentially the only, emission line detectable in most z $\geq$ 10 galaxies due to the low metalicity. The power of recombination theory enables a host of diagnostic tools that will greatly illuminate our understanding of the early universe. Measurements of Lyα at high z can serve as probe of the SFR [41, 42], metalicity [43] and evolution [44, 45] of early galaxies, which ultimately feeds back into the models of LyC escape and the reionization of the universe.

Unfortunately, the mechanisms for Lyα photons to escape from galaxies is as complex as it is for LyC photons, and the escape pathways are not necessarily the same. The interaction cross section at the line core for Lyα in a neutral cloud is $\sim$

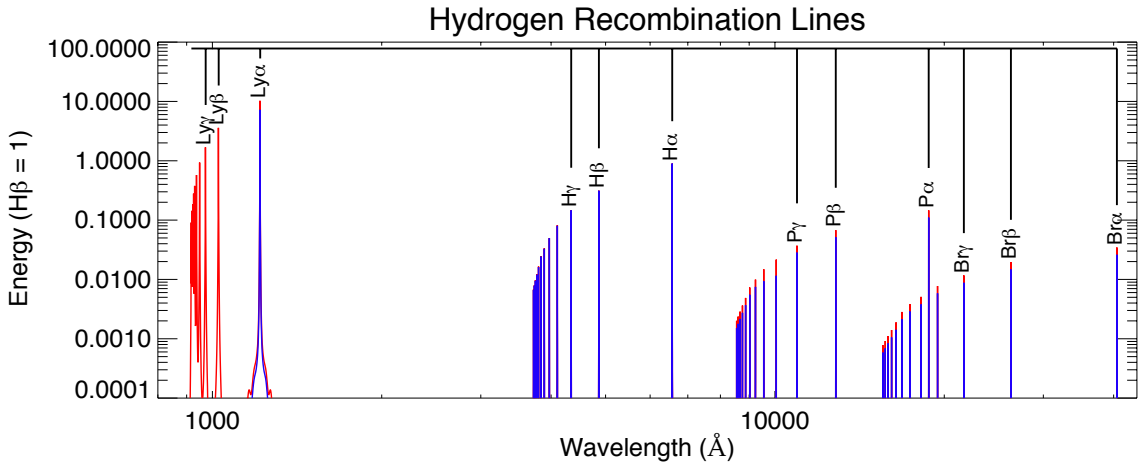

Figure 1.2: Emission spectra of hydrogen in the Case A (red) and Case B (blue) recombination theories. Spectra are normalized to the integrated Hβ intensity = 1

10^4 times greater than for radiation at 912 Å, virtually ensuring that in any typical star formation region, no unscattered Lyα photon will ever escape into the ISM, to say nothing of the IGM. Unlike LyC, Lyα photons are not destroyed upon absorption, but instead undergo resonant scattering until doppler shift random walks the photon into the line wings where the cross section is lower. This process is aided by velocity gradients in a multi-phase medium, as Lyα emitted from H I at a certain velocity appears red- or blueshifted to H I at a different velocity [46–48].

The longer path length for Lyα escape complicates the comparison of the escape of Lyα photons ($f_{Ly\alpha}$) to f_{esc}. It is intuitive to assume that the probability of a resonantly scattering Lyα photon encountering dust and being destroyed would scale with path length. In a clumpy medium, however, it is possible that Lyα photons that escape from their parent cloud will tend to reflect off of other dense, neutral

clouds and therefore will encounter a lower total dust column than continuum photons [46, 49]. This would result in narrower Lyα line profiles and a higher Lyα equivalent width (EW), which have been observed in some targets, especially at high redshift [41, 44, 50, 51].

Aside from the resonant scattering of Lyα, the other mechanisms that govern f_{esc} also contribute to $f_{Ly\alpha}$. Star-formation driven superwinds, a strong ionizing continuum [44] and a multiphase medium all contribute towards the final determination of $f_{Ly\alpha}$ and f_{esc} in galaxies. A simple formula relates the Lyα luminosity to $f_{Ly\alpha}$ and f_{esc} [52],

$$L_{\mathrm{Ly}\alpha} = \frac{2}{3} Q (1 - f_{esc}) f_{Ly\alpha}, \tag{1.2}$$

where Q is the total LyC emission rate. If $f_{Ly\alpha}$ and f_{esc} are each governed by independent processes, then $\mathrm{L}_{\mathrm{Ly}\alpha}$ will be inversely proportional to f_{esc} for a given Q. If they are related, however, and $f_{Ly\alpha} \sim f_{esc}$, then $\mathrm{L}_{\mathrm{Ly}\alpha}$ is a quadratic function of Q with a peak at $\frac{1}{6}$Q for $f_{Ly\alpha} = f_{esc} = 0.5$. If Ly$\alpha$ is to be used as the principal diagnostic spectral line in the high redshift universe, then it is critical to establish the escape parameters, and then ultimately to relate $f_{Ly\alpha}$ to f_{esc}, in order to determine if the earliest galaxies are responsible for the reionization of the universe.

1.3 The Search

This thesis seeks to determine $f_{Ly\alpha}$ from nearby star-forming galaxies and relate it to the local environment. This problem is addressed by two separate, but complementary, projects. The first is a *Hubble Space Telescope* - Advanced Camera for Surveys/Solar Blind Channel (*HST*-ACS/SBC) + *Apache Point Observatory* (APO) survey of 12 targets to search for Lyα escape on $\sim 1''$ scales (Chapter 2). The second project is a sounding rocket-borne fuv instrument designed specifically to measure Lyα emission from galaxies with a heliocentric velocity $\geq$ 1500 km s^{-1} (another means of expressing redshift, in this case z $\approx$ 1500 km s^{-1} $\approx$ 0.005) using multi-object spectroscopy (Chapters 3 and 4). In both projects, the emphasis is on targeting specific sightlines into galaxies in order to understand how $f_{Ly\alpha}$ relates to the local environment. These low redshift observations are critical to understanding the escape mechanisms, as f_{esc} and $f_{Ly\alpha}$ can vary by an order of magnitude depending on the observation sightline [33]. This research aims to increase the understanding of Lyα escape, and to aid in the selection of future targets for LyC observation, which is discussed briefly in Chapter 5.

Chapter 2

Lyα Escape from 0.02<z<0.045 Starforming Galaxies with *HST* Photometry and Optical Spectral Mapping

2.1 Introduction

The investigation of Lyα escape from local galaxies at z $\leq$ 0.05 is complicated by two factors; the lack of fuv sensitive spectrographic instruments, and the difficulty of separating Lyα emission native to a target galaxy from the Milky Way absorption shadow and the bright Lyα emission from the geocorona. At present, the only in-

strument capable of a spectroscopic measurement of Lyα at z $\leq$ 0.15 is the *Cosmic Origins Spectrograph* (COS) on the *Hubble Space Telescope* (*HST*), however the 2.″5 diameter spectrograph aperture provides limited grasp, the product of the effective area (cm^2) and solid angle observed (AΩ), for the study of extended objects. The *Johns Hopkins University* sounding rocket group recently developed the Far-ultraviolet Off Rowland-circle Telescope for Imaging and Spectroscopy (FORTIS) with the goal of providing increased AΩ to carry out these essential measurements (Chapter 3). The experimental nature of the instrument, and the limited exposure time of a sounding rocket flight, necessitates that we approach the problem of Lyα escape through other means as well.

The majority of $f_{Ly\alpha}$ studies in the literature focus on z $\sim$ 3 sources where Lyα is redshifted into the optical bandpass. While these studies have produced useful data that has shaped the understanding of $f_{Ly\alpha}$, they provide only limited angular resolution for studying the variation of escape properties across a single galaxy. Lyα escape is expected to show a significant variation on local scales because of its sensitivity to local environmental properties, such as the column density, velocity gradients, and dust. In recent years, multi-object spectrographs and spectral mapping techniques have enabled the study of the environment of extended objects in unprecedented ways, showing that point-source observations of extended objects often mask a larger story [53].

In this chapter, we present the results of a combined *HST* Advanced Camera

for Surveys - Solar Blind Channel (*HST*/ACS-SBC) and *Apache Point Observatory* Dual-Imaging Spectrograph (*APO*-DIS) study of 12 starforming galaxies at redshifts of $0.02 < z < 0.045$. We extract the Lyα flux from each galaxy using innovative photometric techniques, and compare it to optical 3-D spectral data cubes in order to calculate $f_{Ly\alpha}$. Using the well established spectral diagnostics in the optical bandpass, we also relate $f_{Ly\alpha}$ to other observable properties of these starforming galaxies in an attempt to understand the mechanisms that govern escape.

2.1.1 Lyα Escape Candidates

The sample of low redshift star-forming galaxies was selected from the merged *Galaxy Evolution Explorer* (*GALEX*) + *Sloan Digital Sky Survey* (SDSS) catalogs. The selection goal was to produce a sample of targets spanning the morphological spectrum (Sa, Irregular, Blue Compact, etc) within the redshift range $0.021 \leq z \leq 0.043$, with *GALEX* FUV fluxes within a factor of 2 of each other. The galaxy designation, morphological type, coordinates, redshift, and total *GALEX* FUV channel flux in units of erg cm^{-2} s^{-1} Å^{-1} are given in Table 2.1. SDSS images are presented in Figure 2.1.

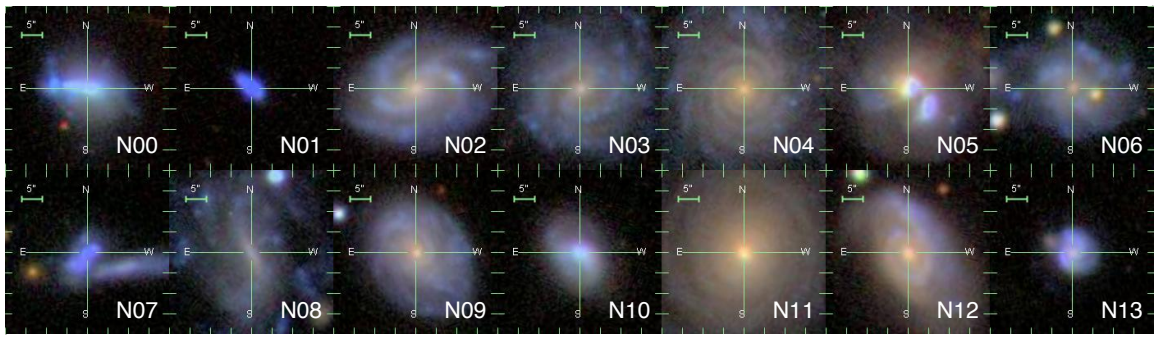

Figure 2.1: $40'' \times 40''$ images of the HST/ACS-SBC targets from the SDSS.

2.2 Lyα Measurements from HST/ACS

The *HST*/ACS-SBC has a set of three long-pass filters (F125LP, F140LP, and F150LP) with sharp absorption edges at the short edge of their coverage region. These are nested filters, with the total throughput determined by the compounding of the transmission of the individual filter materials (CaF_2, BaF_2 and SiO_2). The nested profiles make it possible to make synthetic bandpass filters by subtracting adjacent filters, making "blue" (ACS-b), "green" (ACS-g) and "red" (ACS-r) images (Fig. 2.2). The technical properties are given in Table 2.2. The sensitivities in Table 2.2 are used to convert the raw count rates in the ACS images into fluxes with units of erg cm^{-2} s^{-1} Å^{-1}. At the redshifts of the science targets, Lyα is located in the ACS-b bandpass, ACS-g will be almost entirely continuum emission, and ACS-r will contain only a handful of metal lines.

The flux threshold for target selection was originally established for a *Far-Ultraviolet*

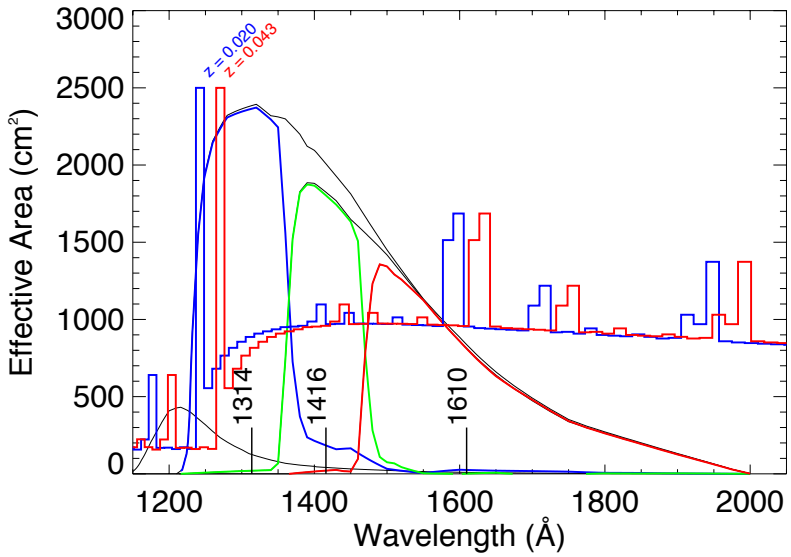

Figure 2.2: The Effective Area curve for the F125LP, F140LP and F150LP HST/ACS-SBC filters. A model FUV emission spectrum is overlaid showing the range of redshifts in the sample. Prominent spectral lines in the region include C IV $\lambda\lambda$ 1548, 1551, O III] $\lambda\lambda$ 1660, 1608 and C III] λ 1909.

Project Balmer Observations

Target	Morphological Type	RA HH:MM:SS	DEC DD:MM:SS	Redshift	f_{1516} (10^{-15} erg cm^{-2} s^{-1} Å^{-1})
N00	BCG	13:25:54.0	+57:15:15.9	0.021	15
N01	BCG	13:59:51.0	+57:26:22.9	0.034	8
N02	S	12:52:03.5	+51:40:47.4	0.027	12
N04	Sbc	9:22:38.1	+60:51:56.9	0.026	10
N05	Sdpec	16:11:40.6	+52:27:24.7	0.029	13
N06	Irr	17:22:05.2	+59:06:48.3	0.031	9
N07	BCG	13:07:28.2	+54:26:50.8	0.033	8
N08	SBc	9:23:08.5	+50:50:08.0	0.026	9
N09	S	13:48:13.1	+54:47:50.1	0.026	7
N10	BCG	10:43:51.5	+55:45:42.9	0.026	6
N12	S	11:18:27.6	+65:01:57.5	0.033	7
N13	BCG/S	13:21:09.0	+59:06:05.5	0.043	7

Table 2.1: Lyα escape candidate target list

Spectroscopic Explorer (*FUSE*) proposal to measure the LyC escape properties. While that proposal was funded, *FUSE* stopped functioning before data could be obtained. The *GALEX* FUV and nuv images were used to determine the slope of the uv continuum based on the relation

$$\beta = \frac{log(f_{1516}/f_{2267})}{log(1516/2267)}, \tag{2.1}$$

HST/ACS-SBC Filter Properties

Band	Sensitivity	λ_p	λ_{rms}	λ_{FWHM}
S_{131}	2.12e+16	1314.	68.	130.
S_{142}	1.40e+16	1416.	41.	105.
S_{161}	2.27e+16	1610.	116.	170.

Table 2.2: HST/ACS-SBC Bandpass Sensitivities. Units of sensitivity are (counts s^{-1})/(ergs cm^{-2} s^{-1} $Å^{-1}$)

where 1516 Å and 2267 Å are the pivot wavelengths of the *GALEX* FUV and NUV bandpasses. The estimated NUV continuum flux is then given as

$$f_\lambda = f_{1516}\left(\frac{\lambda}{1516}\right)^\beta. \tag{2.2}$$

The FUV brightness of the chosen targets was such that with sufficient signal-to-noise, images could be obtained in all three filters within a single orbit. The F125LP filter is not sensitive to geocoronal Lyα, however geocoronal O I λ 1304 and 1356 Å could contaminate the images, therefore the observation sequence was set so that F125LP exposures occurred during shadow time on orbit. Each image had an exposure time of $\approx$ 2700 s. The F125LP - F140LP "blue"-band images for four targets are presented in Fig. 2.3, and all targets are presented in Appendix A.

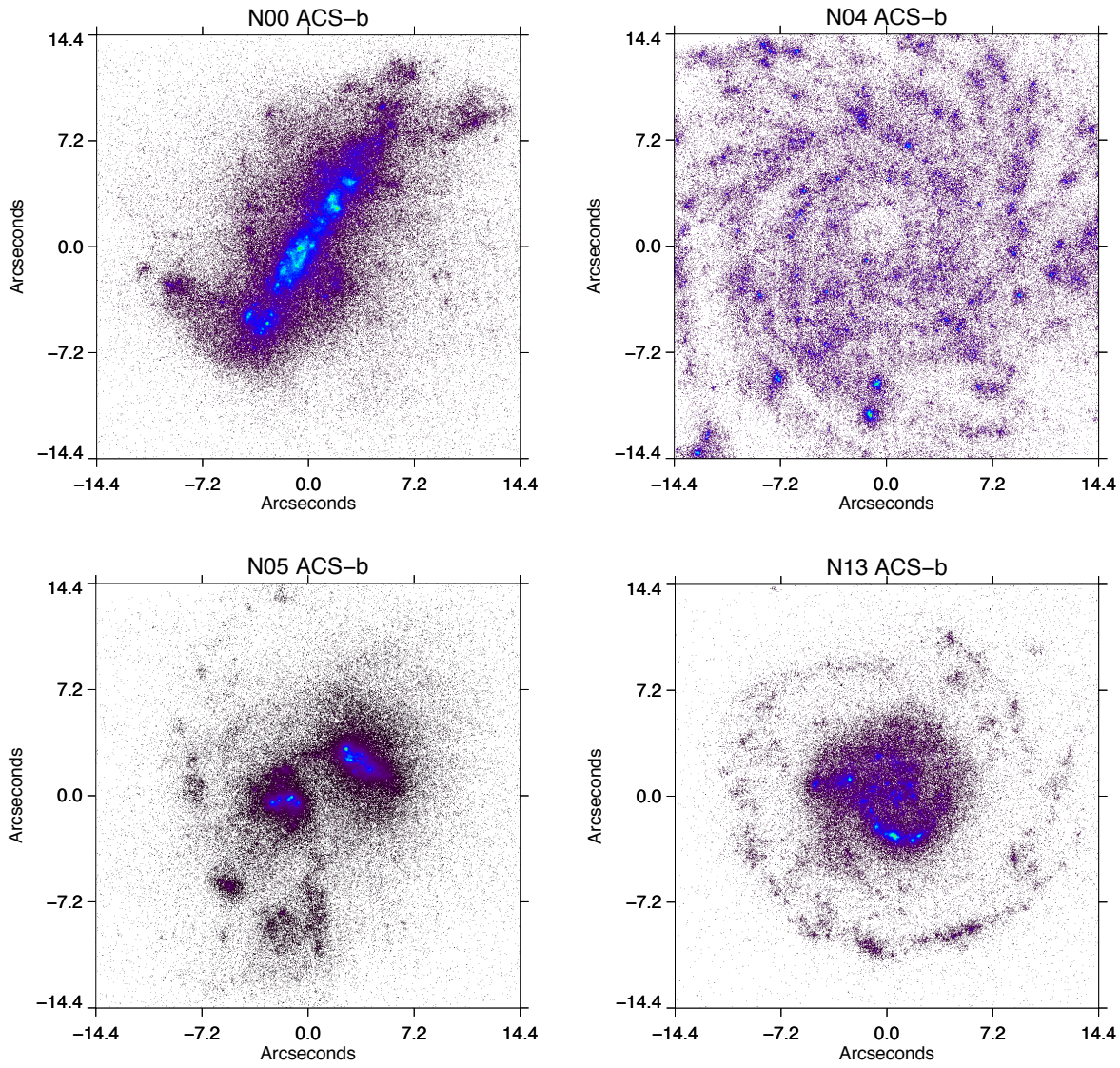

Figure 2.3: ACS-b images for N00, N04, N05 and N13. All other images can be seen in Appendix A.

2.2.1 Extracting Lyα

The spectral energy distribution of the FUV continuum can be expressed in terms of a power law with the slope represented by β. Starburst99 [54] population synthesis models were constructed for instantaneous bursts of star-formation with a Salpeter IMF over time ranges from 1-300 Myr ago, with each "track" consisting of age intervals of 1 Myr. When the continuum slopes, β_{bg} β_{gr} from these model tracks are compared to the βs calculated from the HST/ACS images, we find that there are a number of pixels that are "impossibly blue", meaning that no model spectral energy distribution (SED) can fit the extreme $\beta_{bg} <$ -4, and other pixels that are "impossibly red" - where no model can fit the extreme $\beta_{gr} > 4$. In the presence of well-behaved slopes between the other channels, we associate the "impossibly blue" pixels with Lyα emission, and the "impossibly red" pixels with a variety of metal lines in the F150LP filter, such as C IV $\lambda\lambda$ 1548 – 1550, and potentially continuum absorption in the blue band.

Extracting only the excess flux using this method would likely only extract the extreme Lyα equivalent widths and neglect the majority of the true Lyα emission. From a statistical perspective, if the properties of the entire galaxy were condensed into a single pixel, then conceivably the SED should fit the continuum level in both the red and green channels, as the high energy level metal emission lines should ultimately damp out relative to the continuum. At this point, the amount of Lyα flux should simply be equivalent to the blue excess relative to the flux predicted by β_{gr}. The excess (or deficit) of flux in the blue channel is then given as the blue

channel monochromatic flux (F_{1314}) minus the expected blue channel monochromatic flux calculated from the green channel monochromatic flux (F_{1416}) and power-law slope, β_{gr},

$$\Delta F_{1314} = F_{1314} - F_{1416}\left(\frac{1314}{1416}\right)^{\beta_{gr}} \tag{2.3}$$

where F_{1314} and F_{1416} are in units of erg cm^{-2} s^{-1} Å^{-1}. The 1314 and 1416 represent the λ pivot point for each filter. When this relation is positive, it indicates excess flux in the blue channel, which we interpret to be due to Lyα. The strength of the Lyα line can then be computed by first converting ΔF_{1314} back to a count rate using the ACS-b bandpass sensitivity (S_b). Assuming that all of the excess counts in the ACS-b band are due to Lyα emission, then the Lyα flux, $F_{\mathrm{Ly}\alpha}$, is simply the number of excess counts multiplied by the energy of a Lyα photon divided by the effective area at the redshifted Lyα wavelength. This is defined as the Lyα sensitivity, $S_{\mathrm{Ly}\alpha}(z)$ and is given as

$$S_{\mathrm{Ly}\alpha}(z) = \frac{hc}{\lambda(1+z)A_{eff}(\lambda_{obs})}, \tag{2.4}$$

which leads to

$$F_{\mathrm{Ly}\alpha} = \frac{S_{\mathrm{Ly}\alpha}(z)}{S_b}\Delta F_{1314}. \tag{2.5}$$

This relation should yield the net total Lyα flux from the target.

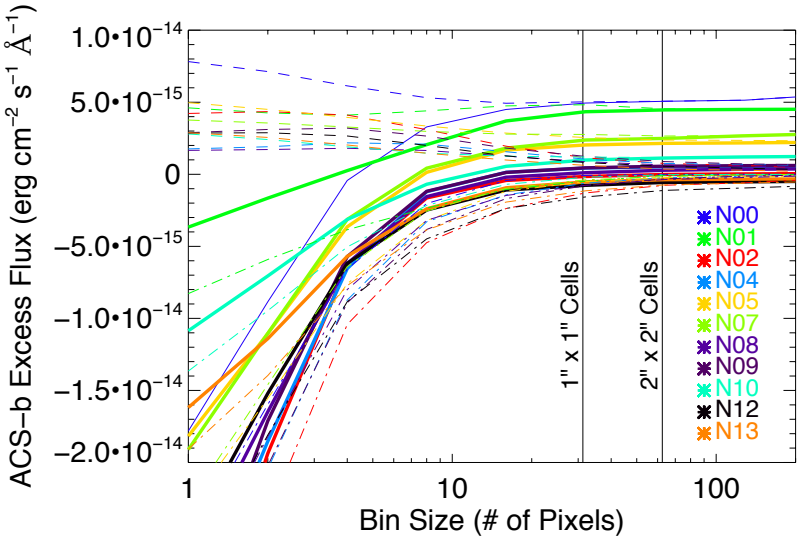

Figure 2.4: The total derived ACS-b image excess flux relative to the bin dimension for each galaxy. The vertical lines represent 1 square arcsecond and 4 square arcsecond cell sizes. Dashed lines is the total flux in emission, and dash-dot the total continuum deficit.

This analysis could be conceivably run on every pixel individually, however it would be potentially susceptible to line emission in the ACS-r band, and the stringent signal-to-noise cut that would be necessary to get proper statistics would neglect the majority of diffuse Lyα emission. We find that the net total Lyα flux within a region begins to stabilize on scales of 10 × 10 ACS pixels, which is a cell size $\sim$ 0.″32 × 0.″32 (Fig. 2.4). Around 1″ × 1″ cell sizes, the net total Lyα flux is mostly flat with respect to the bin size. To achieve good statistics, we require that every cell contains 1000 counts arcsecond^{-2} in the raw long-pass filter F125LP image, or roughly 1 count pixel^{-1} for 1″ × 1″ cell sizes, and 0.5 counts pixel^{-1} for 2″ × 2″ cell sizes.

2.2.1.1 Continuum Deficit

In some cases, ΔF_{1314} is negative, indicating that there is a net deficit of continuum flux in the blue band with respect to the extrapolation from the g-band. It is possible to interpret this deficit in terms of an absorption of the continuum emission around 1216 Å by neutral hydrogen. However, unlike emission, continuum absorption is a non-linear process where the absorption equivalent width (EW) will scale according to the curve of growth. Since we are concerned primarily with the fate of Lyα photons generated by recombination processes, and not resonantly scattered $\sim$ 1216 Å continuum photons, the cells with negative ΔF_{1314} must be counted against the total Lyα emission for the galaxy as a whole. Therefore, when we calculate the total Lyα flux from the sum of emission from all cells, we first total the ΔF_{1314} from all cells before multiplying by $S_{Ly\alpha}(z)/S_b$ and determing $F_{Ly\alpha}$.

The total flux deficit from the cells for each galaxy is represented by the dot-dashed lines in Figure 2.4, while the total positive ΔF_{1314} is represented by the dashed lines. In both cases, smaller cell sizes increases both the positive emission and the flux deficit, however the net galaxy ΔF_{1314} is roughly constant down to $\sim$ 10 pixel bins. This is the result of smaller cells separating regions of Lyα emission and continuum absorption. The total energy budget remans balanced.

This presents a conundrum when determining the Lyα luminosity and escape fraction for different sightlines. For cell sizes of $1'' \times 1''$, the galaxy N09 shows a total of the cells in emission of $\Delta F^{+}_{1314} \sim +1.0 \times 10^{-15}$ erg cm^{-2} s^{-1} Å^{-1}, and a net

continuum absorption of ΔF^{-}_{1314} = -0.4 $\times$ 10^{-15} erg cm^{-2} s^{-1} Å^{-1}. The resulting Lyα flux is the sum of these two converted to a line flux, which is 1.3 $\times$ 10^{-13} erg cm^{-2} s^{-1}. While the net emission at 1216 Å from this galaxy is properly represented by this value, it masks the fact that the Lyα emission from certain parts of the galaxy is actually higher, and is being offset by a deficit of continuum emission in other regions. If we take a larger 2″ $\times$ 2″ cell size, then the Lyα emission and continuum deficient regions blend together, and we only calculate an ΔF^{+}_{1314} of 0.84 $\times$ 10^{-15} erg cm^{-2} s^{-1} Å^{-1} and an ΔF^{-}_{1314} of 0.23 $\times$ 10^{-15} erg cm^{-2} s^{-1} Å^{-1}. Depending on the choice of cell size, we will obtain different answers for the amount of Lyα flux being emitted from different regions, even though the total galaxy emission at 1216 Å remains the same.

2.2.2 Spatial variation of Lyα emission

This study will explore the spatial variation of Lyα emission across the sample of galaxies. We have already shown that the choice of cell size over which we integrate our blue-band flux surplus/deficit will influence the calculation of the net Lyα emission and continuum absorption. Extended objects (N02, N04, N08, N09, and N12) are the most susceptible to noise at smaller scales, therefore we chose a cell size of 2″$\times$ 2″ in order to increase the fidelity of the total Lyα escape fraction measurement. Compact objects are more stable at smaller scales, therefore we chose a cell size of 1″$\times$ 1″ so that we can investigate the escape fraction at smaller scales. These cell

sizes are limited by the photon statistics of the ACS images (Fig. 2.4), but also by the ancillary optical spectral maps, which are also sampled at $\sim 1''$ scales (§2.3). Investigating the Lyα emission properties of these galaxies at higher resolution would show an even greater spread between the total Lyα in emission relative to the continuum deficit at 1216 Å.

2.3 Project Balmer - An Apache Point Observatory Study

The optical bandpass provides the crucial measurement of the Balmer series of hydrogen (n = $\infty \rightarrow 2$), which we require to determine $f_{Ly\alpha}$ from Case B recombination theory. The primary goal of obtaining optical spectral maps of these targets is to determine the Hα/Hβ ratio, which provides a measure of the total line-of-sight extinction, and enables the determination of the intrinsic Hα flux ($F_{\mathrm{H}\alpha,o}$). We generate low-resolution images of the targets in these spectral lines, and others in the bandpass, which could also be obtained using narrow band photometry. Spectral mapping has the added benefit of easily separating Hα from the [N II] $\lambda\lambda$ 6544, 6582 doublet, while also enabling the calculation of the metalicity, SFR, stellar age, and other spectral diagnostics. Each of these measurements can be assembled into images for direct comparison to the ACS photometry.

To that end, Project Balmer was initiated in 2008 with the goal of completely

mapping all 14 targets observed by HST. This intensive project was completed in 2012 with 12 of the 14 objects covered. The remaining 2 were left unobserved after analysis of the HST data showed little to no Lyα emission potential. In total, 49 half-nights of dark time observations were required to complete the data-set, with 31 half-nights needed to obtain the data presented, 2 spent on a 13th target not used, and 16 where conditions prevented useable observations. This section will outline the observations (§2.3.1) and the extensive data reduction pipeline (§2.3.2). The data cubes and spectral diagnostic maps are presented in §2.3.4. This section concludes with a description of how the data cubes are aligned to the HST data in §2.3.6.

2.3.1 DIS Observations

Optical spectral mapping was carried out using the *Dual Imaging Spectrograph* (DIS) on the 3.5 m telescope at APO. The instrument was configured in the low resolution (B400/R300) grating setting that enables full spectral coverage between $\sim$ 3500 – 10,000 Å. Each target was mapped using a "push-broom" observation style. A $0\farcs9 \times 6'$ long slit was placed across the face of the galaxy, and then a set of three redundant exposures were taken. The slit position was shifted by slightly less than one slit width until the entire galaxy had been observed (Fig. 2.5). A step size of $\sim$ $0\farcs85$ was used instead of $0\farcs9$ in an attempt to ensure a continuous coverage, however inclement observing conditions occasionally resulted in choppy and uneven tracking. The spatial scale of the spectra along the slit axis is $\sim 0\farcs42$ pixel^{-1}.

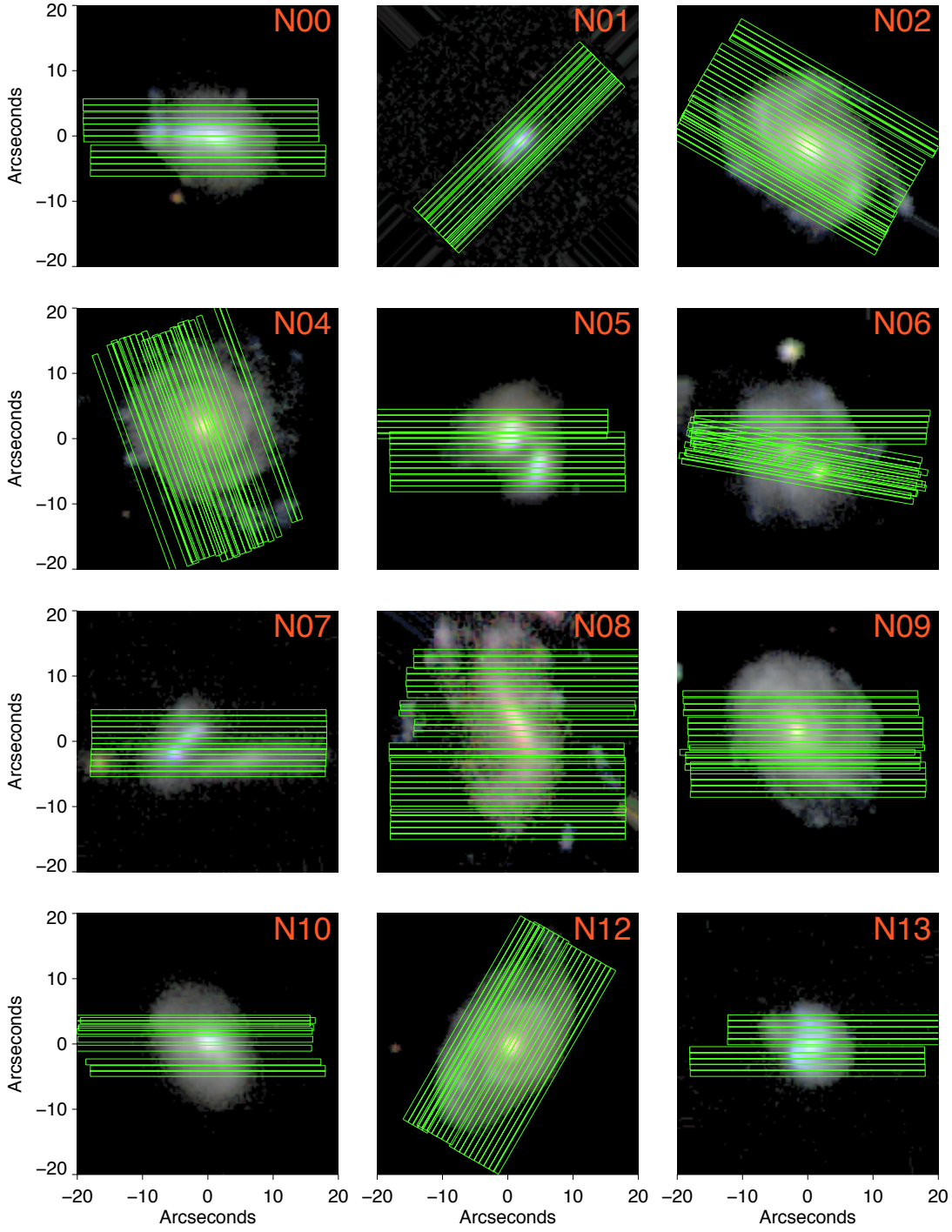

Figure 2.5: Slit overlays for Project Balmer targets with the slit length truncated to show the tracking errors in the slit dimension. North is oriented up in all images.

A calibration standard star was periodically observed at different airmasses to aid in the absolute flux calibration. The observations for N08 were taken with the instrument data pipeline set to rebin the spatial dimension by 2, resulting in a spatial scale of $0\farcs82$ pixel^{-1}. For consistency, this setting was used for all five nights of observation. On the third night of observing N06, the previously set telescope rotation angle of 10° was not applied, resulting in a triangular gap in coverage (Fig 2.5). Data from this object has been reduced, however an anomaly in the data from the second night has prevented us from reaching a level of fidelity that would merit inclusion of N06 in this study at this time. A summary of the targets and observations is listed in Table 2.3.

2.3.2 Data Reduction

Each set of three redundant exposures were median filtered to produce a single 2-D spectra for the red and blue channels for each slit position. A set of bias exposures were used to remove the DC offset of the CCD. Flat-fields were obtained by imaging a quartz lamp, with different exposure times to maximize the signal for the red and blue channels. A set of Helium + Neon + Argon calibration lamp exposures provided a filled slit spectrum for wavelength calibration. A new set of calibration data was taken for each night of observation.

The centroids of the calibration star spectra for various wavelength bins were used to calculate the rotation correction for each night. The airglow spectrum was

estimated by identifying off-target portions on either side of the target, and then interpolating along each airglow emission line in the spatial dimension to recover the line profile and intensity across the slit. This method performed significantly better than simply averaging the airglow emission on either side of the spectrum, as the shape of the line profile varied across the sky. The typical airglow emission in the red channel was $\sim$10$\times$ the galaxy continuum (Fig. 2.6), however it was only $\sim$5$\times$ at wavelengths near Hα.

The flux calibration standard stars were observed with both the $0\farcs9$ slit and a larger $5''$ slit in order to determine the slit losses when the photometric seeing was larger than the slit width. The ratio of the total flux in the calibration standard exposures to the *HST/Calspecs* published spectrum was used as the airmass dependant flux correction for the data. The scaling of the flux calibration for each wavelength with airmass was determined by interpolating the range of airmasses over which the standard star spectra were taken.

The red and blue channels, which are spatially offset along the slit, were aligned using a difference minimization routine. The channel mismatch slightly changed over time, therefore each pointing was aligned individually. The profiles were oversampled to 10$\times$ the native resolution to allow for fractional pixel alignments. The spatial scale of the red channel ($0\farcs40$ pixel^{-1}) was interpolated up to the spatial scale of the blue channel ($0\farcs42$ pixel^{-1}) (Fig. 2.7).

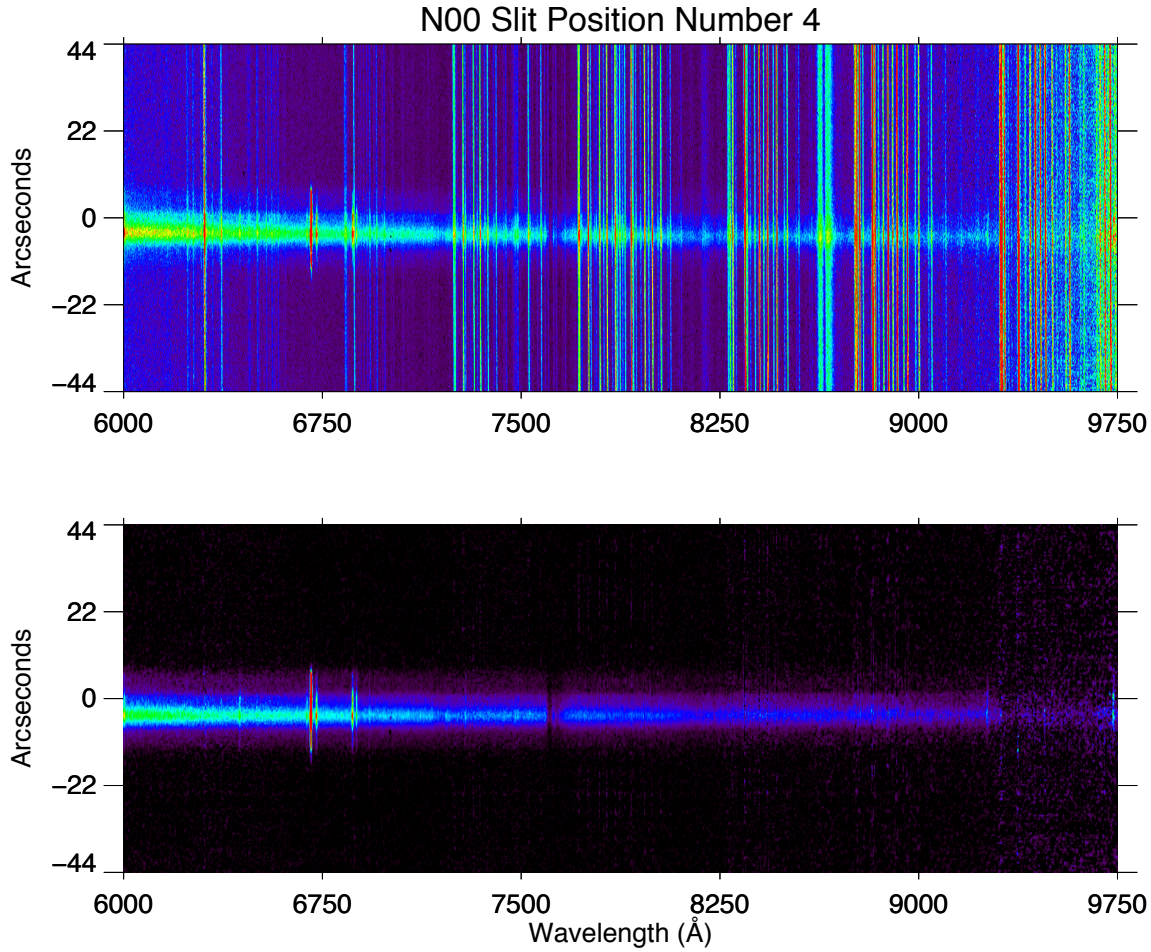

Figure 2.6: (Top) The central portion of a raw 2-D spectrum of N00. (Bottom) An airglow, rotation and distortion corrected version. The color scales of these two images are identical

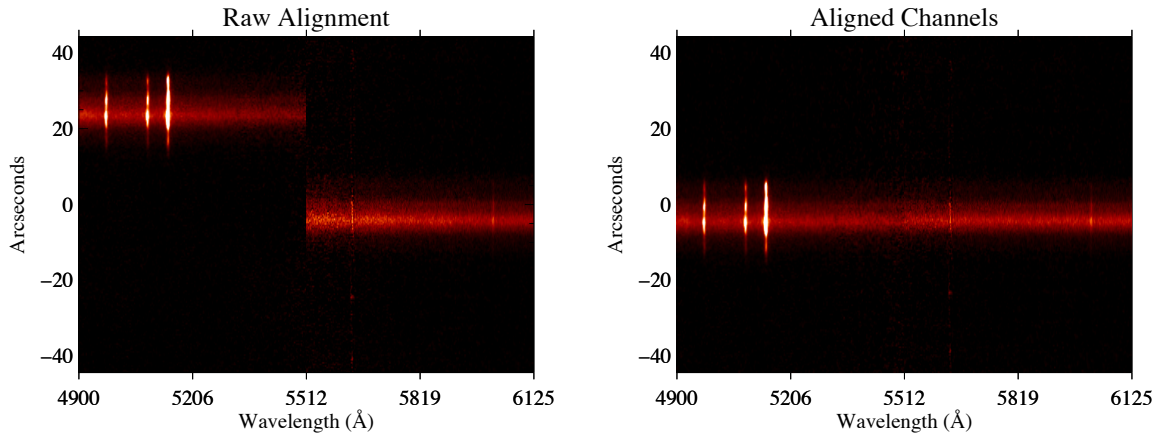

Figure 2.7: (Left) The native alignment of the red and blue channels for a 2-D spectrum of N00. (Right) The matching of the two channels after alignment.

2.3.2.1 Pointing Alignment

The exact position of each slit is critical to constructing an accurate 3-D spectral data cube. Simply assuming that each pointing represents a 0.″9 portion of the target offset 0.″9 from the previous pointing would not accurately reconstruct the profile of the galaxies. The final alignment must be accurate to at least the SDSS pixel size (0.″396 pixel^{-1}) in order to accurately compare the optical data cubes to *HST* photometry.

Guide camera images of the target region were used to calculate the true center of the slit at any given position. Approximately 20 – 50 guider images exist per pointing depending on the exposure time. The centroid of the brightest star in the guidecam field of view for each image was used to estimate the tracking errors and offsets. The dispersion of the telescope pointing can be seen in the slit overlays in Figure 2.5,

where tracking errors occasionally caused sequential pointings to overlap or shift in the slit dimension, especially during inclement weather.

Each 2-D exposure was divided into 9 identical spectra, with each representing synthetic 0.″1 slits, and that block of data was positioned in a map array based on the calculated position of the slit. If one of the synthetic slits overlaps with another from a different pointing, then the weighted average spectrum is substituted for the original synthetic slit, where the weighting is determined by the depth of the 0.″1 slit within the parent 0.″9 slit. For N partially overlapping spectra, the final 2-D spectrum, S, for each synthetic 0.″1 slit is given by the weighted sum of each of the individual 0.″9 spectra, S_N

$$S = \frac{\Sigma_N S_N (0.5 - \frac{|j_n - 5|}{9})}{\Sigma_N (0.5 - \frac{|j_n - 5|}{9})} \tag{2.6}$$

where j_n is the synthetic slit number (from 1-9) for each overlapping 0.″1 slit within it's 0.″9 parent. So for 2 exposures that are 0.″7 offset from each other, the resulting array would be 1.″6 wide, with the first 0.″7 represented by $7/9^{ths}$ of the first 0.″9 exposure, the next 0.″1 by 0.0833 ($3/36^{th}$) of the first exposure and 0.0278 ($1/36^{th}$) of the second, the next 0.″1 by 0.0278 of the first exposure and 0.0833 of the second, and the remaining 0.″7 by $7/9^{ths}$ of the second exposure. After the map is constructed, the spatial dimension is truncated to 91.″8.

Any gaps in the coverage area are filled by an interpolation of the nearest slits for each wavelength. The largest gap in coverage of any target is 1.″5 for N04. For

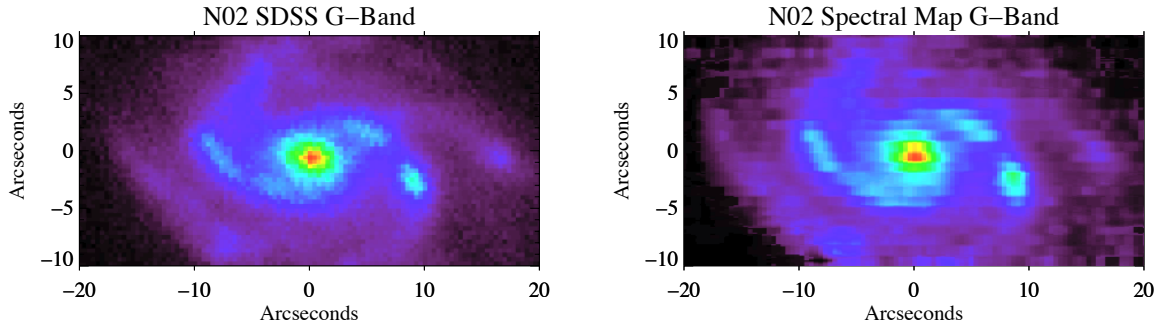

Figure 2.8: (Left) SDSS g-band image of N02 (Right) SDSS g-band filter curve convolved with the aligned APO spectral data cube.

most cases, however, coverage gaps are $< 0\farcs5$. Observations from different days were intentionally overlapped, so that coincident data could be used to scale the flux calibrations. These differ slightly from day to day depending on the seeing and airglow conditions.

We aligned the data cubes with SDSS photometry in order to scale the brightness profile and check the fidelity of the map assembly. Each data cube was convolved with the SDSS g, r and i filter curves, and the resulting images were rebinned to the SDSS pixel scale. A window matching routine that minimized the square of the difference of the two normalized images aligned the coordinate systems (Fig. 2.8). The ratio of the normalized DIS images to the SDSS photometry was then used as a scale factor to smooth the data cube profile. The portion of the data cubes that overlap with the SDSS $3''$ diameter fiber pointings were summed to check the flux calibration against the SDSS spectra (Fig. 2.9).

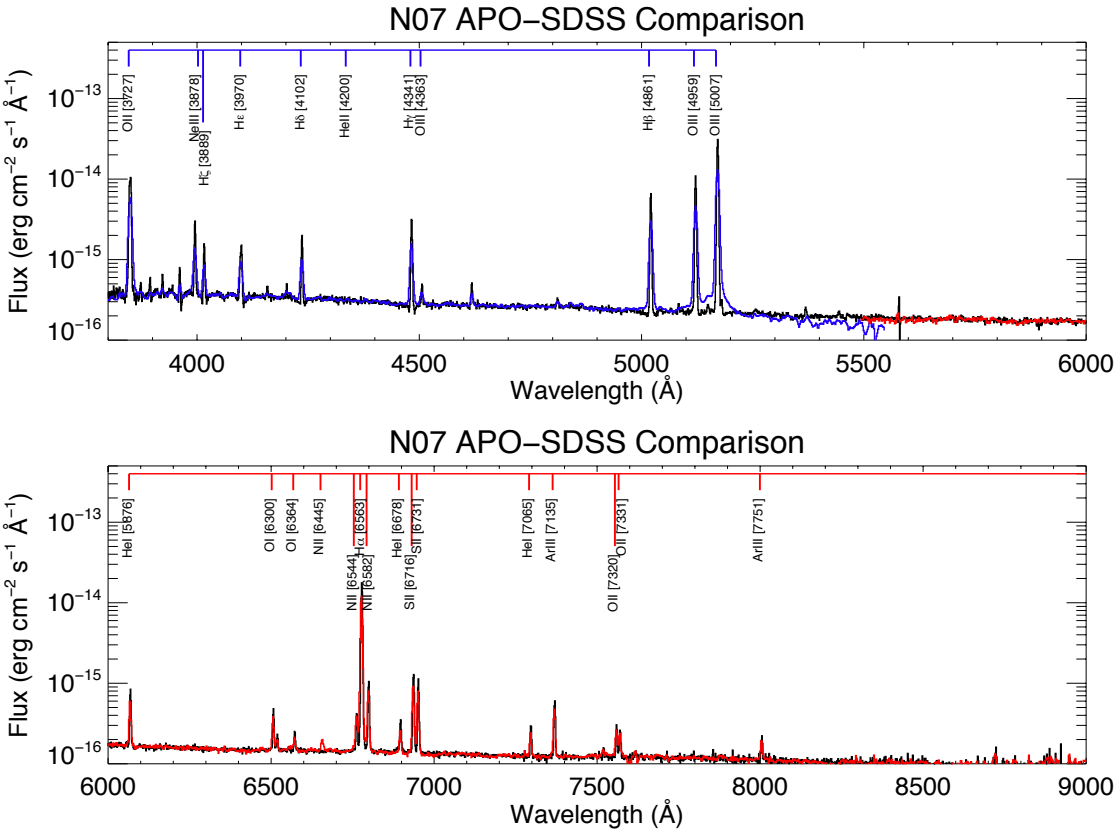

Figure 2.9: APO spectra for the 3″ diameter region covered by the SDSS fiber for N07. Each spectra is in the native scale of the respective instrument, so line width and peak heights are not the same for the same total line flux.

Project Balmer Observations

Target	No. of Steps	Exposure Time (s)	Half Nights	Calibration Standard	No. of Aligned Spectra
N00	12	300	2	Hz44	25,488
N01	9	300	2	Feige67	14,266
N02	27	300	3	Hz44	44,928
N04	25	900	5	Feige34	55,512
N05	15	300	2	Hz44	27,216
N06	19	450	3	Hz44	24,624
N07	12	300	1	Feige34	22,248
N08	31	600	4	Feige34	33,335
N09	19	900	4	Hz44	35,208
N10	10	300	1	Hz44	16,200
N12	22	300	2	Feige34	36,504
N13	10	300	2	Hz44	20,304
Totals	211	84h 52.5m	31	–	355,833

Table 2.3: APO Project Balmer Observations

2.3.3 3-D Spectral Data Cubes

Each 3-D spectral data cube represents a grid $N \times 91\farcs8$ of spectra covering the 3500 – 10,000 Å bandpass with an oversampled spatial scale of $0\farcs42 \times 0\farcs1$, where N is the angular length covered by the mapping. The total number of flux calibrated 1-D spectra is given in Table 2.3, although some of these spectra are oversampled, but smoothed, duplicates, and not all contain galaxy emission. The spectra were corrected for the line-of-sight Milky Way extinction in the observed wavelengths before extracting line strengths. We use the Milky Way extinction map of Schlegel et al. (1998) [55] with an R_V=3.1 and the extinction curve of Osterbrock and Ferland (2006) [40]. Every 1-D spectra is analyzed for emission at Hα, and spectra with a SNR $\geq$ 3 in Hα are subsequently analyzed for other line emission. Spectral lines strengths are determined by subtracting a spline fit to the underlying continuum emission, and then fitting the residual line with a Gaussian profile and integrating. We also calculate the equivalent width (EW), full-width at half-maximum (FWHM), line centroid, and flux uncertainty for each line.

2.3.3.1 Stellar Absorption Correction

Significant stellar absorption features complicate the determination of the extinction from the Hα/Hβ ratio. The standard practice is add to the Hα and Hβ equivalent widths to correct for this absorption [56]. In some cases, a constant correction of 2 Å to all of the Balmer lines is used [48, 57]. In this study, however, we found that the 2

Å correction underestimates the Hβ flux and results in a higher extinction estimation for the regions coincident with the SDSS fiber than is computed by the SDSS.

The SDSS uses a stellar age dependent model fit to the spectrum to extract the corrected line fluxes. We calculated ΔEW using the low-metalicity 4000 Å break (D_n4000, see §2.3.4.4) dependant relation in Mattsson and Bergvall (2008) [58]. D_n4000 was originally defined as the total flux between 4050 – 4250 Å divided by the total flux between 3750 – 3950 Å [59], and was later refined to the 4000 – 4100 Å and 3850 – 3950 Å bandpasses [60]

$$D_n4000 = \frac{\int_{4000}^{4100} f_\lambda d\lambda}{\int_{3850}^{3950} f_\lambda d\lambda}. \tag{2.7}$$

The [Ne III] λ3869 emission line must be removed prior to calculation. D_n4000 is considered an indicator of the stellar age, and is small when there is ongoing or recent star-formation due to the low metal opacity in O and B stars. This method is similar to the method used in the SDSS data reduction pipeline in that it relies on a stellar age diagnostic to determine ΔEWs. We systematically calculate D_n4000 values between 5-15% smaller than the D_n4000 of the SDSS for the same 3″ region (see §2.3.4.4), however, resulting in values of $\Delta EW_{H\beta} \sim$ -1 Å greater for targets with older stellar populations (N04, N08, N09, N12). The sensitivity of these low line emission targets is such that this 1 Å extra boost to the EW results in Hα/Hβ ratios < 2.87 and negative extinction, which is unrealistic.

An accurate stellar absorption correction is critical to determining $f_{Ly\alpha}$ in targets

with low $EW_{H\beta}$, such as N12. The ΔEWs from the SDSS for N12 ($\Delta EW_{H\alpha} = 1.83$ and $\Delta EW_{H\beta} = 2.44$) and calculated from our D_n4000 ($\Delta EW_{H\alpha} = 1.86$ and $\Delta EW_{H\beta} = 3.41$) result in total H$\beta$ fluxes that are different by 27%. If we assume E(B-V)=0 for our D_n4000 derived $\Delta EW_{H\beta}$, then the E(B-V) for the SDSS derived $\Delta EW_{H\beta}$ would be 0.23. This would result in an intrinsic Hα flux 75.8% higher than in the E(B-V) = 0 case, reducing the calculated $f_{Ly\alpha}$ by ~40%. For higher observed $EW_{H\beta}$ this sensitivity is greatly reduced, and even in low line emission targets the $EW_{H\beta}$ is typically 10 – 30 Å for emission coincident with star-formation (See §2.3.4), nevertheless the choice of ΔEW is very important.

While it is tempting to have a simple relation that could determine the variation of ΔEW across a target, a combination of our overestimation of ΔEW in low line emission galaxies and the low SNR in the 4000 Å continuum for some of our 1-D spectra, leads us to chose to apply the SDSS derived correction to each galaxy as a whole. This leads to an uncertainty in $EW_{H\beta}$ that is related to the variation of D_n4000 in each target, which would typically be $\sim \pm 1$ Å. The Hα and Hβ raw EWs and SDSS ΔEWs are presented in Table 2.4.

2.3.4 Emission Line Diagnostics

In the optical bandpass there are usually many different established diagnostics for determining galaxy properties. Kewley and Ellison (2008) lists in detail 10 optical diagnostics for determining the metalicity alone [61]. The stellar age is often related

Target	$EW_{H\alpha}$ (Å)	$EW_{H\beta}$ (Å)	$\Delta EW_{H\alpha}$ (Å)	$\Delta EW_{H\beta}$ (Å)
N00	-102.4	-12.5	-2.68	-4.14
N01	-300.1	-45.6	-2.53	-3.11
N02	-41.30	-5.42	-2.52	-3.50
N04	-12.88	-1.01	-1.89	-2.09
N05	-116.4	-17.0	-2.38	-3.22
N07	-121.0	-20.19	-2.48	-3.06
N08	-27.28	-3.23	-1.98	-2.68
N09	-16.4	-1.81	-1.96	-2.59
N10	-42.58	-6.09	-2.82	-3.92
N12	-10.34	-1.16	-1.83	-2.44
N13	-102.2	-17.35	-2.82	-3.50

Table 2.4: The uncorrected Balmer line EW and the SDSS derived ΔEW.

to D_n4000, but can also be referenced to the EW of the H_δ absorption line [62], or by model fits to the spectrum. In many cases we have calculated multiple diagnostics, such as the metalicity using both the [NII]/Hα and ([OIII]/Hβ)/([NII]/Hα) ratio methods from Pettini & Pagel 04 [63], and the [NII]/[OII] ratio method from Kewley & Dopita 02 [64]. Since the primary goal of this study is to show the evolution of $f_{Ly\alpha}$ with local properties, we have elected to showcase only the methods that are the least susceptible to noise, as opposed to those that produce the most accurate result. A sample of spectral emission line and diagnostic maps from N00, N02, and N13 are presented in figures 2.10, 2.11, and 2.12, with all other presented in Appendix A.

The diagnostic relations are discussed in the following sections. A Baldwin-Phillips-Terlevich (BPT) diagram of the log[[OIII]/Hβ] versus the log[[NII]/Hα] ratios for every pixel in which all four lines are in emission is presented in Figure 2.13 All portions of these galaxies fall into the star-formation locus [65].

2.3.4.1 Star Formation Rate

We estimate the star formation rate (SFR) using the Hα luminostiy ($L_{H\alpha}$) and spectral line efficiency $\eta_{H\alpha}$ based on the model of Charlot and Longhetti (2001) [66,67],

$$SFR = \frac{L_{H\alpha}}{\eta_{H\alpha}}, \tag{2.8}$$

where $\eta_{H\alpha}$ is a function of the uncorrected flux ratios Hα/Hβ, [OII]/[OIII], [OIII]/Hβ, [SII]/Hα, and $EW_{H\beta}$. We calculate $L_{H\alpha}$ using the distance luminosity method of Pen (1999) [68]. We find SFRs ranging from $\sim 1 - 45$ $M_\odot$ yr^{-1} for our sample.

2.3.4.2 Balmer Ratios and Extinction

The intrinsic ratio of the Hα to Hβ flux, according to case B recombination theory at T $\sim 10^4$K and $n_e \sim 10^2$ cm^{-3}, is 2.87 [40]. Assuming an $R_V = 3.1$ and using the extinction curve of Osterbrock and Ferland (2006)

$$E(B-V)_g = 0.966 \ln\left(\frac{H\alpha/H\beta}{2.87}\right). \tag{2.9}$$

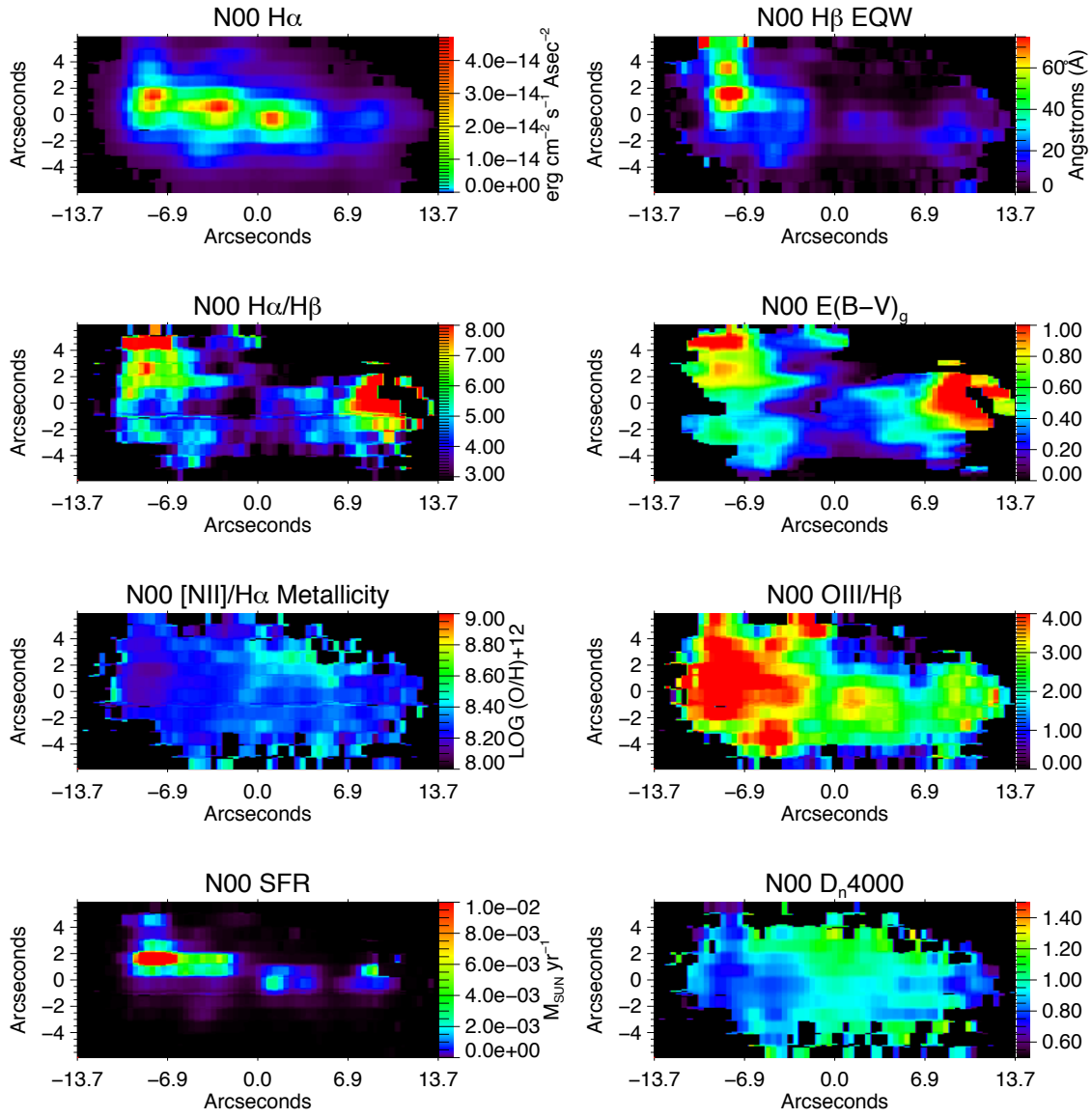

Figure 2.10: Milky Way extinction corrected Hα flux and diagnostic maps from N00

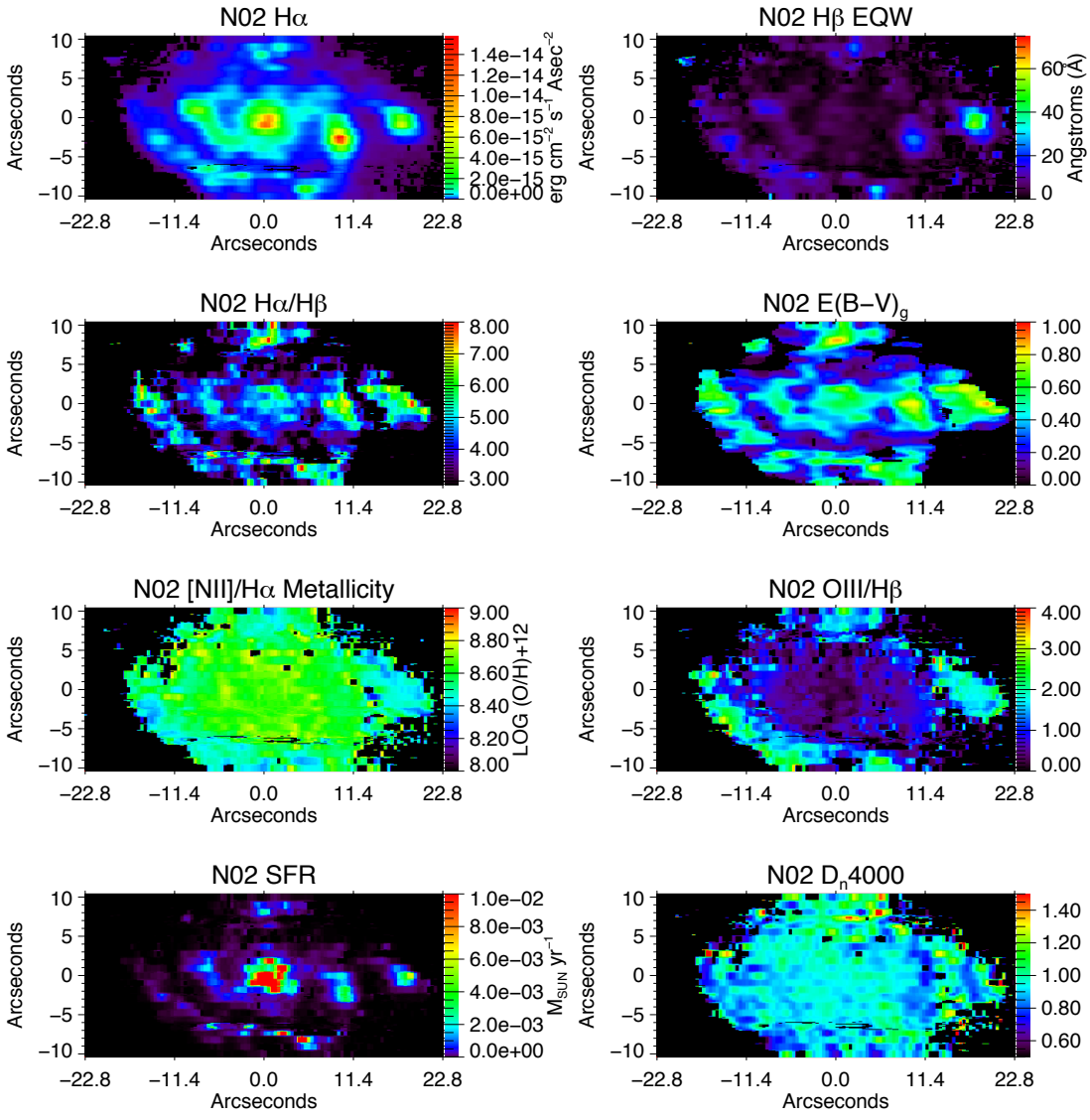

Figure 2.11: Milky Way extinction corrected Hα flux and diagnostic maps from N02

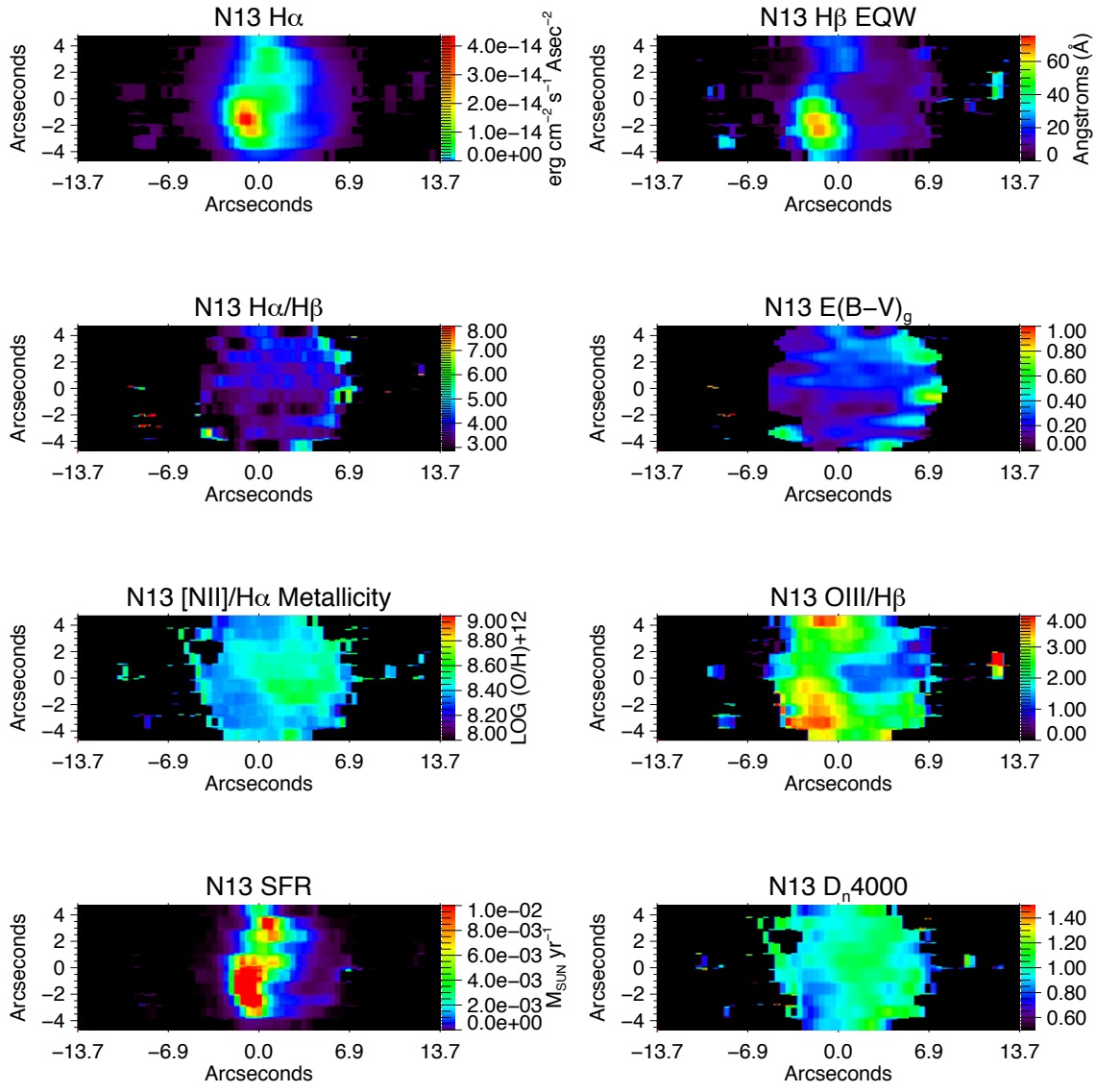

Figure 2.12: Milky Way extinction corrected Hα flux and diagnostic maps from N13

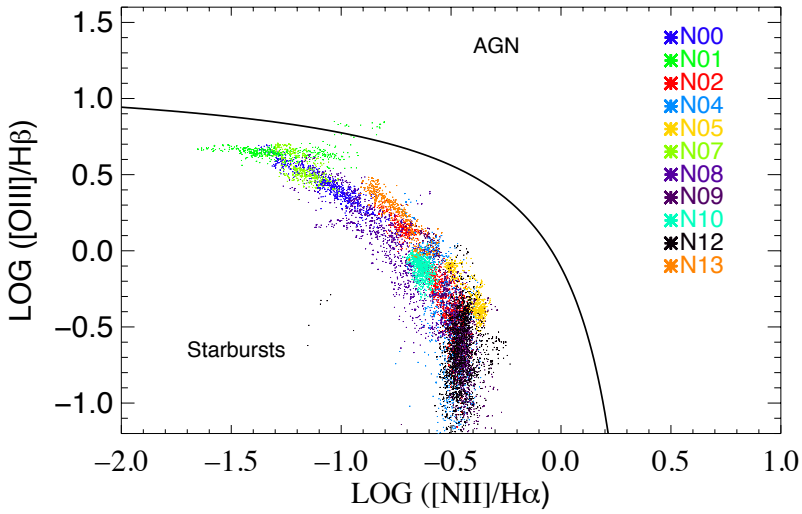

Figure 2.13: BPT diagram indicating that the entire sample is made up of regions dominated by star-formation, but to varying degrees. The solid black line marks the boundary between star-formation and AGN powered emission.

We use E(B-V)$_g$ to differentiate from the Milky Way extinction, E(B-V)$_{MW}$. In Table 2.5 we present the raw Hα and Hβ fluxes ($F_{\rm H\alpha}$ and $F_{\rm H\beta}$), the extinction calculated by collapsing the entire data cube into a single spectrum (E(B-V)$_g^{SS}$), the extinction computed for the region coincident with the SDSS fiber (E(B-V)$_{SD}$), and then the corrected Hα flux using the both the co-added spectrum corrected by E(B-V)$_g^{SS}$ ($F_{\rm H\alpha,o}^{SS}$) and by correcting each pixel based on the E(B-V)$_g$ computed for the spectrum in that pixel ($F_{\rm H\alpha,o}$). The variation of E(B-V)$_g$ in each galaxy can be seen in figures 2.10, 2.11, and 2.12, and in Appendix A.

All points in which the line signal is too low to calculate an accurate E(B-V)$_g$ are assigned an E(B-V)$_g$ equal to the galaxy average when the correction is applied.

Target	E(B-V)$_{MW}$	$F_{\mathrm{H}\alpha}$	$F_{\mathrm{H}\beta}$	E(B-V)$_{SD}$	E(B-V)$_g^{+\sigma}_{-\sigma}$	$F^{SS}_{\mathrm{H}\alpha,o}$	$F_{\mathrm{H}\alpha,o}$
N00	0.012	2.71	0.67	0.009	$0.328^{+0.29}_{-0.13}$	6.06	8.99
N01	0.012	1.50	0.40	0.079	$0.191^{+0.20}_{-0.08}$	2.38	2.81
N02	0.010	2.50	0.65	0.540	$0.288^{+0.18}_{-0.10}$	5.06	7.63
N04	0.031	0.89	0.21	0.53	$0.377^{+0.23}_{-0.14}$	2.23	3.48
N05	0.020	7.78	1.75	0.409	$0.425^{+0.15}_{-0.16}$	22.01	23.97
N07	0.019	1.93	0.59	0.16	$0.129^{+0.15}_{-0.03}$	2.66	3.37
N08	0.015	0.71	0.20	0.215	$0.193^{+0.18}_{-0.07}$	1.14	1.78
N09	0.013	0.62	0.17	0.202	$0.223^{+0.18}_{-0.07}$	1.07	1.70
N10	0.009	0.95	0.29	0.215	$0.113^{+0.15}_{-0.05}$	1.25	1.52
N12	0.013	0.75	0.25	0.546	$0.05^{+0.33}_{-0.01}$	0.84	4.21
N13	0.011	1.46	0.42	0.356	$0.193^{+0.14}_{-0.05}$	2.35	2.62

Table 2.5: Milky Way extinction E(B-V)$_{MW}$, observed total Hα and Hβ fluxes in units of 10^{-13} erg cm^{-2} s^{-1}, E(B-V)$_{SD}$ derived from the SDSS measured Hα and Hβ line fluxes from the target galaxy (which cover only a 3″ diameter area), E(B-V)$_g$ derived from the Balmer ratio of the co-added spectrum for the entire map, and the single spectrum corrected total Hα and Hβ fluxes in units of 10^{-13} erg cm^{-2} s^{-1}.

Spectra assigned the average extinction generally have very low line emission, so the error introduced by using the galaxy average is minimal.

2.3.4.3 Metalicity and Stellar Mass

We chose to use the [NII]/Hα relation for mapping metalicity because the calculation is virtually extinction independent due to the close proximity of [N II] λ6584 and Hα [63]. There is likely to be some contamination of the [N II] λ6584 flux due

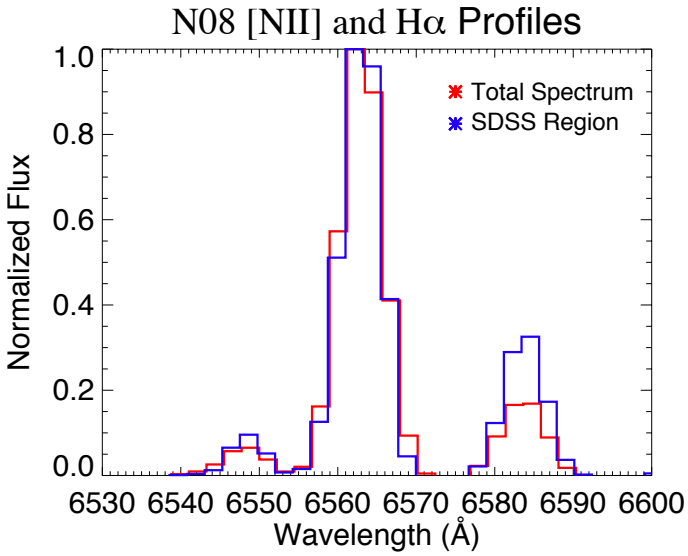

Figure 2.14: Hα and [N II] $\lambda\lambda$ 6544, 6582 emission from N08 for the entire galaxy (red) and for a 3″ region centered on the SDSS fiber (blue).

to blending with Hα, however in most cases the two lines are clearly separated even at the low resolution of DIS, with the region between the lines reaching a continuum subtracted flux $\sim$ 0 even for relatively strong [N II] emitters (Fig. 2.14). We also calculate metalicity using the ([O II] + [O III])/Hβ so that we may utilize the mass-metalicity relation of Tremonti et al. (2004) to determine the Mass (M_*) [69, 70], however we do not present a diagnostic map of that relation.

2.3.4.4 4000 Å Break

We have chosen to use D_n4000 as a measure of the stellar age rather than H_δ absorption, as the low spectral resolution of DIS poorly probes absorption lines (see §2.3.3.1). We systematically derive D_n4000 ratios $\sim 0-10\%$ lower than the SDSS for

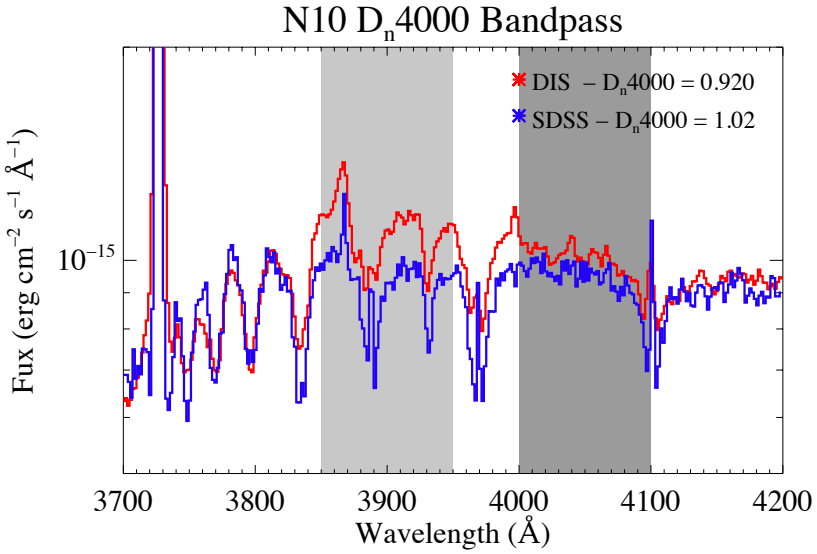

Figure 2.15: A comparison of the relevant D$_n$4000 bandpass for the SDSS spectrum and the coincident region of the DIS spectral map.

coincident regions. This is likely due to a systematic error in the flux scaling within the 3700 – 4000 Å bandpass (Fig. 2.15). The cause of this scaling error is not clear, however it appears to be constant for each target, so it should not effect the use of D$_n$4000 as a relative diagnostic.

2.3.5 Discrepancy Between Maps and Co-added Spectrum

A summary of these diagnostics is presented in Table 2.6, along with the 1σ high and low for the metalicity and D$_n$4000 diagnostic maps. The D$_n$4000 ratio is as measured for a co-added, uncorrected spectrum, but all other relations are calculated

using the sum of the relevant extinction corrected spectral line maps as the inputs to the formulae. This produces the same answer as if the extinction corrected data cube is condensed into a single spectrum to within $\sim 1.5\%$. The extinction corrections for each data cube are based on the extinction maps. The SFR is presented both as calculated by the single co-added spectrum (SFR^{SS}) and as the sum of the SFR diagnostic map ($\Sigma\mathrm{SFR}^{map}$). The difference between these two SFR, and between the similarly calculated intrinsic Hα fluxes, $F^{SS}_{\mathrm{H}\alpha,o}$ and $F_{\mathrm{H}\alpha,o}$, provides a measure of the error introduced by observing the galaxy through a single aperture, which we will outline in this section.

The total of all the spectral line fluxes in a line map compares well to the line flux extracted when we condense the spectral data cube into a single spectrum for each target. In general, the difference between the total of all the individual pixel line fluxes and that from the co-added spectrum is $< 2\%$. When diagnostic relations are calculated from the co-added spectra, however, they tend to track the properties of the dominant line emission regions. This does not always paint an accurate picture of the galaxy.

For example, we take two identically sized $2'' \times 2''$ regions in N00 and label them regions A and B. The relevant uncorrected line strengths, in units of 10^{-15} erg cm^{-2} s^{-1}, for each are given in Table 2.7. For region A, we calculate a SFR of 2.58 $\mathrm{M}_\odot$ yr^{-1} and an E(B-V)$_g$ of ~ 0.61, and for region B we calculate a SFR of only 1.08 $\mathrm{M}_\odot$ yr^{-1} and an E(B-V)$_g$ ~ 0.24. When the fluxes are combined, we calculate a SFR of

Target	$D_n4000^{+\sigma}_{-\sigma}$	$Z_{[NII]/H\alpha}{}^{+\sigma}_{-\sigma}$	$Z_{[O]/H\beta}{}^{+\sigma}_{-\sigma}$	M_*	SFR^{SS}	ΣSFR^{map}
		log(O/H)+12	log(O/H)+12	log($M/M_\odot$)	$M_\odot$ yr^{-1}	$M_\odot$ yr^{-1}
N00	$0.93^{+0.12}_{-0.07}$	$8.24^{+0.09}_{-0.04}$	$8.42^{+0.24}_{-0.16}$	8.53	3.72 ± 0.9	5.64
N01	$0.81^{+0.07}_{-0.09}$	$8.16^{+0.10}_{-0.05}$	$8.44^{+0.17}_{-0.28}$	8.55	5.58 ± 1.45	7.03
N02	$0.93^{+0.14}_{-0.05}$	$8.57^{+0.08}_{-0.10}$	$8.84^{+0.16}_{-0.21}$	9.58	9.04 ± 2.35	14.7
N04	$0.98^{+0.13}_{-0.04}$	$8.62^{+0.08}_{-0.10}$	$8.80^{+0.26}_{-0.28}$	9.46	0.96 ± 0.23	5.03
N05	$0.99^{+0.19}_{-0.05}$	$8.75^{+0.05}_{-0.09}$	$8.91^{+0.12}_{-0.18}$	9.85	37.6 ± 9.8	45.6
N07	$0.98^{+0.10}_{-0.07}$	$8.20^{+0.10}_{-0.03}$	$8.44^{+0.28}_{-0.15}$	8.57	5.08 ± 1.3	4.52
N08	$0.95^{+0.11}_{-0.06}$	$8.40^{+0.11}_{-0.09}$	$8.31^{+0.38}_{-0.25}$	8.36	0.86 ± 0.22	1.04
N09	$1.11^{+0.12}_{-0.05}$	$8.67^{+0.06}_{-0.08}$	$8.91^{+0.17}_{-0.21}$	9.82	1.84 ± 0.5	2.48
N10	$0.96^{+0.10}_{-0.02}$	$8.51^{+0.06}_{-0.04}$	$8.85^{+0.15}_{-0.06}$	9.61	1.23 ± 0.32	1.63
N12	$1.20^{+0.14}_{-0.09}$	$8.70^{+0.07}_{-0.07}$	$9.02^{+0.14}_{-0.15}$	10.33	0.80 ± 0.21	9.78
N13	$0.99^{+0.09}_{-0.06}$	$8.41^{+0.07}_{-0.06}$	$8.67^{+0.18}_{-0.11}$	9.09	7.64 ± 1.99	7.14

Table 2.6: Global values of D_n4000, metalicity (using both the [NII]/Hα method used for spectral mapping and the ([OII] + [OIII])/Hβ method for using the Tremonti 04 mass-metalicity relation, the mass from the Tremonti 04 relation, and the star formation rate derived from the Hα luminosity as a single spectrum or totaled diagnostic map

only 2.56 $M_\odot$ yr^{-1} and an E(B-V)$_g \sim 0.34$, as the overall brighter emission region dominates the line ratios and masks the intense star formation in region A.

When the fluxes are corrected for extinction using the co-added spectrum derived extinction E(B-V)$_g = 0.34$, which is similar to the global value in Table 2.5, the Hα flux becomes $F_{H\alpha,o} \sim 3.2 \times 10^{-13}$ erg cm^{-2} s^{-1} . When the two regions are corrected separately for E(B-V)$_g = 0.61$ and 0.24 respectively, the total Hα flux becomes $F_{H\alpha,o}$

Region	$F_{H\alpha}$	$F_{H\beta}$	F_{OIII}	F_{OII}	F_{SII}	$EW_{H\beta}$
A	49.6	9.2	38.7	16.0	8.8	-20.4
B	92.6	25.2	84.0	62.0	17.8	-11.5
A + B	138.7	33.9	126.6	76.5	26.8	-12.9

Table 2.7: Uncorrected line fluxes in N00 corresponding to two $2'' \times 2''$ regions with the highest (A) and lowest (B) extinctions, and from a co-added spectrum of the two regions.

$\sim 3.85 \times 10^{-13}$ erg cm^{-2} s^{-1}. An examination of the spectra for each of these regions shows that region B is dominant in the continuum emission, in addition to having stronger line emission (Fig. 2.16). When combined, the resulting spectrum retains the form and relative line ratios of the region B spectrum, and any analysis underestimates the extinction correction, SFR, and intrinsic line fluxes as a result. This is especially important in galaxies with strong, heavily extinguished star-formation.

2.3.6 Alignment to *HST* data

A similar window matching routine to that described in §2.3.2.1 was used to align the HST/ACS-b band images with the sum of the Hα, Hβ, [O III] λ5007 and [O II] λ3727 fluxes, however due to differences in the FUV and optical profile of the galaxies, some manual adjustment was necessary (Fig. 2.8). The HST photometry was degraded in resolution to $0\farcs1 \times 0\farcs1$, and then smoothed to account for the lower data cube resolution of $\sim 0\farcs9 \times 0\farcs85$. The line emission and diagnostic maps were

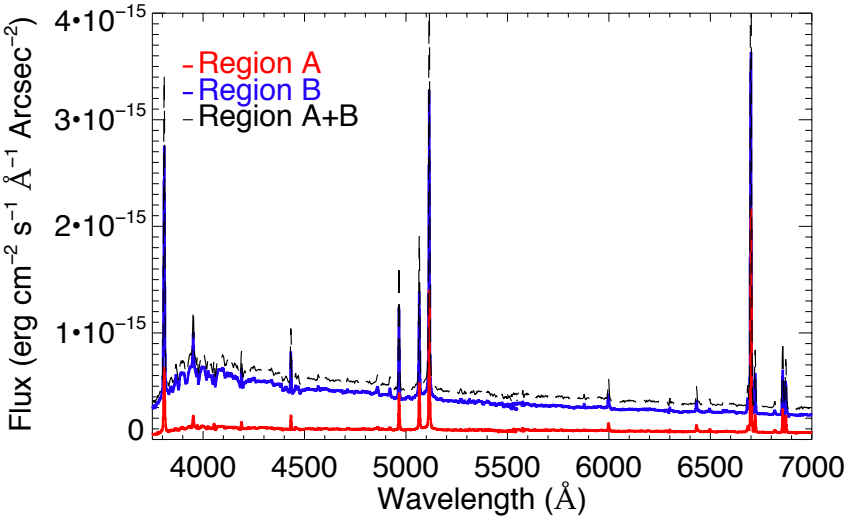

Figure 2.16: A comparison of the high extinction and high SFR spectrum of region A in N00 (red) to the low extinction, low SFR spectrum of region B (blue)

similarly rebinned to 0.″1 × 0.″1 from 0.″42 × 0.″1 (Fig. 2.17).

2.4 Lyα Escape Fraction

We define $f_{Ly\alpha}$as the ratio of the Milky Way extinction corrected Lyα flux ($F_{\mathrm{Ly}\alpha,obs}$) to the intrinsic Ly$\alpha$ flux ($F_{\mathrm{Ly}\alpha,o}$),

$$f_{Ly\alpha} = \frac{F_{\mathrm{Ly}\alpha,obs}}{F_{\mathrm{Ly}\alpha,o}}, \tag{2.10}$$

where

$$F_{\mathrm{Ly}\alpha,o} = 8.1 F_{\mathrm{H}\alpha,o}. \tag{2.11}$$

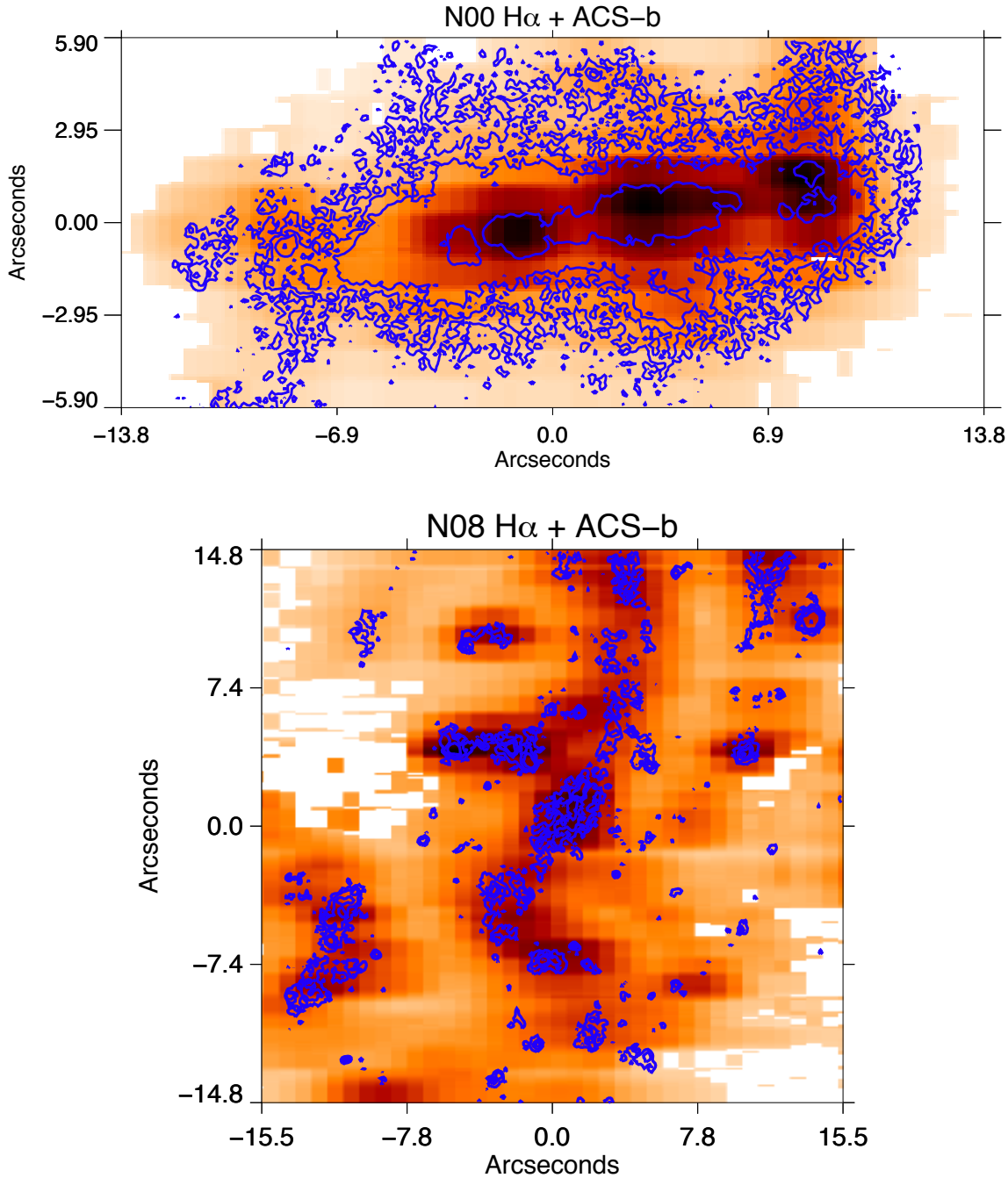

Figure 2.17: Image of Hα for N00 and N08 with the aligned *HST* blue filter contours overlaid.

Escape fractions are computed for $1'' \times 1''$ cells in the bright, compact targets (N00, N01, N05, N07, N10, N13), and $2'' \times 2''$ cells for extended objects (N02, N04, N08, N09, N12). The choice of larger cell size in the extended objects reduces the uncertainty due to the slit alignment. Quantifying a total escape fraction for these targets is complicated by the continuum absorption, as described in §2.2.1.1.

In Table 2.8 we present a summary of the total estimated Lyα flux of cells with net emission ($F^{+}_{\mathrm{Ly}\alpha}$) and the flux deficit of cells exhibiting a continuum deficiency (ΔF^{-}_{1316}). The escape fraction is presented in two different ways, first as calculated using the net ΔF_{1316} and equation 2.5 ($f_{Ly\alpha}$), and then using only the cells with a positive Lyα flux ($f_{Ly\alpha,+}$), but still the same total $F_{\mathrm{H}\alpha,o}$. The second value can be considered an upper limit and would change depending on the cell size. As a measure of how Lyα varies with sightline, we also compute $f_{Ly\alpha,\Pi}$, the ratio of $F_{\mathrm{Ly}\alpha,o}$ in cells with Lyα emission to the $F_{\mathrm{H}\alpha,o}$ from only those same cells. Also presented in Table 2.8 is the $F_{\mathrm{H}\alpha,o}$ for the region covered by the ACS pointing (extended objects overfill the ACS aperture), the net galaxy Lyα luminosity ($L_{\mathrm{Ly}\alpha}$), and $f_{Ly\alpha,w}$, the escape fraction for the cell with the highest uncorrected Hα flux-weighted escape fraction, $P_n(f_{Ly\alpha})$, given as

$$P_n(f_{Ly\alpha}) = f_{Ly\alpha_n}\left(\frac{F_{\mathrm{H}\alpha,n}}{\Sigma_n F_{\mathrm{H}\alpha}}\right)^2. \tag{2.12}$$

The cell (n) with the highest $P_n(f_{Ly\alpha})$ is conceivably a cell with a high amount of ongoing recombination, which should be traced by Hα, but also a high $f_{Ly\alpha}$. If

$f_{Ly\alpha}$ and f_{esc} are related, then LyC observations along these sightlines should reveal a similar f_{esc}. These regions would be quality targets for future LyC observations. $f_{Ly\alpha,\Pi}$ is a measure of the escape fraction that would be estimated if only particular sightlines where there is Lyα emission were probed.

Target	SA_{cell}	$F^{+}_{Ly\alpha}$	ΔF^{-}_{1316}	$L_{Ly\alpha}$	$F_{H\alpha,o}$	$f_{Ly\alpha}$	$f_{Ly\alpha,+}$	$f_{Ly\alpha,\Pi}$	$f_{Ly\alpha,w}$
N00	0.20	9.10	-0.15	9.21	8.99	0.124	0.126	0.130	0.31
N01	0.50	8.84	-0.46	21.4	2.80	0.370	0.390	0.422	0.37
N02	1.35	1.51	-1.84	-0.56	6.71	-0.006	0.028	0.058	0.03
N04	1.14	2.35	-1.90	0.66	3.42	0.016	0.085	0.139	1.2
N05	0.39	5.74	-0.27	10.84	23.78	0.028	0.030	0.034	0.05
N07	0.46	4.43	-1.27	7.44	3.34	0.117	0.164	0.242	0.136
N08	1.19	1.56	-1.11	0.69	1.39	0.040	0.138	0.250	0.41
N09	1.21	1.82	-0.47	2.08	1.68	0.100	0.134	0.198	0.18
N10	0.03	1.25	-0.25	1.54	1.51	0.082	0.102	0.147	0.27
N12	1.74	1.09	-1.42	-0.73	4.21	-0.010	0.033	0.076	0.10
N13	0.75	0.70	-1.16	-1.78	2.55	-0.023	0.034	0.093	0.07

Table 2.8: The surface area of the sample cell in kpc^2, the total Lyα flux in emission ($\times 10^{-13}$ erg cm^{-2} s^{-1}), continuum deficit ($\times 10^{-15}$ erg cm^{-2} s^{-1} Å^{-1}), net Lyα luminosity ($\times 10^{41}$ erg s^{-1}), total Hα flux for only the ACS coverage region ($\times 10^{-13}$ erg cm^{-2} s^{-1}), and the Lyα escape fractions for the total galaxy ($f_{Ly\alpha}$), using $F_{+,Ly\alpha}$ ($f_{Ly\alpha,+}$), for just the cells where Lyα is in emission ($f_{Ly\alpha,\Pi}$), and the cell with the highest Hα flux-weighted escape fraction ($f_{Ly\alpha,w}$).

Poor map alignment in some of the larger galaxies, especially the top fifth of N04 and the bottom quarter of N02, result in local values of $f_{Ly\alpha}$ that appear inflated. For most of these targets, the $2'' \times 2''$ cells properly compare the Lyα to co-spatial Hα,

and any misalignments are near the edge in inconsequential locations. In the case of the $f_{Ly\alpha,w} = 1.2$ for N04, however, it appears that the small bright knot in the top center that is the source of the brightest Lyα emission in N04 is at the lower edge of its cell, and the majority of the nearby Hα is in the cell below. This may be accurate, however it may also be the result of a misalignment of slits when constructing the spectral map. This location is coincident with the border between two different days of observation, which are the most misalignment-prone areas. Comparing this region of N04 to neighboring Hα cells shows that $f_{Ly\alpha,w}$ is still ≥ 0.55 for this single knot regardless of the alignment.

2.4.1 Spatial Profiles of Lyα and $f_{Ly\alpha}$

In Figures 2.18, 2.19, and 2.20 we present the corrected Hα emission maps, *HST*/ACS-b band image, Lyα emission and $f_{Ly\alpha}$ maps for the selected galaxies N00, N05, and N09. The remainder are presented in Appendix A. The highest $f_{Ly\alpha}$ values are typically not co-spatial with the brightest line or continuum emission regions. In some cases, these escape fractions exceed unity, even when there is high confidence in the line map alignment (Fig. 2.18). These values could either indicate Lyα resonant scattering out of the star-forming regions before escape, $\mathrm{EW_{Ly\alpha}}$ boosting due to the different Lyα and Hα path lengths [46], or an underestimation of the extinction, and therefore the corrected Hα flux, in these low line-brightness regions. In no case are regions with $f_{Ly\alpha} > 1$ coincident with the brightest Lyα emitting regions, except for

the one cell in N04 discussed earlier.

The escape fraction of Lyα varies greatly within the galaxies. In the case of N09, for instance, $f_{Ly\alpha,\Pi}$, the ratio of the total Lyα to Hα_o for only the cells where there is Lyα emission, is 0.2 and covers 68 out of 112 cells binned to $2'' \times 2''$ (82 kpc^2). This shows that the majority of the galaxy is emitting Lyα, and that if we assume that Lyα is co-spatial with the LyC emission, then the escape fraction is 0.2. When the emitted Lyα is compared to the galaxy-wide Hα_o flux, however, then the escape parameter $f_{Ly\alpha,+} = 0.13$, indicating that there is a roughly equivalent Hα flux in the remaining 44 cells. Therefore, almost half the Hα flux from N09 has no coincident Lyα escape. The highest $f_{Ly\alpha}$ also seems to "shoot the holes" between star-forming knots in the other face-on spiral galaxies, N02, N04, and N08, though not N12.

The cells with the highest $f_{Ly\alpha}$ tend to be in the periphery of N00, N01, N07, N12, and N13. The highest $f_{Ly\alpha}$ in N00 falls between two continuum emitting knots within the galaxy, with apparent $f_{Ly\alpha} > 1$ above and below that zone (Fig 2.19). In N07, the majority of the Lyα emission and biggest $f_{Ly\alpha}$ surrounds the lobe with the lower brightness, in both the optical and FUV, while the brighter lobe has a net continuum deficit (Fig. A.20). N01 has a blue-band continuum deficit only in the brightest continuum cell, while N12 and N13 only have small bands of $f_{Ly\alpha} > 0.1$ at the edges. The merging pair N05 shows a distinct break between $f_{Ly\alpha}$'s ~ 0.1 in the higher metalicity lobe, and ~ 0.25 in the lower metalicity lobe (Fig 2.19). N02 and N08 are net Lyα emitters for one half of the galaxy, but are continuum deficient on

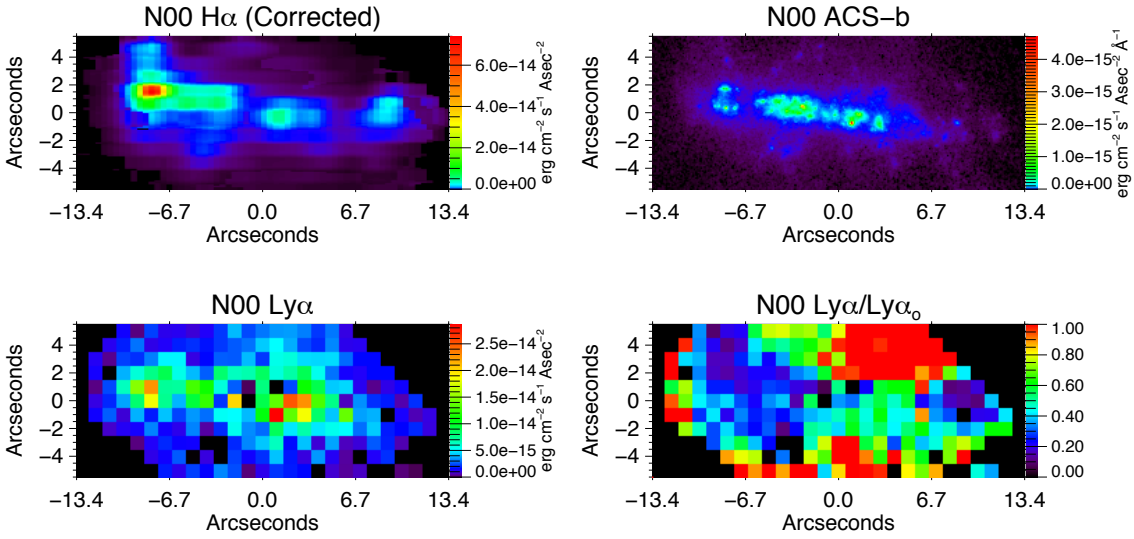

Figure 2.18: Corrected Hα, ACS-b filter, Lyα emission, and $f_{Ly\alpha}$ maps for N00

the other, despite similar extinction, D_n4000, and metalicity on both halves. A $10'' \times 10''$ aperture spanning 30 kpc^2 centered on the eastern half of N08 would measure an escape fraction of 0.19, while that same aperture centered on the western half would conclude that N08 is not a Lyα emitter.

2.4.1.1 Lyα Emission Relative to FUV Continuum

We show in Figure 2.21 that for cells where there is Lyα emission, the Lyα surface luminosity scales with the surface luminosity of the FUV continuum (L_{1416}). We also find that for $L_{1416} > 100 \times 10^{36}$ erg s^{-1} Å^{-1} kpc^{-2}, the proportion of cells that feature net Lyα emission is $\sim 75\%$, while at $L_{1416} < 100 \times 10^{36}$ erg s^{-1} Å^{-1} kpc^{-2} that number falls to $\sim 60\%$. There is a large spread in $f_{Ly\alpha}$ among the individual

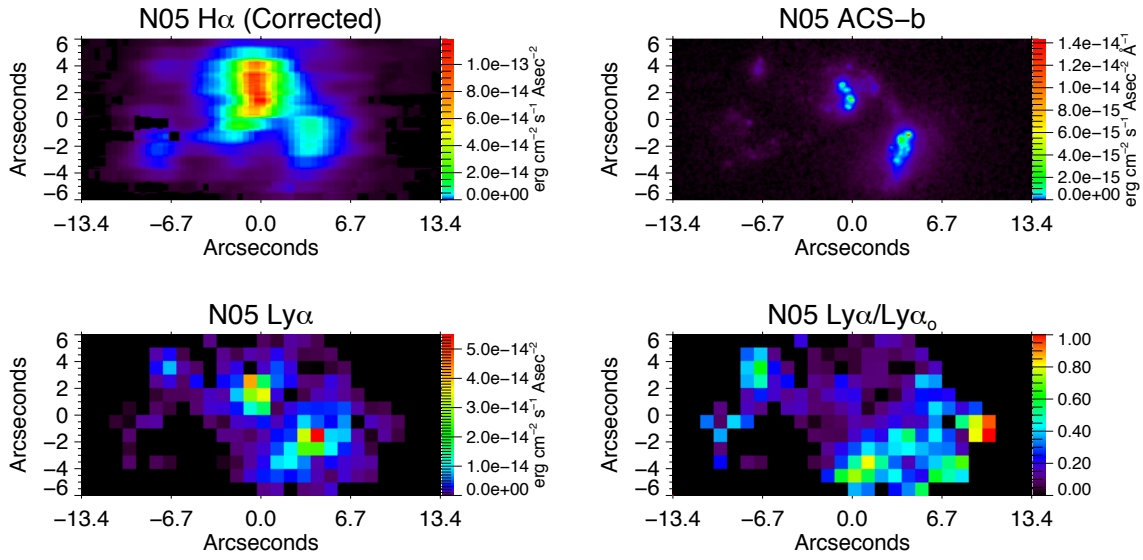

Figure 2.19: Corrected Hα, ACS-b filter, Lyα emission, and $f_{Ly\alpha}$ maps for N05

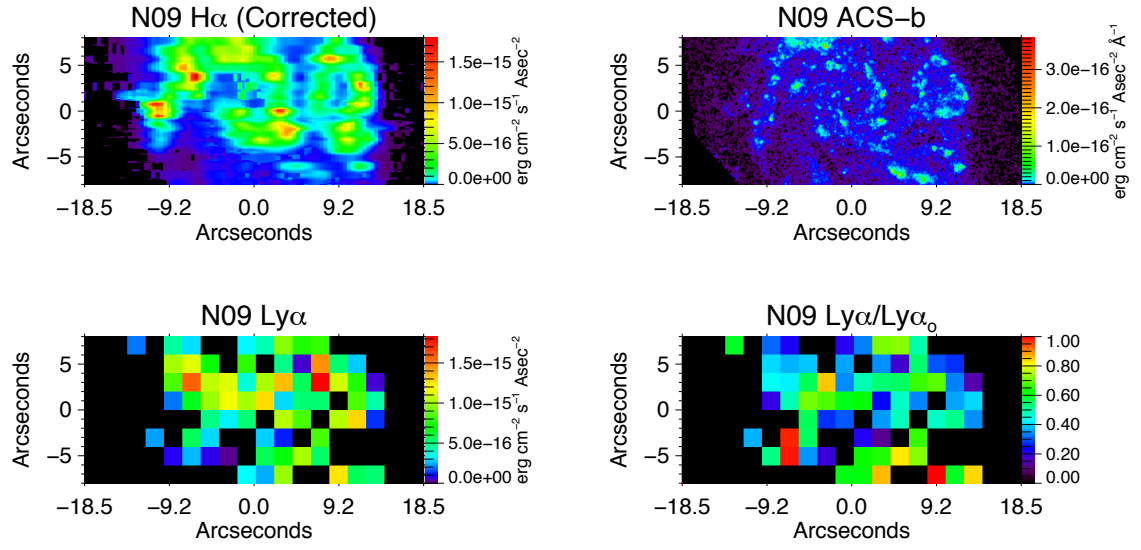

Figure 2.20: Corrected Hα, ACS-b filter, Lyα emission, and $f_{Ly\alpha}$ maps for N09

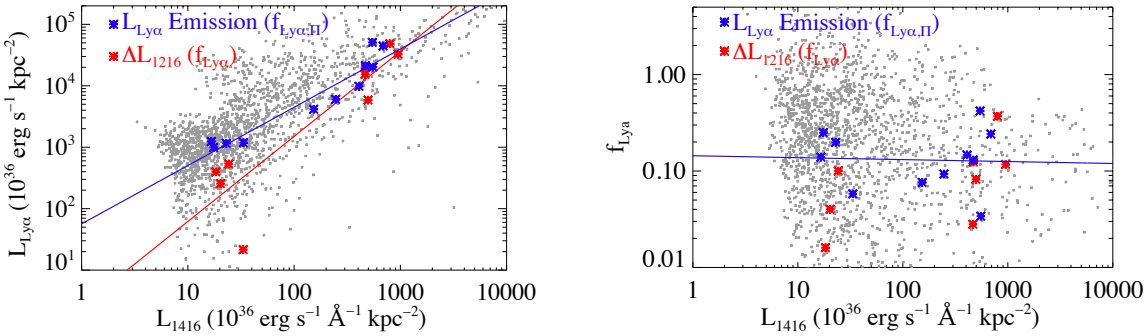

Figure 2.21: (Left) Lyα surface luminosity versus the FUV continuum surface luminosity. (Right) $f_{Ly\alpha}$ versus the FUV continuum surface luminosity. The red points represent the net Lyα for the targets as a whole, while the blue points represent the same, but for only the cells with Lyα emission ($f_{Ly\alpha,\Pi}$). The overplotted lines are the fits to the respective colored sets.

cells in the low continuum regime that appears to converge towards $f_{Ly\alpha} \sim 0.1$ at the brightest emission cells. In total, the top 10% brightest cells in L_{1416} contain 55% of the total $L_{Ly\alpha}$ of our sample.

Wofford et al. (2013) observed 20 targets with the $\sim 2\farcs5$ diameter aperture of *HST*/COS centered on the region coincident with the brightest FUV knot in *GALEX* photometry. They found that 7 of their targets featured net Lyα emission, with $f_{Ly\alpha}$ ranging from 1 – 12%. Based on Fig. 2.21, it would seem that this would be the best strategy for finding and measuring $f_{Ly\alpha}$. If we analyze only the F_{1416} brightest $2'' \times 2''$ cells in our targets, however, we find a higher $f_{Ly\alpha}$ in N02, N05, and N08, but lower in all other targets relative to our galaxy-wide measurements. N01, which has an enormous $f_{Ly\alpha}$ of 0.37, but features a continuum deficit coincident with its brightest cell, would fall to an $f_{Ly\alpha}$ of only 0.042, grossly underestimating the true

value. $f_{Ly\alpha}$ for N05 would flare from 0.028 to 0.125. In total we would be left with only 6 out of 11 targets being net Lyα emitters, when in fact 8 are. Our range of $f_{Ly\alpha}$ would fall from a maximum of 0.37, with 4 targets having $f_{Ly\alpha} \geq 0.1$, to a maximum $f_{Ly\alpha} = 0.127$ in N08 (which has a galaxy-wide $f_{Ly\alpha}$ of only 0.04), and only N05 and N08 having $f_{Ly\alpha} > 0.1$, neither of which do galaxy wide. While it is possible that the FUV-brightest region might dominate the Lyα emission of a galaxy, it does not appear that brightness is a reliable tracer of Lyα escape. This can be seen in the Lyα emission map of N09 (Figure 2.20), where the FUV-bright knots in the northern and southern regions have no net Lyα emission coincident with them, but the bright knots to the northwest and in the center are strong Lyα emitters.

2.4.1.2 Color-Luminosity and Color-$f_{Ly\alpha}$

A plot of $L_{Ly\alpha}$ versus the m_{1416} - m_{1610} color, which is related to β_{gr}, shows the emission tends to be strongest in very blue (m_{1416} - $m_{1610} < 0.3$) regions, however there is a long extension of Lyα emission towards redder colors. The galaxies follow a fairly defined line on the blue side of the locus for the total net $L_{Ly\alpha}$, but the targets are pushed redward when only the positive emission cells are considered ($f_{Ly\alpha,\Pi}$). This indicates that in those targets with cells featuring significant continuum deficit, that a significant portion of the Lyα emission is from cells that have a redder color than the galaxy average. In every case except N01 and N05, choosing only cells that have a net positive Lyα emission resulted in a redward shift in the color.

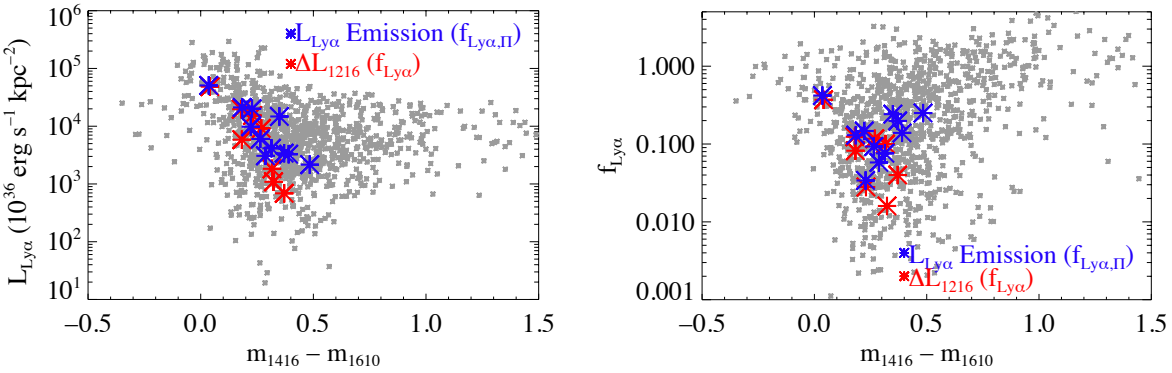

Figure 2.22: $L_{Ly\alpha}$ and $f_{Ly\alpha}$ versus the G-R color, which is proportional to β_{gr}.

2.5 Comparison of Results

Analysis in this sub-section is carried out by condensing the relations we have calculated into the same cells as the Lyα and $f_{Ly\alpha}$. We analyze only cells with an uncorrected $EW_{H\alpha} > 10$ Å and an $EW_{H\beta} > 2$ Å so as to reduce the uncertainty introduced by the stellar absorption correction. We focus here on local variations of properties within the targets and how those local variations compare to the rest of the sample, not the relationship between these properties on the galaxy level and the total $f_{Ly\alpha}$, which can be easily done by looking at Table 2.8.

2.5.1 Correlation with Metalicity

Both the ([OII] + [OIII])/Hβ and the [NII]/Hα derived metalicites ($Z_{[NII]/H\alpha}$) show a wide distribution of $f_{Ly\alpha}$ across the majority of the metalicity range. Fig-

ure 2.23 shows a histogram of the proportion of each $\Delta Z_{[NII]/H\alpha}$ =0.1 bin that has $f_{Ly\alpha} > 0.1$, relative to all selected cells, even if there is no net positive Lyα emission in that cell. Greater than 70% of the cells in our sample with an [NII]/Hα derived $Z_{[NII]/H\alpha} < 8.3$ have $f_{Ly\alpha} > 0.1$, with only 15% of cells registering no Lyα emission. For $Z_{[NII]/H\alpha} \geq 8.5$, these properties change to $\sim$ 31% and 32% respectively. All three galaxies that have a global $Z_{[NII]/H\alpha} < 8.3$ have $f_{Ly\alpha} > 0.1$, while only N09 does among the $Z_{[NII]/H\alpha} \geq 8.3$ galaxies.

In theory, if $f_{Ly\alpha}$ and f_{esc} are anti-correlated with higher galaxy mass [32], and mass follows metalicity [70], then we should expect $f_{Ly\alpha}$ and f_{esc} to trend down with increasing metalicity. The individual cells in our sample show that the probability of a region to be a net Lyα emitter may be greater at low $Z_{[NII]/H\alpha}$, but that $Z_{[NII]/H\alpha}$ does not define the Lyα emission or the escape fraction.

2.5.2 D_n4000

In a similar manner to the metalicity, we find that for low $D_n4000 \leq 0.9$, escape fractions are ≥ 0.1 for 60% of cells, and that 17% of the cells have no net Lyα emission. For $D_n4000 \geq 1.1$, these proportions move to 42% and 38% respectively. At the galaxy-wide level, however, the low D_n4000 galaxy N02 is not a Lyα emitter, while the high D_n4000 galaxy N09 has $f_{Ly\alpha} \sim 0.1$. Some of the highest $f_{Ly\alpha}$ and Lyα fluxes in N09 come from central regions with $D_n4000 > 1$, but are near cells with no net emission (Fig. 2.20). Stellar age (D_n4000) and metalicity are therefore not

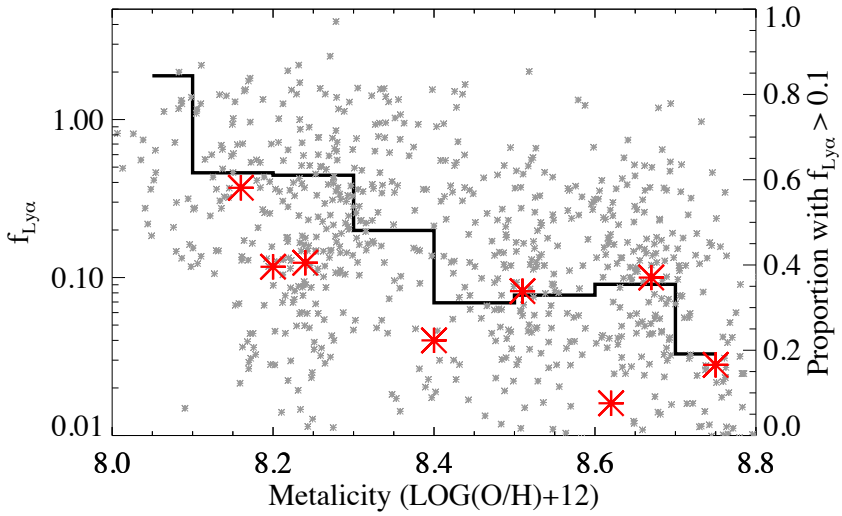

Figure 2.23: A histogram of the number of cells with $f_{Ly\alpha} \geq 0.1$ out of the total number of cells with $EW_{H\alpha} \geq 10$ Å and $EW_{H\beta} \geq 2$ Å. The raw cell values (grey) and the total values for each target (red) are overplotted.

predictors of $f_{Ly\alpha}$, but could potentially be used to bias a sample towards higher or lower $f_{Ly\alpha}$, and potentially towards a greater proportion of net Lyα emitters.

2.5.3 Lyα Equivalent Width

The typical estimate of the intrinsic $EW_{Ly\alpha}$ (presented as positive in emission for simplicity) is between 80 – 240 Å. For 89% of the cells with Lyα in emission, we measure $EW_{Ly\alpha}$ to be <240 Å. Six of our targets (N00, N01, N07, N10, N12, and N13) have at least one cell with $EW_{Ly\alpha} > 200$ Å, with N00, N01, N07, and N10 having multiple cells with $EW_{Ly\alpha} > 300$ Å. In N13, four of the six cells with $EW_{Ly\alpha} > 200$ Å are clustered together at the edge of the galaxy. For all of our targets we find

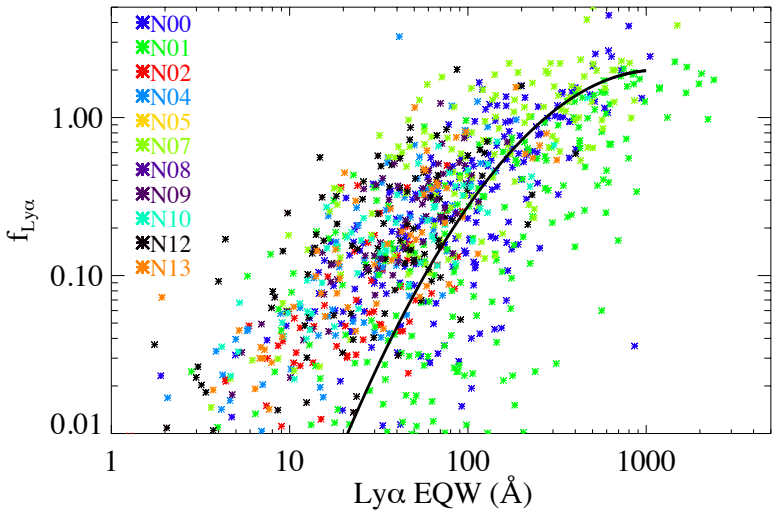

Figure 2.24: A plot of $f_{Ly\alpha}$ versus $\mathrm{EQW_{Ly\alpha}}$ for each target, with a fit line overlay

that $f_{Ly\alpha}$ roughly increases with $\mathrm{EW_{Ly\alpha}}$ (Fig. 2.24). The scatter prevents establishing a meaningful correlation, however we can set soft limits of $f_{Ly\alpha} < 0.3$ for $\mathrm{EW_{Ly\alpha}} <$ 10 Å, and $f_{Ly\alpha} \sim 1$ for $\mathrm{EW_{Ly\alpha}} > 300$ Å. The regions with $\mathrm{EW_{Ly\alpha}} > 300$ Å may be evidence of equivalent width "boosting" by the resonant scattering of Lyα off of the surfaces of dense clumps en route to escaping, therefore encountering a lower total dust and gas column density than the continuum and Hα emission [46].

2.5.4 Star Formation Rate

Previous studies have shown that the $\mathrm{EW_{Ly\alpha}}$ decreases with the uv-derived SFR [71, 72]. A plot of $\mathrm{EW_{Ly\alpha}}$ versus the Hα derived SFR density (Σ_{SFR}) confirms this

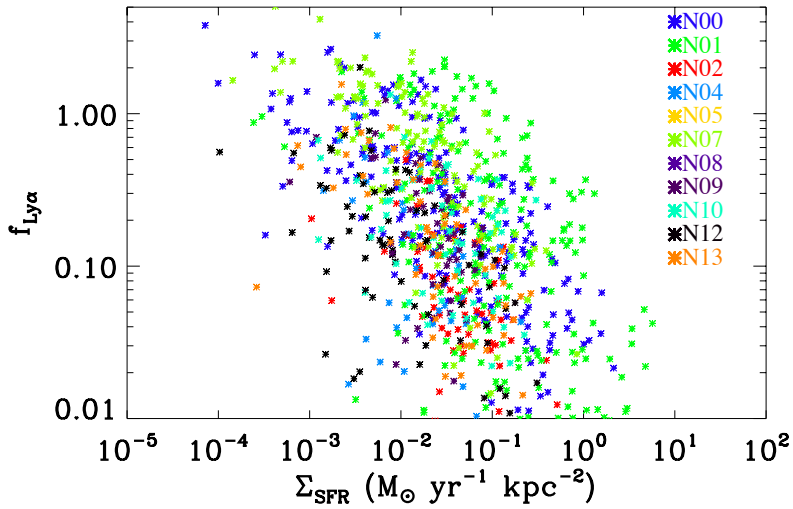

Figure 2.25: A plot of $f_{Ly\alpha}$ versus the SFR density.

relation on $1'' \times 1''$ scales, albeit with large scatter. If $f_{Ly\alpha}$ increases with increasing $\mathrm{EW_{Ly\alpha}}$, and $\mathrm{EW_{Ly\alpha}}$ decreases with increasing Σ_{SFR}, then $f_{Ly\alpha}$ should decrease with increasing Σ_{SFR}. This is weakly shown in Figure 2.25. While a number of factors are used to calculate our SFR, it is well correlated to the much simpler Hα luminosity dependant SFR from Kennicutt (1998) [14]. Therefore, a relationship between $f_{Ly\alpha}$ and Σ_{SFR} is really a relationship between the Lyα emission and the intrinsic and observed Hα emission.

2.6 Discussion

We surveyed 12 objects with the *HST*/ACS-SBC and *APO*-DIS. Using the slopes of the FUV continuum, we extracted the net Lyα emission or absorption for each target on scales of $1'' \times 1''$ for compact sources, and $2'' \times 2''$ for the extended objects. The optical spectral maps were assembled into aligned data cubes that, with a few noted exceptions on the extended objects, accurately matched the *HST* photometry at the $1'' - 2''$ scale. We constructed emission line and spectral diagnostic maps in order to probe the behavior of $f_{Ly\alpha}$ within each galaxy.

2.6.1 Spatial Variation of $f_{Ly\alpha}$

We have shown that in order to determine the Lyα luminosity of a galaxy, the entire galaxy must be measured. While we have been able to make estimates as to what optically derived properties of a galaxy region might increase or decrease the probability of detecting Lyα emission, we have not found evidence for a clear $f_{Ly\alpha}$ indicator, nor any way to extrapolate the properties of one region of the galaxy to the galaxy as a whole.

We also cannot point to any particular morphology that can be defined in terms of $f_{Ly\alpha}$. In the merging pair in N05, the Lyα emission appears to come from in and around the bright FUV continuum regions. For the merging pair N07, however, the bulk of the Lyα flux comes from the area between the two lobes at apparent $f_{Ly\alpha} > 1$,

while the brightest FUV-continuum region, which has the brightest spectral lines in our sample, clear Wolf-Rayet features, low metalicity and D_n4000, and relatively low extinction, is not a net Lyα emitting region. In the spiral galaxies N02 and N08, the vast majority of the Lyα emission comes from one side of the galaxy, while the other half of the galaxy features almost no emission at all. If only the right-half of N08 is considered (Fig. A.21), which spans an angular area as large as N01, $f_{Ly\alpha}$ skyrockets from 0.04 to 0.185. In N12 the Lyα emission is a mixed bag of emission from bright continuum regions, a large continuum deficit in the brightest FUV continuum region, and a large amount of Lyα from an inexplicably optically quiet region at the very top. In N09, the only face-on spiral with a large $f_{Ly\alpha}$, the Lyα emission seems to come from everywhere but where there is star-formation, except for the region where there is the most star-formation, where $f_{Ly\alpha}$ is a respectable 0.18.

These contradictory findings lead to the conclusion that the mechanisms that govern $f_{Ly\alpha}$ are very local to the emission region and viewing geometry.

2.6.2 Possible Implications for f_{esc}

In most cases, the brightest FUV-continuum regions are not the regions with the highest $f_{Ly\alpha}$ (with N05 being a very notable exception). Our $f_{Ly\alpha,w}$ parameter, which aims to pick out the highest Hα flux weighted $f_{Ly\alpha}$, could be a useful starting point for future LyC observations. With the exception of a potentially poorly aligned cell in N04, no $f_{Ly\alpha,w}$ is > 0.5. If the escape mechanisms along a particular line-of-sight

are identical, then $f = f_{Ly\alpha} = f_{esc}$. For where the $f_{Ly\alpha,w}$ is coincident with a bright continuum emitting region, as in N05, then from equation 1.2 and $f_{Ly\alpha,w} = 0.05$, we would expect $L_{Ly\alpha} = 0.032Q$ with $Q \approx 28.0 \times 10^{41}$ erg s^{-1} from that single square arcsecond region. For the higher $f_{Ly\alpha,w}$ of 0.37 in the compact galaxy N01, where there is no Lyα emission coincident with the strongest FUV continuum region, but a great deal surrounding it, $Q \approx 9.0 \times 10^{41}$ erg s^{-1} if $f_{Ly\alpha} = f_{esc}$. Measurements of the LyC flux and f_{esc} from these two bright, but fundamentally different, regions would greatly illuminate the understanding of how these properties relate.

2.6.3 Conclusions

We conclude from this study that the amount of Lyα escape varies tremendously depending on the observation sightline, with significant Lyα emission in the periphery of the galaxies. Therefore, it is critical to cover the entire target when searching for global relationships that can meaningfully be applied to high redshift observations. It is unknown whether the unpredictable emission characteristics of Lyα escape in spiral galaxies is the result of direct escape from low-luminosity, low density regions, or the result of resonant scattering from nearby star-forming regions shifting the apparent Lyα source to these inter-spiral arm areas. Establishing direct measurements of f_{esc} with *HST*/COS from a selection of regions in this study with a well defined $f_{Ly\alpha}$ will help to clarify both the relationship between $f_{Ly\alpha}$ and f_{esc}, and the effect of resonant scattering on Lyα emission.

Chapter 3

FORTIS

3.1 Introduction

The Far-uv Off Rowland-circle Telescope for Imaging and Spectroscopy (FORTIS) is an entirely new spectroscopic telescope developed by the Johns Hopkins University sounding rocket group [29, 73]. FORTIS is a far-UV sensitive f/10 Gregorian specro-telescope featuring a diffraction grating holographically ruled directly onto the secondary mirror (Fig. 3.1). This unique design produces redundant off-axis dispersed channels on either side of a zero-order imaging channel, greatly improving the efficiency and spectral multiplexing capabilities of FORTIS relative to that of a traditional longslit spectrograph and telescope. Multi-object spectral acquisition capability is provided by a *James Webb Space Telescope* (JWST) *NIRSPEC* prototype microshutter array (MSA) positioned at the focus of the primary mirror that acts

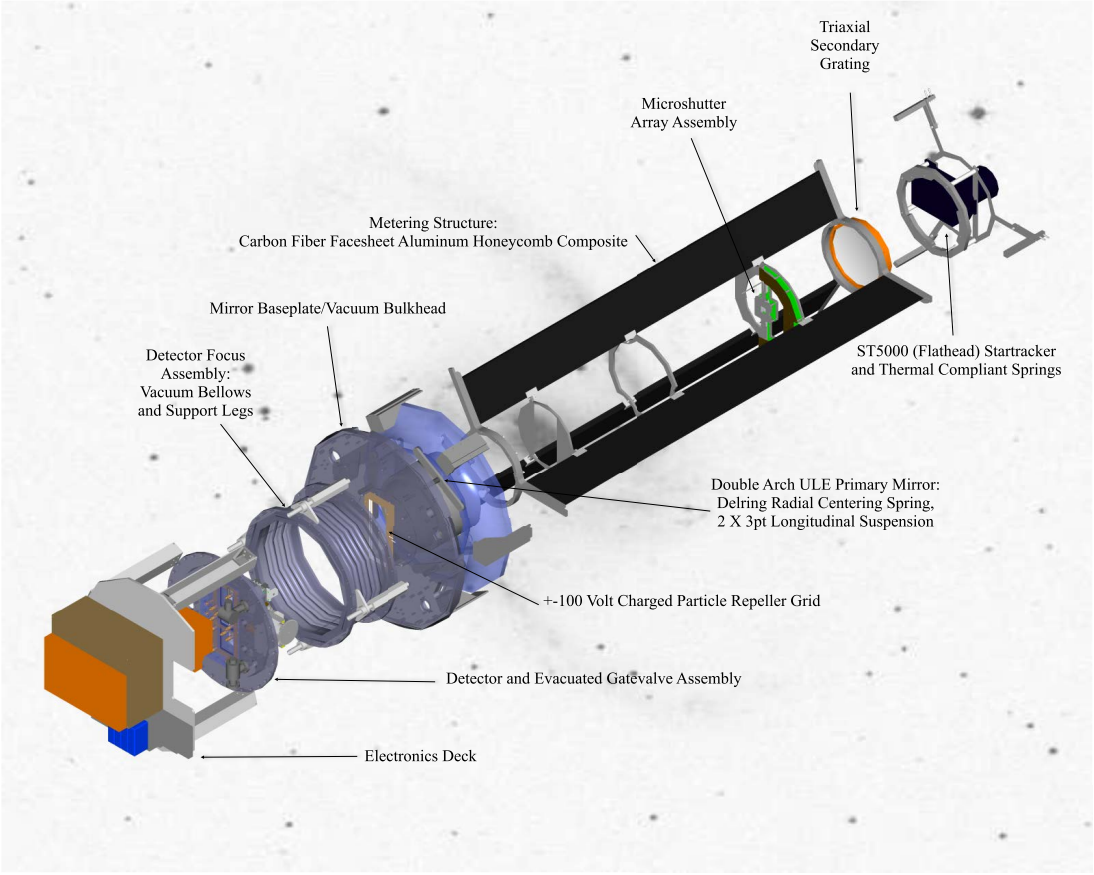

Figure 3.1: Rendered exploded drawing of FORTIS with major components labeled.

as a reprogrammable slitmask [74]. The imaging channel is analyzed "on-the-fly" by an onboard Field Programmable Gate Array (FPGA) module to select observation targets in real-time and address the MSA.

The novel optical design gives FORTIS an effective area approximately twice that of *Hopkins Ultraviolet Telescope* – Astro-2 (HUT) [75], with only half the primary mirror diameter. The large 0.5° FOV and multi-object spectral capability enables

the study of extended objects in ways that were too time consuming for *FUSE* or *HST/COS*. Operating in the 800 - 1800 Å bandpass with a design resolving power of R $\sim$ 1500 and the ability to take simultaneous spectra of up to 43 objects at once, FORTIS is ideally suited to study Lyα escape from z $>$ 1200 km/s galaxies, and to serve as a pathfinder mission for enabling observations of the Lyman Continuum as well.

The first components of FORTIS were delivered in 2008 and fabrication began in 2009. Detector interface testing occurred in April 2011 and handshaking with NASA telemetry systems in December 2011. Full fabrication was completed in May 2012 and the first environmental testing took place at NASA Wallops Island Flight Facility (WFF) in August 2012. Environmental testing and integration with NASA Sounding Rocket Operations Contractor (NSROC) equipment was successfully completed in January of 2013. The maiden launch of FORTIS took place May 10, 2013 from White Sands Missile Range (WSMR). This chapter will cover the design, fabrication and calibration of FORTIS up to the date of shipment to WSMR. Preparation for launch and the results of the first flight will be covered in Chapter 4.

3.2 Optics

Reflectivities for mirrors in the FUV down to the Lyman limit (∼912 Å) are rarely better than 30 – 40%. This presents unique challenges in the design of a far-uv instrument, as a typical "three-bounce" telescope-plus-grating optical design will reduce the collected number of photons by $\geq 95\%$ before any light reaches the detector. The FORTIS design mitigates this effect by recording the grating directly onto the secondary mirror, thus removing one reflection and increasing the optical throughput by a factor of three. The tri-axial figure of the secondary corrects for the aberrations in the spectral orders caused by a concave grating figure, but introduces a point- source astigmatism into the imaging order. A cylindrical CaF_2/MgF_2 doublet lens positioned on-axis corrects the imaging channel astigmatism and provides a low wavelength cutoff at $\lambda \leq 1250$ Å to avoid contamination by geocoronal Lyα. The dual spectral order redundancy affords another factor of two in efficiency [76]. This section will cover the testing history of the individual optics, starting with the optic fabrication and coating (§3.2.1) and then the grating and corrector lens imaging (§3.2.2) and spectral performance (§3.2.3). A description of the end-to-end focusing and alignment of the fully constructed telescope is presented in §3.6.1 along with the other end-to-end testing. A summary of the parameters of the two mirror optics is presented in Table 3.1.

3.2.1 Optic Fabrication and Coating

The FORTIS primary mirror was fabricated by D.A. Loomis Custom Optics and delivered to JHU in 2007. The secondary substrates were fabricated by Precision Asphere in 2010. The grating was holographically recorded onto the secondary substrates at Horiba Scientific by applying a photoresist material and exposing it to the fringes of two coherent laser beams to produce the grooves, and then overcoated with platinum. The CaF_2/MgF_2 achromat was delivered in January 2012. The primary mirror was coated at NASA *Goddard Space Flight Center* (GSFC) in March 2012 with a SiC over Al coating, while the Pt-coated gratings were overcoated with just SiC. A set of three witness samples were also coated, and one was installed in FORTIS to act as a proxy for the primary mirror.

Measurements of the witness sample reflectivity and achromat transmission was carried out using the JHU *Calibration and Test Equipment* (CTE) [77]; a vacuum far-uv monochrometer illuminated by a windowless hollow cathode gas discharge lamp for wavelengths ≤ 1608 Å, and a PtNe lamp for longer wavelengths. The witness sample was mounted approximately at the focus of the monochrometer at a slight angle to reflect the beam away from the incident axis. A photomultiplier tube (PMT) mounted to a lever-arm stage centered on the mirror intercepts the beam in order to measure the incident monochromatic light intensity, then is moved off to the side and rotated $\sim 180^\circ$ to measure the reflected intensity (Fig. 3.2). The reflectivites of the primary mirror witness sample are presented in Figure 3.3, along with the transmission of

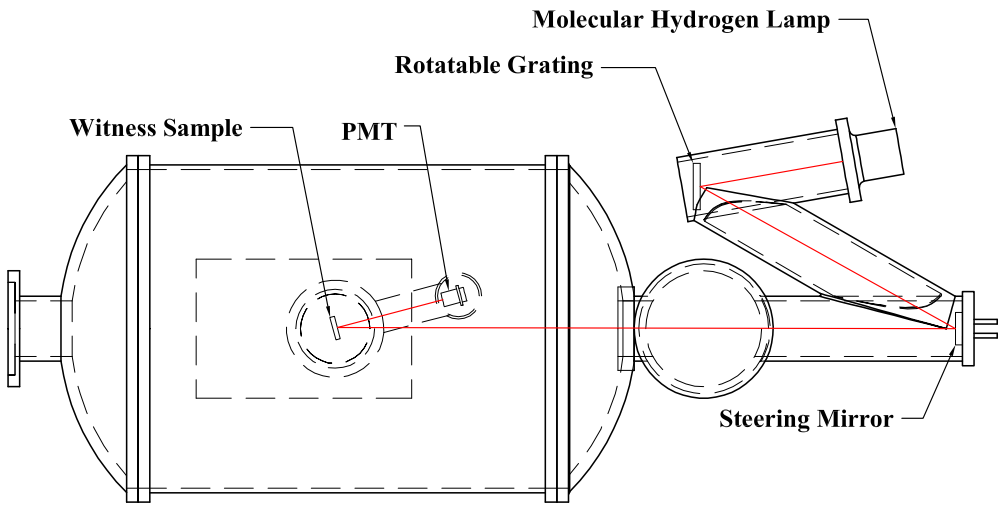

Figure 3.2: Schematic drawing of the CTE when setup for measuring the reflectivity of the primary mirror witness sample. Light from the H_2 lamp diffracts off of a rotatable grating towards a steering mirror which directs the monochromatic beam towards the angled witness sample. The PMT is on a rotatable stage and can move to intercept the beam and measure it both directly and in reflection.

the cylindrical CaF_2/MgF_2 imaging corrector lens, which was measured in the same manner, but with the PMT positioned behind the lens to measure transmission.

3.2.2 Imaging Performance

Each bare substrate was installed onto a custom optical bench at JHU consisting of a mirror mount approximately 312.5 mm from a 5 μm pinhole light source centered on the optical axis. This setup produced a pair of 5× magnified focii beginning at ∼1562.5 mm from the vertex, each a horizontal or vertical rectangle as the light rays from the different axis focus at different locations. This simulates the optical setup

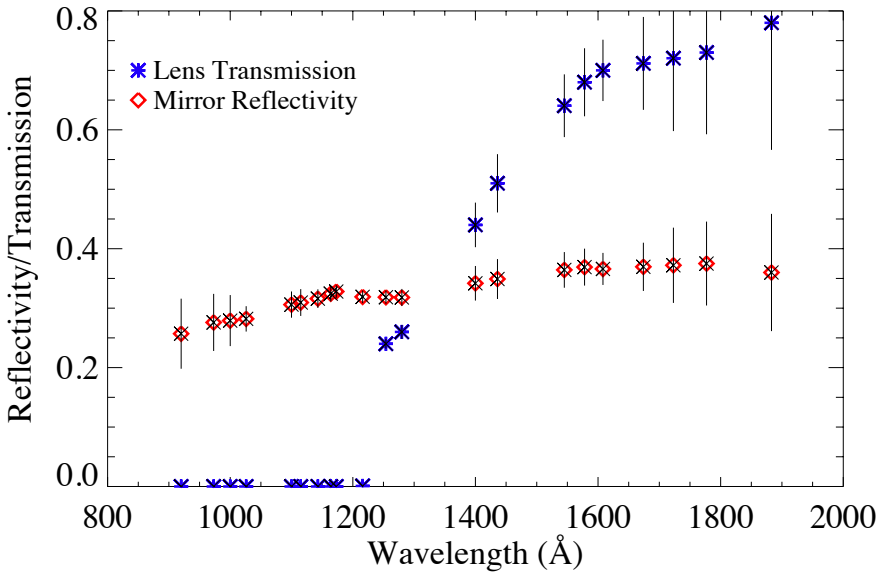

Figure 3.3: Lens transmission and measured primary mirror witness sample pre-flight reflectivity after SiC over Al coating

of FORTIS from the microshutter array at prime focus to the detectors (Table 3.1). A SCION CFW-1612M 12-bit monochromatic CCD mounted to a 3-axis precision stage was used to capture images and sweep through the focii. The astigmatism of the secondary substrates were measured and found to conform to expectations, with tangential and sagittal focii occurring ~ 2.5 mm apart in the flight configuration with full-widths at half-maximum (FWHM) of $1\farcs03$ and $1\farcs23$ respectively in visible light (Fig. 3.5). A raytrace simulation of the test setup, including obscurations, predicted that the FWHM of the minor axis of each focus should be $1''$.

The cylindrical corrector doublet acts to change the vertical focus position of the light rays to match the horizontal focus position. The lens is positioned $\sim$52 mm

from the imaging order detector and consists of a 4.05 mm thick (at thickest point) MgF_2 lens with one face flat and the other with a radius of 96 mm, and a 3.56 mm thick CaF_2 lens with an inverse 96 mm radius to match the MgF_2 on one face and a 292 mm radius on the other (Fig. 3.4). Light from the grating enters the doublet at the flat face of the MgF_2 and exits to towards the imaging detector from the R=292 mm face of the CaF_2. When corrected, the flight secondary produces a spot with a slight "C" shape and a FWHM of $\sim 1\farcs75$ (Fig. 3.5).

The secondary grating and achromat were integrated with the primary mirror into the telescope structure in May 2012. A 15" diameter air collimator illuminated by a 7.5 μm pinhole light source was used to illuminate the telescope for alignment and focusing. The alignment of the telescope was set by determining the best focus for a given configuration, and then applying shims to the secondary mirror mount to center the focus and move the focal point closer to the detector plane. Raytrace estimates using the defined optical specifications predicted a FHWM of the fully built telescope at the center of the corrected imaging order of $1\farcs5$, however the combined telescope could not be aligned to produce a spot smaller than $4''$. The enlarged point spread function (PSF) was traced to the primary mirror. It has yet to be determined whether these errors are caused by the mounting fixture or are native figure errors in the primary (Fig. 3.5). The alignment of the telescope was adjusted so that the FWHM in the dispersion direction was minimized, resulting in a tail-like coma in the spatial dimension.

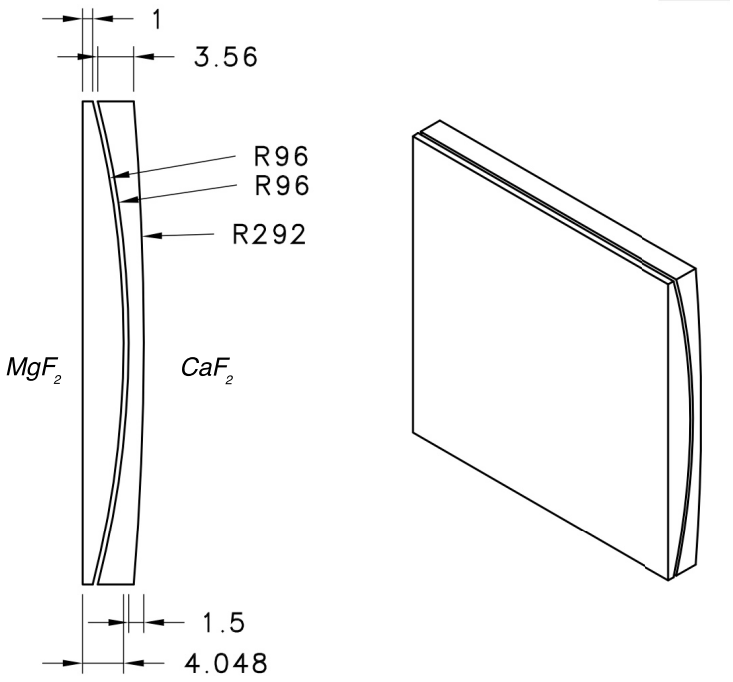

Figure 3.4: Drawing of the cylindrical MgF_2/CaF_2 achromat lens. All measurements in millimeters

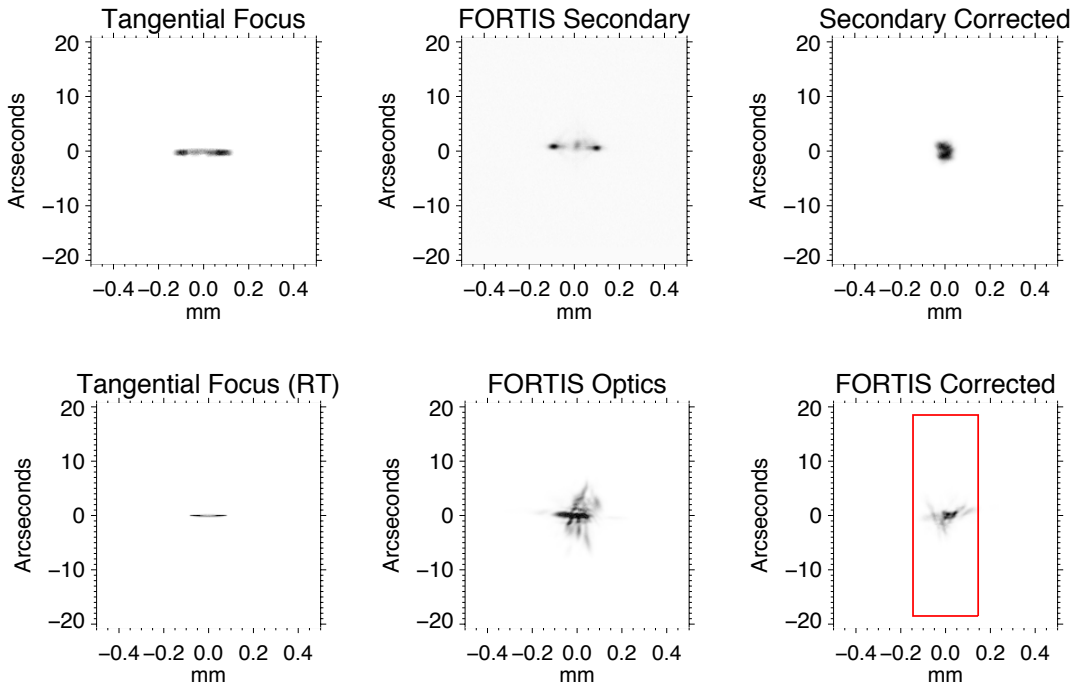

Figure 3.5: (TOP) FORTIS Secondary grating images from a 5 μm pinhole illumination in the optical test bench in (LEFT) Raytrace, (CENTER) measured image, (RIGHT) corrected by the cylindrical lens. (BOTTOM) Full FORTIS telescope illuminated by a 7.5 μm pinhole source through an air collimator (LEFT) Raytrace, (CENTER) measured image, (RIGHT) corrected by the cylindrical lens with a microshutter aperture overlay.

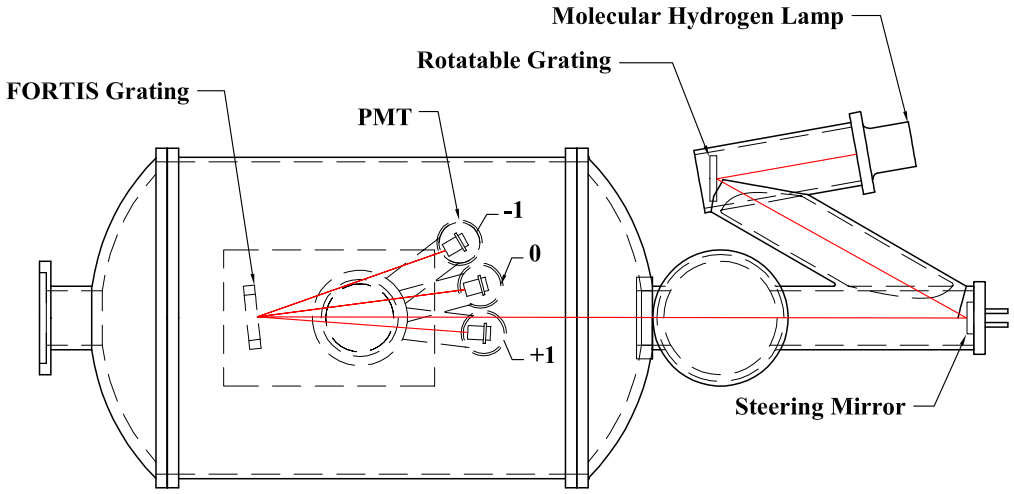

Figure 3.6: Schematic drawing of the CTE when setup for measuring the grating efficiency. The three PMTs show the three different positions needed to measure the 0-order and ±1 order diffracted light. Not shown is the incident position (intercepting the beam) and the ±2 orders.

3.2.3 Spectral Performance

Grating efficiencies were measured in the CTE (see §3.2.1) using a similar calibration strategy as was used to measure the primary mirror reflectivity. The grating was placed at an angle such that the PMT could be maneuvered to measure the 0, ±1 and ±2 spectral orders at all wavelengths between 920-2000 Å without vignetting the incident beam (Fig. 3.6). The results for the designated flight grating are presented in Figure 3.7. The second grating was less than half as efficient in the FORTIS bandpass and therefore was designated the backup grating and may be returned to the vendor in the future to be re-ruled.

The efficiencies measured are somewhat lower than the design goal, and the

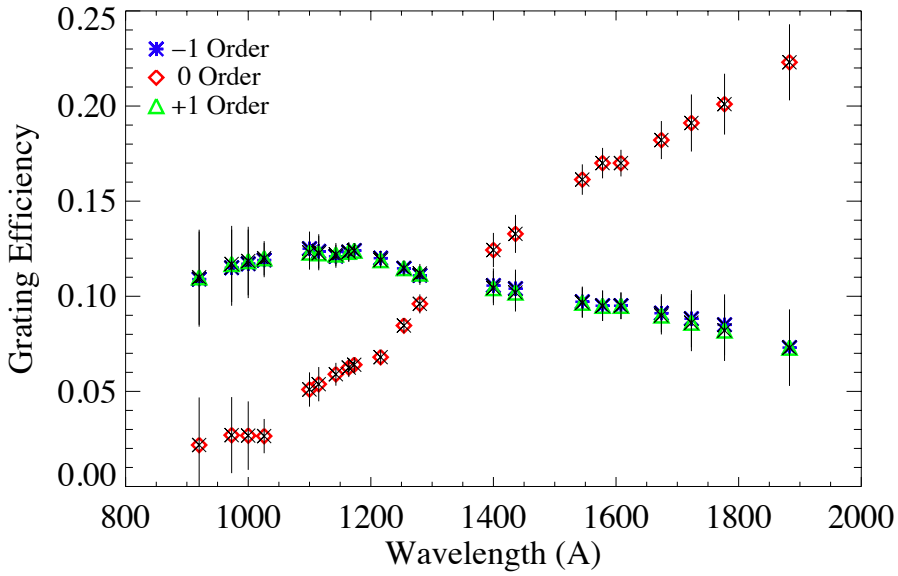

Figure 3.7: Grating efficiency for the flight grating in 0 and ±1 spectral orders

crossover point where 0-order and ±1 spectral orders are equally efficient occurs ∼1300 Å instead of the target ∼1620 Å. These measurements imply that the ruling depth of the flight grating is ∼210 Å rather than the target 250 Å. A measured 0.008 efficiency in ±2 order at 1216 Å also suggests that the grove profile is not laminar, as a laminar grove profile should suppress the even spectral orders [78]. The end-to-end spectral imaging performance of FORTIS is presented in §3.6.1.

3.3 Detectors

The FORTIS science data is recorded by three cross delay line (XDL) microchannel plate (MCP) detectors with CsI photocathodes manufactured at Sensor Sciences LLC [79] and delivered in June 2011. These XDL MCPs operate by accelerating photoelectrons generated at the cathode through the channels, where they multiply by several orders of magnitude as the electrons impact the high impedance channel walls. The resulting electron cloud impacts on a grid of upper and lower charge collectors at the anode, and the signal feeds into two sets of delay lines. A zener diode and low pass filter fixes the common output of the three MCPs to -600 V with respect to the XDL anode, which sits at ground (Fig. 3.8). The difference in arrival time of the signal in each set of delay lines is proportional to the centroid of the charge cloud in that dimension, resulting in X and Y coordinates for each detected photon. A signal indicating the total amount of charge received on the anode, or the pulse height (PH), is also generated. The PH is useful for separating photon counts, which have a Gaussian-like distribution with a centroid defined by the applied voltage, from ion events or dark counts. The electronic readout is fast, enabling global countrates $\sim 10^6$ counts s^{-1}, however local countrates are limited by the rate at which the charge can replenish on the plates. Each of the three FORTIS science detectors are large format MCPs, with operational properties listed in Table 3.2.

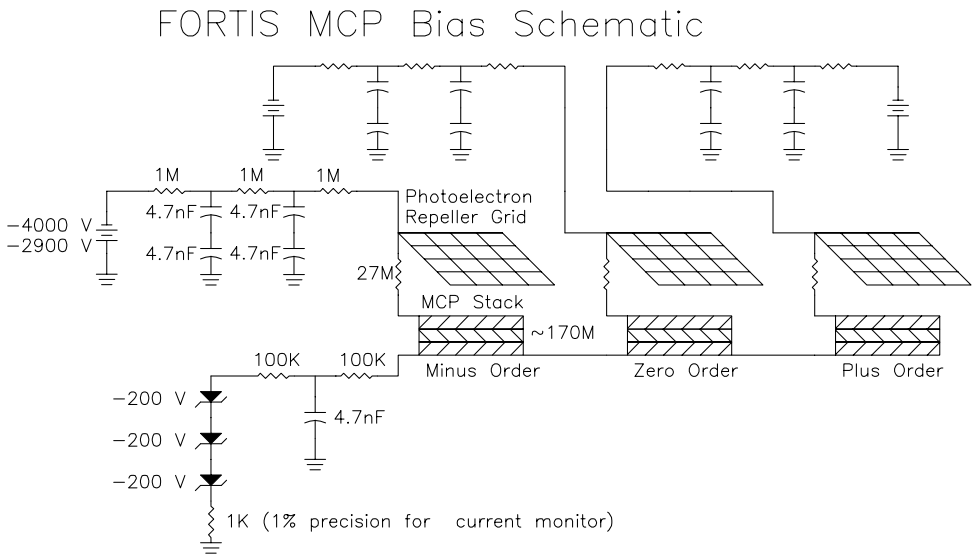

Figure 3.8: Schematic diagram of the MCP HV and biasing

3.3.1 Detector Operation

The CaF_2 in the corrector lens has a spectral cutoff shortwards of ∼1250 Å, however the spectral channels are sensitive down to 800 Å and are at risk of saturation by geocoronal Lyα. The Lyα brightness of the night sky is generally between $I_{Ly\alpha}$ = 2 – 4 kRayleighs, producing a photon radiance on each FORTIS spectral detector of:

$$L_{\pm 1} = \frac{\alpha_{sr}\Theta_{MSA}\epsilon_{1216,\pm 1}R_{pm}I_{Ly\alpha}(r_o^2 - r_i^2)}{4}10^6 \tag{3.1}$$

Where α_{sr} is the 0.5° FOV in steradians, Θ_{MSA} the open area ratio of the MSA (∼0.73, §3.5), $\epsilon_{1216,\pm 1}$ the grating efficiency of the first spectral orders at Lyα, R_{pm}

the reflectance of the primary mirror, and r_o and r_i the outer and inner radii of the primary mirror, in centimeters, respectively. For the values listed in Table 3.1, and from Figures 3.7 and 3.3, and a Lyα geocoronal brightness of 4 kRayleighs, the number of photons incident on each of the two spectral MCP detectors when the MSA is open is $\sim 1.8 \times 10^6$ photons s^{-1}.

To protect the detectors, the spectral channels are deactivated during the image acquisition phase by setting the high voltage (HV) to a standby level of approximately -2900 volts; the maximum potential possible without activating the channel plates. The standby state prevents the deactivated plates from floating to the zener voltage and causing field emission between the active imaging and the deactivated spectral channels.

Each of the three detectors is powered by individual custom made variable HV power supplies developed by the *Instrument Development Group* (IDG) at JHU. The HV level for each detector is set individually based on the centroid of the PH distribution (PHD) for an FUV light source. Optimum values were determined by tuning the voltage until the centroid was located at $\sim$32% of the maximum pulse height range; $\sim$5 and 20 for the spectral and imaging channels respectively (see Table 3.2).

3.3.2 Detector Interface

Pulses generated by the XDL anode are read into an amplifier and time-to-amplitude converter (TAC) system developed by Sensor Sciences, and output simul-

taneously as a set of three data words per channel, with 13 active bits representing each coordinate of the data event on an X,Y plane, and 4 active bits indicating the PH (the imaging order position data words are 12 bits and the PH 6 bits). The MCP area does not fill the entire electronic resolution, however, so the total number of active resolution elements is smaller (see Table 3.2). This yields a resolution of 13.1 $\times$ 13.9 μm/pixel in the imaging order and $\sim$ 10.5 $\times$ 7.6 μm/pixel in the spectral orders. The data is routed through a custom multiplexor (MUX) designed by the IDG and reordered to present a sequence of two 15+1 bit data words per event, 13 (12) data bits and 2 (3) PH bits, which are recorded into a FIFO for readout. The 16th bit is a "control" bit assigned by the MUX to delineate between X and Y data words. Each of the three channels is fed into an identical, but independent, MUX and FIFO system.

During flight, the telemetry (TM) module of the payload will clock each of the FIFOs at a rate of 125 kHz, allowing a maximum science data countrate of 62,500 counts s^{-1} $channel^{-1}$. A set of three National Instruments PCIe-6536 Digital I/O cards read the data into a ground service computer that screens the counts and organizes the bitstreams into (X,Y) coordinates and PH values, and assigns a time tag for each photon event to be written out to a file for storage. This system operates in two modes, flight mode and calibration mode. In flight mode, the data is processed in real-time by an IDL GUI running in parallel and images of the three detectors are displayed on screen as they accumulate, along with basic statistics, plots of the PHD,

a plot of the extracted brightest spectra, and a full resolution image of the brightest portion of the imaging detector. This computationally intensive mode requires a significant dead-time correction at high countrates to accurately determine the incident flux.

The linearity of the data acquisition system was tested by mounting the detector at the end of the main chamber of the CTE and illuminating it with a beam of Lyα photons, determining the measured countrate, and then directing the beam to a calibrated EMR 542G photomultiplier tube with a linear responsivity curve. Figure 3.9 shows that in flight mode, we detect $\sim 2\%$ fewer incident photons at 40,000 counts s^{-1} than are actually incident upon the detector. At the maximum TM count rate of 62,500 counts s^{-1}, the dead time increases to $\sim 7\%$. In calibration mode, the data is recorded into a buffer in the ground service computer memory and processed asynchronously. In this mode, there is no means of determining the instantaneous state of the detector, as the read rate is often much greater than the processing rate, however the maximum countrate is significantly higher ($\sim$ 360,000 counts s^{-1} channel^{-1}) and total dead time is $< 10\%$ at countrates $<$ 200,000 counts s^{-1} channel^{-1} (Fig. 3.9). The total countrate in this mode is limited by the detector hardware itself, namely the clock rate of the MUX, whereas in flight mode it is limited by the processing speed of the ground service computer. Means for increasing the maximum count rate are discussed in Chapter 5.3.

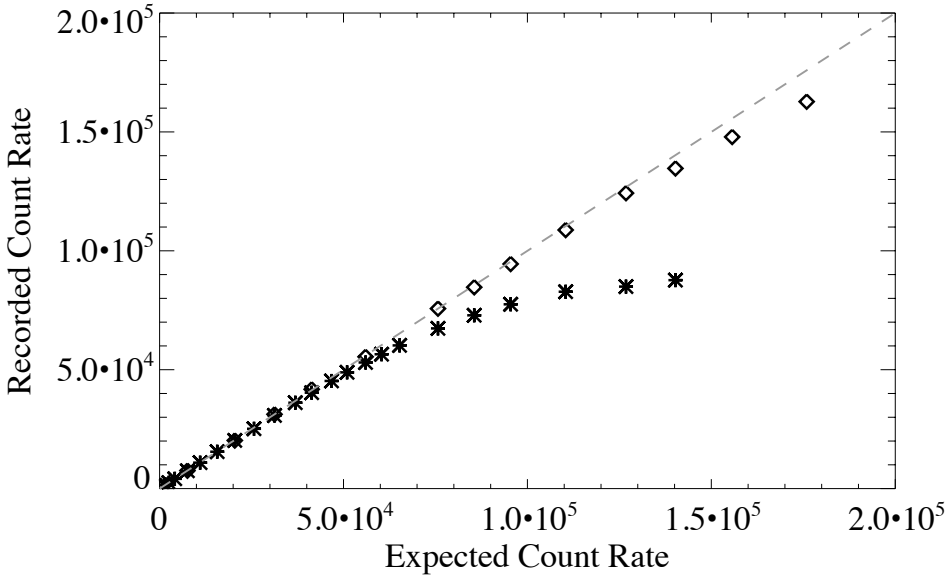

Figure 3.9: The measured response of the imaging MCP in normal operation (stars) and when the real-time display and data recording routines are deactivated (diamonds). The grey line indicates a 1-1 correlation between photons incident on the detector (modulo the detector QE (§3.3.3) for that wavelength) and the number recorded by the DAQ system

3.3.3 Detector Calibration

The quantum efficiency (QE) of a detector at a given wavelength is defined as the number of photons detected divided by the number of incident photons at that wavelength.

$$QE_\lambda = \frac{N_{d,\lambda}}{N_{I,\lambda}} \tag{3.2}$$

To measure the QE_λ for the FORTIS MCPs, the detectors were installed in the CTE on a flange attached to the end of the main chamber. In this configuration, the neck of the chamber is too narrow for the steering mirror to move the beam onto all three channels, therefore the detector flange is offset so as to center the beam on the region between the imaging and one of the spectral channels. After those two channels are calibrated, the flange is then shifted over to allow the targeting of the imaging and other spectral MCP.

The incident photon flux, $N_{I,\lambda}$, is measured directly by a NIST MgF_2 windowed Cs_2Te photodiode (SN 682-3) for wavelengths greater than 1100 Å, and a windowless Al_2O_3 photodiode (SN 239) for wavelengths less than 1216 Å. The diode current is read by a Keithley 6514 System Electrometer and the recorded value for each measurement is the median of 2000 samples. The beam intensity required to produce a signal on these photodiodes of only 2× the noise inherent to the system yields nearly half the maximum count rate on the MCPs, therefore a QE measurement calibrated directly against the diodes has large error. An EMR 542G photomultiplier tube used

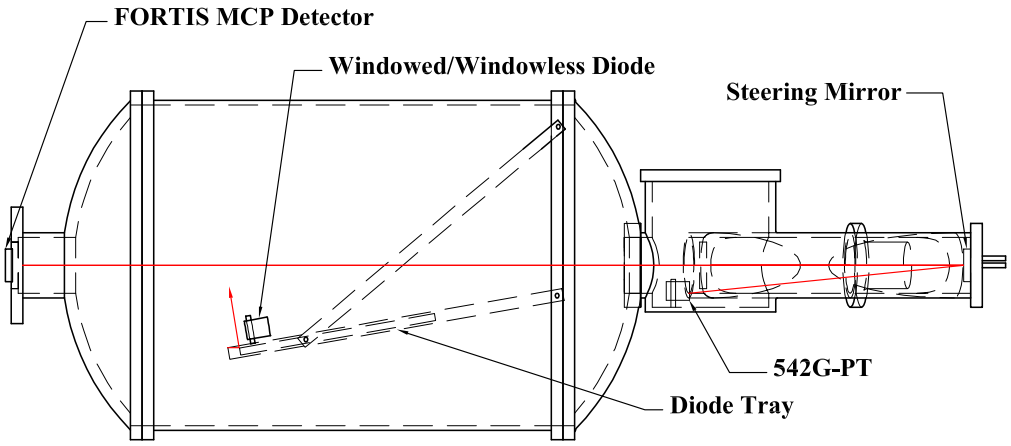

Figure 3.10: Schematic drawing of the CTE when setup for measuring the FORTIS MCP detector QE. The beam can be steered down to the 542G-PT using the steering mirror for cross calibration. The NIST calibrated photodiode (windowed or windowless, depending on the wavelengths being calibrated) can be moved into and out of the beam by raising or lowering the tray.

as a secondary standard allows for a much lower intensity light source and greater accuracy, as it has a linear response at much higher incident photon rates than the MCP, and higher gain than the photodiodes,. The PMT was calibrated against the photodiodes with a high intensity beam, and then a lower intensity beam was used to cross-calibrate the detectors against the PMT. A schematic of the setup is shown in Figure 3.10.

The original photocathode on the delivered detector had quantum efficiencies about half of previous measurements of CsI coated XDL MCPs, such as those on the *Hubble Space Telescope* - Cosmic Origins Spectrograph (COS) [80]. Those QEs were remeasured approximately 9 months later and found to have decreased by an

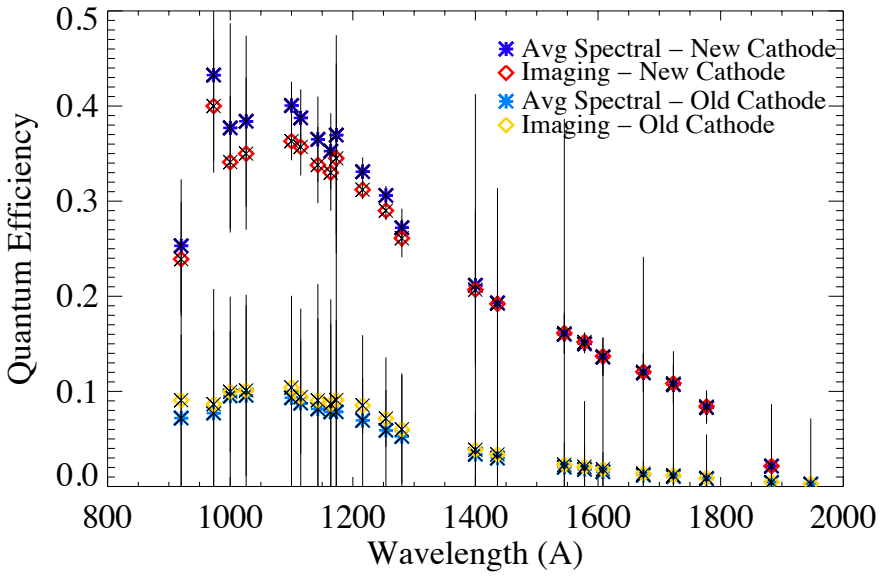

Figure 3.11: Detector QE for the imaging and averaged spectral channels before and after the deposition of a new CsI photocathode

additional ∼50% from the original measurement. The detector was sent back to the manufacturer for repairs and a new CsI photocathode was applied. Subsequent measurements of the QEs were close to the that of the COS mission requirement, peaking at ∼0.4 at 1100 Å (Fig. 3.11). Each QE was measured in three positions on the spectral channels and six on the imaging channel. The total variation in QE was $<$ 5% on all three detectors, verifying a close to flat responsivity on scales on the order of the spot size of ∼6 mm.

Primary Mirror	
Diameter	502 mm
Form	Parabola
Focal Ratio	F/2
Secondary Grating	
Diameter	165 mm
Form	Tri-axial Ellipse
Ellipsoidal x-axis (a)	698.77 mm
Ellipsoidal y-axis (b)	698.67 mm
Radius of Curvature (xz)	520.83 mm
Object Distance (Prime Focus, s)	312.5 mm
Image Distance (Imaging Detector, s_m)	1562.5 mm
Ruling Density (d^{-1})	320 lines mm^{-1}
Ruling Width (d)	31250 Å
Incidance Angle (α)	0°
Stigmatic Condition	$(a/b)^2 = (s_m + s\cos\beta_s)/(s_m + s\cos^3\beta_s)$
Output Angle (β_s)	$\pm 2.38^\circ$
Output Leg ($s_m/\cos\beta_s$)	1563.85 mm

Table 3.1: Properties of the optical elements

Detector Characteristics			
	Spectral -1	**Imaging Order**	**Spectral +1**
Size (mm)	62.5 × 42	42 × 42	62.5 × 42
# X bits	13	12	13
# Y bits	13	12	13
# Pulse Height bits	4	6	4
Active X-elements	5763	3214	6017
X Pixel Size (μm)	10.85	13.07	10.39
Active Y-elements	5566	3015	5565
Y Pixel Size (μm)	7.55	13.93	7.55
High Voltage (V)	-4100	-4200	-4150
Max Count Rate	62,500	62,500	62,500

Table 3.2: FORTIS Science Detector Properties

3.4 Instrument Effective Area

The instrument effective area, $A_{\lambda,eff}$, is defined as the effective collecting area of a telescope given the losses due to efficiencies, reflectivites, and transmissions at a given wavelength.

$$A_{\lambda,eff} = \pi(QE)_\lambda \epsilon_\lambda R_{\lambda,pm} T_{\lambda,lens}(r_o^2 - r_i^2) \tag{3.3}$$

In the case of the spectral orders, $T_{\lambda,lens}$, the transmission of the corrector lens, is unity. Using $A_{\lambda,eff}$ reduces the calculation of the incident photon flux desnity into the experiment to

$$F_\lambda = \frac{N_d}{A_{\lambda,eff}} \quad [\gamma s^{-1} cm^{-2}] \tag{3.4}$$

Where N_d is the number of counts recorded per second at a given wavelength on the science detector. The effective area of FORTIS is calculated by combining the data from Figures 3.3, 3.7, 3.11, and Table 3.1 and is presented in Figure 3.12. The peak effective area of $\sim$40 cm^2 at Lyα is in line with the design expectations and nearly double that of the *Hopkins Ultraviolet Telescope* – Astro-2 (HUT) [75].

3.5 Microshutter Array

The MSA consists of a 128 $\times$ 64 grid of individual clear aperture 100 μm $\times$ 200 μm slits located at the prime focus, each containing a 0.5 μm thick silicon nitride shutter

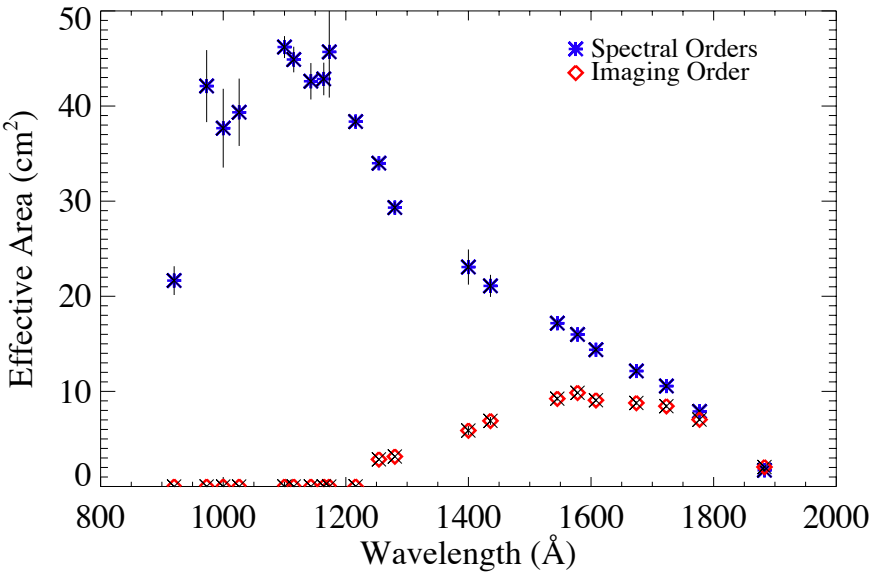

Figure 3.12: The effective area for the FORTIS spectral and imaging channels

blade affixed to a torsion bar (Fig. 3.13). Each shutter has an open area subtending 15.″9 × 36.″9, with a pitch of 20″ × 40″ and an open area ratio of Θ_{MSA}=0.73. When closed, the shutter blade is framed by a light shield which effectively blocks ∼ 99.95% of incident light. The shutters are coated with thin strips of high permeability magnetic material to allow them to be partially opened (or closed) by the close scanning (∼ 1.0 mm) of a quadrupole magnet. Electrodes are deposited on the surfaces so that magnetically actuated shutters may be electrostatically latched open by applying opposing polarity voltages to the shutter support grid. Supertex HV584 level shifters enable the individual addressing of shutters by switching the ± voltages in sync with the actuation of the shutters by the magnet. The MSA is mounted to a

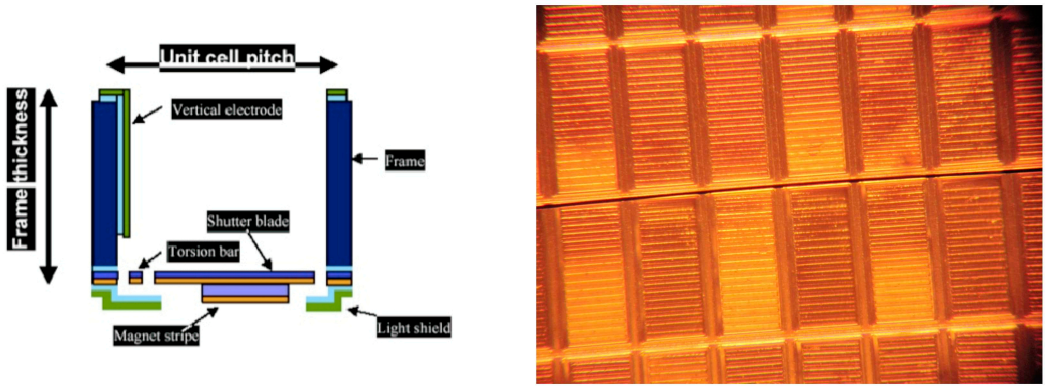

Figure 3.13: (Left) Cartoon schematic of a microshutter unit cell. (Right) Front illuminated photograph of the magnet side of the microshutter array through a microscope. Magnetic strips are visible on the surfaces of the shutters.

"D"-shaped custom circuit board (dubbed the "Big-D"), which is placed so that the MSA is coincident with the prime focus. The "D" shape allows the light reflected off the grating to pass around the assembly with minimal occultation. The MSA is controlled by a NASA developed, and JHU modified, control software on a *National Instruments* cRIO 9076 FPGA module with 2× 9403 32 ch. 7μs and 2× 9401 8 ch. 100ns C-series TTL digital I/O cards.

The quadrupole magnet assembly was designed at JHU. It provides smooth and steady motion of the magnet across the face of the MSA within a limited space and is vacuum compatible. A Faulhaber LM-0830 magnetic linear motor is affixed to the lower portion of the straight back of the "Big-D", with the magnet yolk attached to the end of the drive rod. The far end of the carrier assembly is supported by a slide mounted to the opposite end of the "D". Two optical switches serve as limit

indicators and feed directly into the MSA control software, which routes the signals to the Faulhaber motor control module. Delrin channels on either side of the magnet yolk constrain the assembly to protect the MSA. The motor is not independently controllable in its flight operation and can only be driven from one limit switch to the other by a control pulse generated by the MSA software. This limited motor control is acceptable for a sounding rocket flight as only basic commands can be uplinked to the payload during the science mission, therefore a simple and autonomous operation mode is preferred. Uplinked commands to the payload order the software to latch ("all open") or address a pattern, which in turn initiates the motion of the magnet.

The microshutters themselves are somewhat fragile and susceptible to minor manufacturing defects, damage from debris impact, and sudden power losses, which cause opened shutters to "flap" shut, occasionally dislocating the shutter. Similarly, the bonding of the array to the "Big-D" itself may result in electrically dead rows or columns. The FORTIS optical bench is designed to incorporate a slight amount of alignment adjustment so that the position of the prime focus, which subtends only 88×43 shutters of the 128×64 shutter array, is optimized to avoid large areas of failure.

3.5.1 Microshutter Testing History

The FORTIS MSAs are prototype versions of the larger JWST arrays and feature a number of design differences [74, 81]. The first array to be bonded to a Big-D,

dubbed "Big-D4" (hereafter BD4), was installed onto a mock-up of the flight mounting plate and magnet assembly and secured in a testing vacuum dewar at GSFC in June 2011. A bank of LEDs was positioned $\sim 6''$ behind the array and coaligned with a window and external camera system to enable imaging of of the LEDs through open microshutters. The initial RIO software (a Labview RT/FPGA based code developed at GSFC and later modified by JHU) was integrated with the JHU developed magnet control software, and the electrical connections to BD4 were verified.

After a period of troubleshooting, the first partially successful pattern address occurred on September 8, 2011 (Fig. 3.14a). This first address had many problems, mostly related to software and control parameter issues. BD4 was destroyed during environmental testing in October 2011 and replaced by a new array installed on Big-D2 (BD2a). The wire bonds to the silicon carrier on BD2a were ~ 200 μm taller than on BD4, while the clearance of the magnet over the array itself was only ~ 700 μm (Fig. 3.14b). Contact was made between the wire bonds and the magnet during operation and caused damage to the array, requiring a new array to be bonded to Big-D2 (BD2b) and a procedure implemented to measure bond-magnet distances and to adjust the magnet positioning. BD2b was the first array to be successfully addressed on March 18, 2012 and was designated the flight array, however it was destroyed during vibration testing in November 2012 (Chapter 4.2) and replaced with the backup array, BD1, which ultimately was the array used for the first flight.

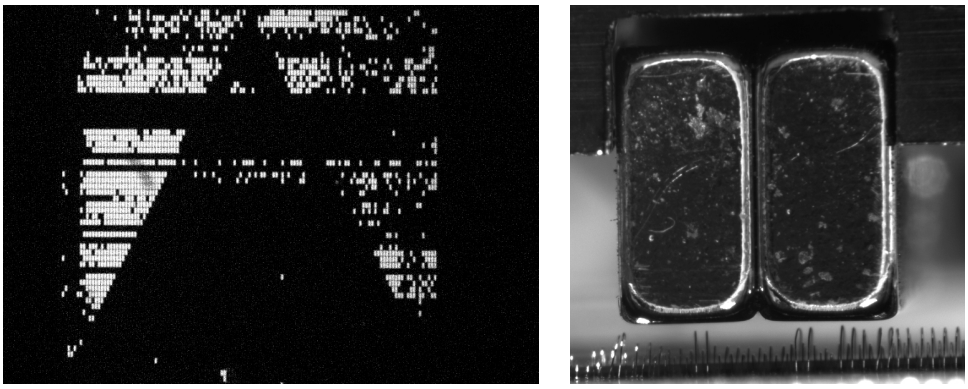

(a) (b)

Figure 3.14: (a) The first partially successful address of the FORTIS test MSA BD4 at GSFC. (b) Photograph of the magnet clearing the wirebonds on BD2b. Separation distance is ∼155 μm.

3.5.2 Microshutter Operation

The original strategy of operating the FORTIS MSA, derived from the JWST operation strategy, caused excessive static charge buildup on the shutters, resulting in a significant number of microshutters sticking open when commanded shut. The FORTIS team developed a new operation strategy in March 2012 designed to minimize charge buildup, producing nearly perfect address patterns (Fig. 3.15).

To change from "Closed" or "Addressed" to "Latched", the magnet is scanned across the array while a low-state latching voltage (V_L ∼24 V) is applied to both the vertical (column) and horizontal (row) rails. Once the array is latched, the power supply is transitioned to a high state, V_H (∼33 V), and the row voltage is dropped to 0V, resulting in a holding potential $V_L < V_H < 2V_L$, where V_H is the minimum potential necessary to hold the microshutters open against the closing force of the

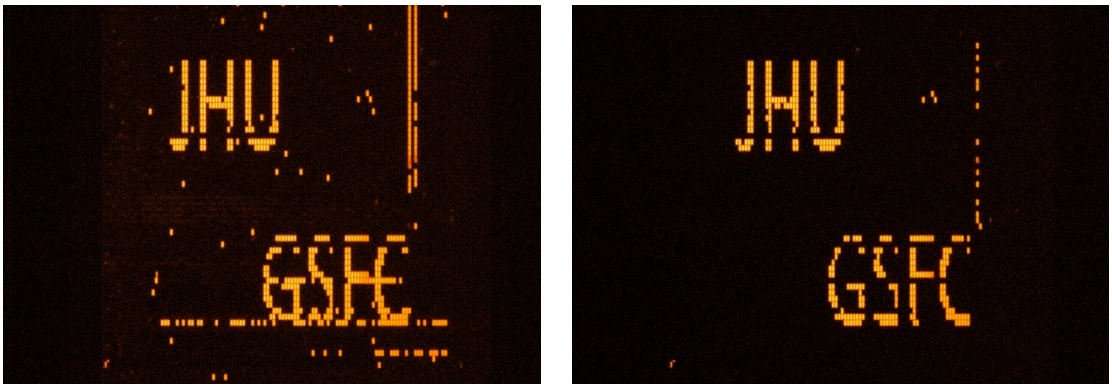

Figure 3.15: (Left) Image of addressed microshutter array using the original addressing strategy in the test setup at GSFC (Right) Image of addressed microshutter array using the new FORTIS addressing strategy, taken immediately after the image on the right. Improperly open shutters are mechanically damaged and were identified for plugging

torsion bar. To address the array, both rails are first dropped to 0V to allow some static charge to bleed off. The magnet is scanned back across the array synchronously with the cascade of $\pm V_H$ voltages that activate only a single column, and the associated row(s) selected for that column, at a time. Once the addressing sequence is complete, the power supply returns to the low state, holding the addressed pattern with $2V_L$, the minimum necessary to maintain the pattern.

At installation in December 2012, BD1 was 68.7% functional, or 2483 of the 3612 shutters in the field of view were operational and the remainder were either electrically or mechanically damaged. This was significantly worse than BD2b, which was 85% functional before being destroyed. At the time of launch, BD1 was 67.7% functional, with the $\sim 1\%$ drop being largely intermittent. There were three contrast leak shutters that were mechanically prevented from fully closing (Fig. 3.16).

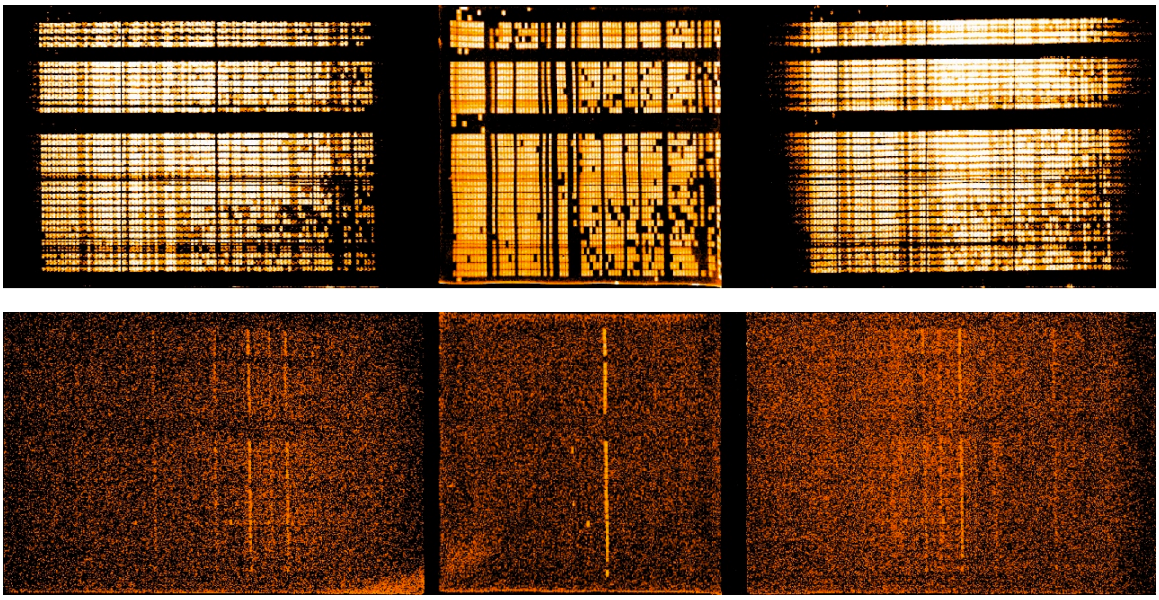

Figure 3.16: (TOP) The central imaging channel of FORTIS showing a fully latched MSA illuminated by an air-fed hollow cathode lamp, flanked by the spectral outrigger channels showing the spectrally dispersed image. (BOTTOM) Same as above, but with only a single row of the microshutter addressed open. Three contrast leak shutters can be seen in the imaging channel.

3.5.3 Microshutter Timing and Alignment

There are four variables involved in the synchronization of the microshutter; the scan speed of the magnet, the delay between when the magnet motion is initiated and the initiation of the addressing routine, the dwell time of the microshutter control software when voltages are applied to a column, and the time interval between addressing sequential columns. If the magnet scans faster than the addressing progresses, then no shutters will open, as the magnet lifting force will operate on unpowered microshutter. If the magnet scans too slowly, than it will open all the shutters, as the array will be fully charged. When the timing is off by only a little, a portion of the array may address correctly, but then the remainder will either be fully open or closed.

The magnet scan takes $\sim$3.2 seconds to traverse the 3 cm between limit switches. Testing showed that a faster scan rate decreased the success rate of MSA addressing and increased errors as the dwell time was insufficient to actuate each shutter properly. A slower scan rate resulted in an uneven and choppy motor run, also increasing addressing errors. These software controlled addressing parameters require adjusting every time the motor assembly is installed, as there are slight differences in motor performance and therefore actual magnet scan rate, and have been found to have a tolerance of 3000 μs. If the addressing begins $\sim$1500 μs or more too soon or too late, the function will fail as described above. Once the parameters are properly calibrated, the microshutter has a $> 99\%$ success rate at addressing the proper pattern, though not all functional shutters are successfully opened every time.

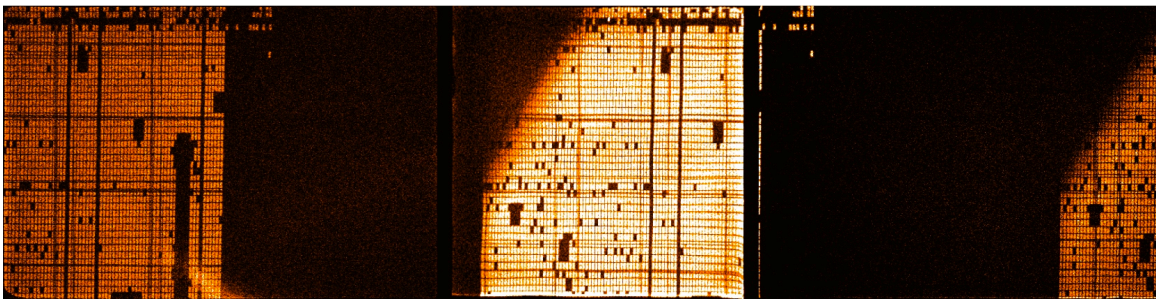

Figure 3.17: Firstlight image of an open MSA (BD2b) illuminated by a Hg pen-ray

3.6 End To End Calibrations

The fabrication of FORTIS was completed on May 18, 2012 and firstlight images were obtained the following day by illuminating the payload with a Mercury lamp through a quartz window attached to a bulkhead at the telescope aperture (Fig. 3.17). Initial end-to-end checks focused on verifying that all systems functioned, including MSA addressing, detector operation, and that the optics were coarsely focused and aligned. Subsequent tests finely adjusted the grating position to optimize focus, generated a wavelength calibration for all microshutters, and aligned the ZOMI.

3.6.1 Optical Focus and Spectral Resolution

The fine focusing and alignment of FORTIS was achieved by attaching the telescope aperture to a 400 mm F/12 vacuum collimator [82] and illuminating a 20 μm pinhole with a hollow cathode lamp fed by a $\approx$ 0.1 torr atmospheric leak. The lamp was attached to a custom 3-axis stage powered by *Physik Instrumente* precision linear

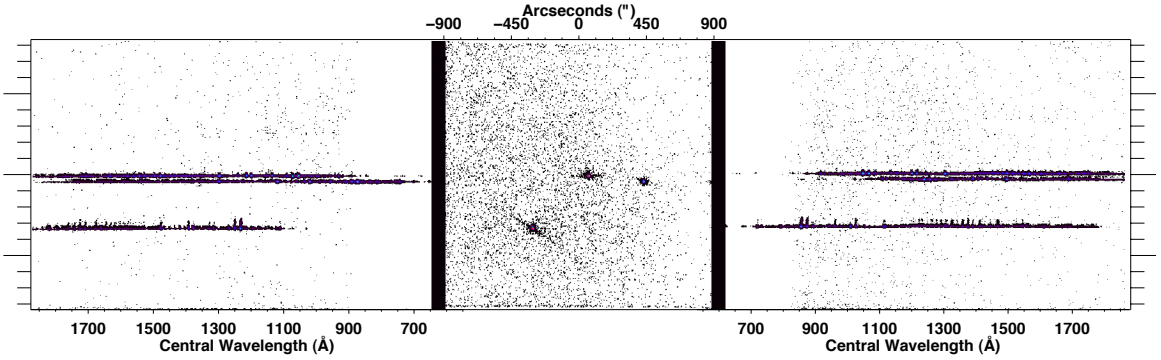

Figure 3.18: Composite image of three separate point-source calibration spectra, each taken through a single microshutter (the point source is smaller in angular scale than a full microshutter aperture) with all other microshutters closed.

actuators, which provided micron scale movement capability and enabled the beam to target any individual microshutter (Fig. 3.18). Focus sweeps were performed in the center and each corner of the imaging detector by moving the light source in 50 μm steps. Precision shim adjustments to the secondary grating mount were applied to optimize the focus.

The best focus was defined to be the spot with the lowest FWHM in the dispersion direction to maximize the spectral resolution. At the center of the imaging channel, the FWHM of the point spread function for the X and Y dimensions was 105 μm and 162 μm respectively, which for a platescale of $41\farcs25$ mm^{-1} corresponds to a spatial resolution of $4\farcs3 \times 6\farcs7$ (Fig. 3.19). While much larger than the $1''$ design goal, this resolution is still smaller than the $15\farcs9$ open width of a single microshutter.

The Ar I $\lambda\lambda$ 1048, 1066 doublet was used for measurement of the spectral resolution. Argon gas was leaked into the hollow cathode lamp to a pressure of $\sim$0.1

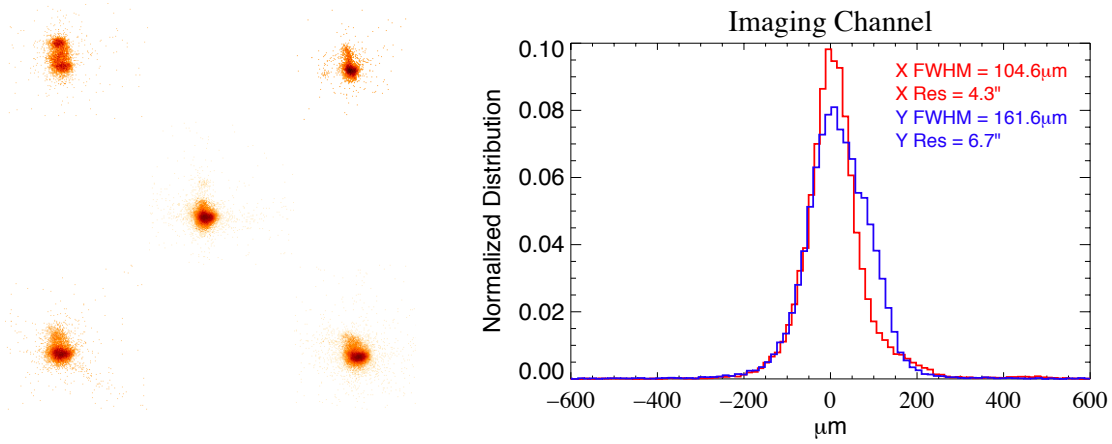

Figure 3.19: (Left) Variation of the FORTIS image across the imaging channel. Separation of spots is not to scale. (Right) Plot of the point spread with FWHM in real and angular units, given a $41\farcs25$ mm^{-1} platescale

torr. Residual atmospheric gas in the lamp provided enough signal for alignment of the beam in the imaging order, which is not sensitive to the argon lines due to the CaF_2 in the corrector lens. Both the positive and negative channel exhibit similar line profiles and spectral FWHM, averaged for the two lines, of 2.77 Å and 2.84 Å respectively for a spectrum corresponding to a spot on the center of the imaging channel (Fig. 3.19). This corresponds to a resolving power, using the average λ and FWHM, of

$$R = \frac{\lambda}{\Delta\lambda} = \frac{1057 \text{ Å}}{2.805 \text{ Å}} = 377 \tag{3.5}$$

which is below the R $\sim$ 1500 featured in the FORTIS design goals [73] and is mainly attributed to the primary mirror PSF.

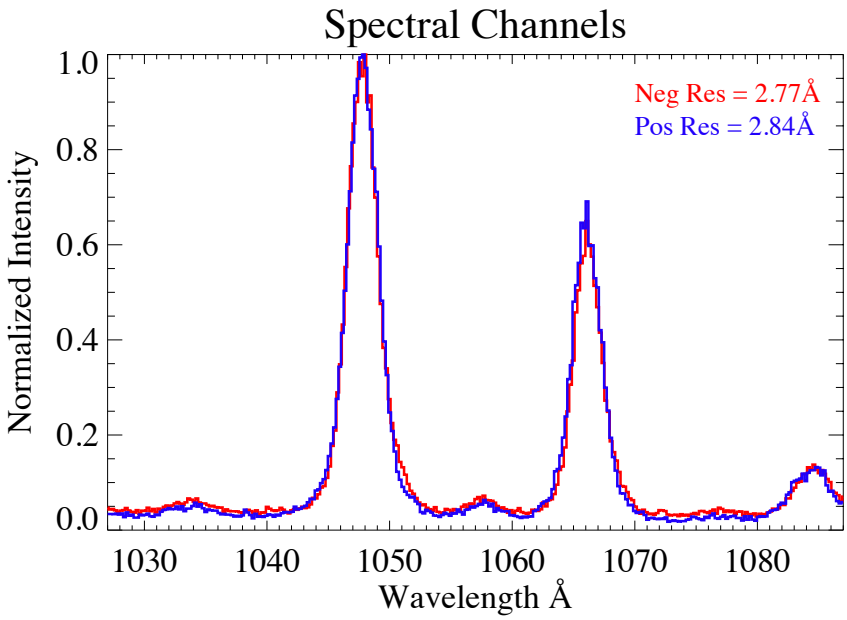

Figure 3.20: Normalized intensity of the Ar [1048] and Ar [1066] lines from both spectral channels. The average FWHM resolution using both lines is listed for each channel.

3.6.2 Wavelength Calibration

Wavelength calibration for the 2483 individual working microshutter slits progressed in two steps. A low fidelity wavelength calibration was obtained by illuminating the MSA with the hollow cathode lamp source attached to a bulkhead at the entrance aperture of the telescope. A $\leq$ 1 torr mixture of atmospheric gas was fed into the lamp, which was separated from the telescope high vacuum by a 50 μm pinhole. Payload pressure was maintained at $\leq 1{\times}10^{-5}$ despite the leak. The microshutter software mask was modified to enable only a single column of shutters to open at a time, essentially acting as a longslit spectrograph (see Fig. 3.16). Low count rates, filled slits, and a high background necessitated that this method only provide a first order wavelength calibration for 4 – 7 spectral lines, but for every functional microshutter (Fig. 3.21).

For the second step, approximately 30 high resolution spectra of the point source from the vacuum collimator sent through a single microshutter were taken with an Argon + atmospheric gas leak into the lamp of $\sim$0.2 torr. Each of these spectra consisted of 23 atomic lines and blended molecular bands of sufficient strength and isolation to be used in developing a wavecal solution, with another 17 mostly CO bands too blended to be effectively isolated. The shortest wavelength spectral line used for the wavelength calibration is O II λ 833, while the longest is the CO band at $\sim$1811 Å (Fig. 3.22).

The individual spectral lines were identified using a custom peak finding routine

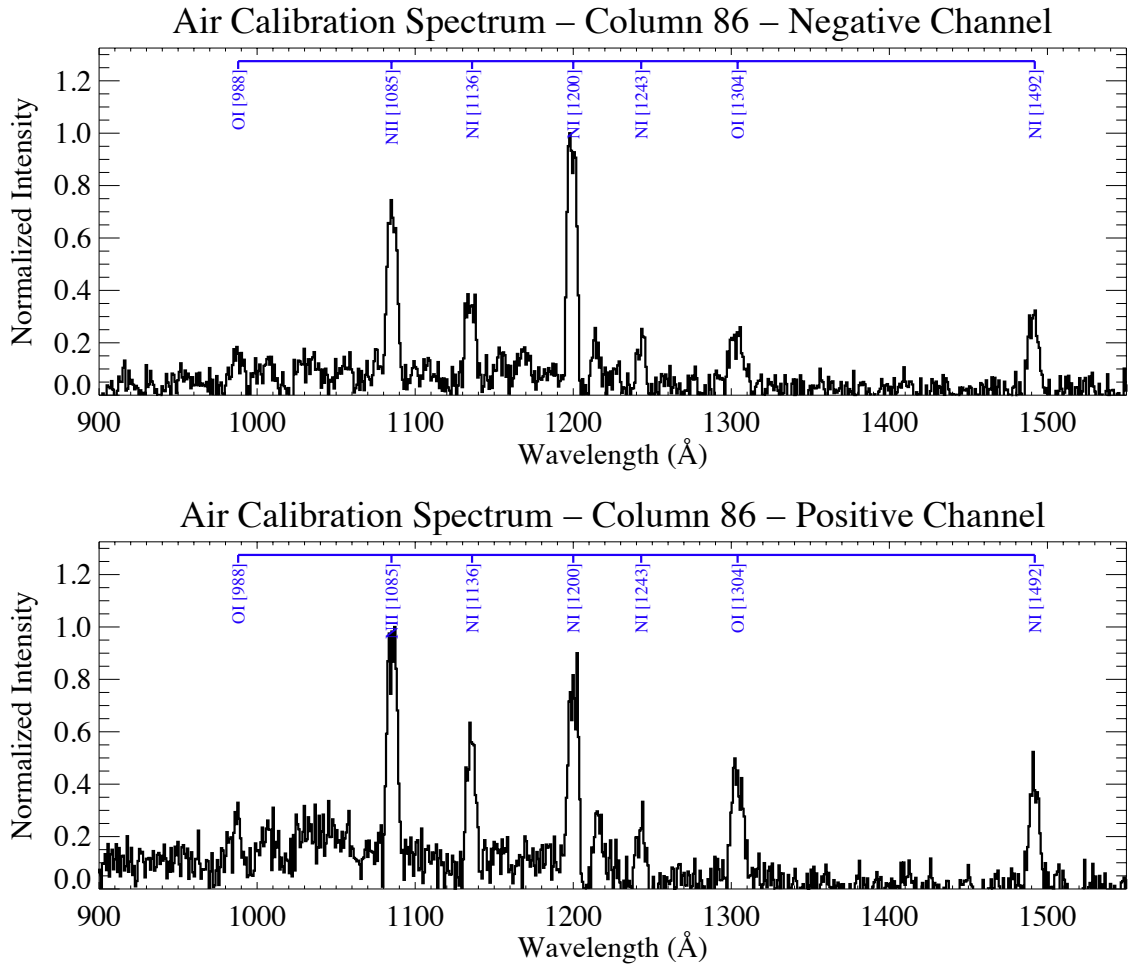

Figure 3.21: The positive and negative calibration spectra for a flat-field source through a single column of microshutters with lines identified.

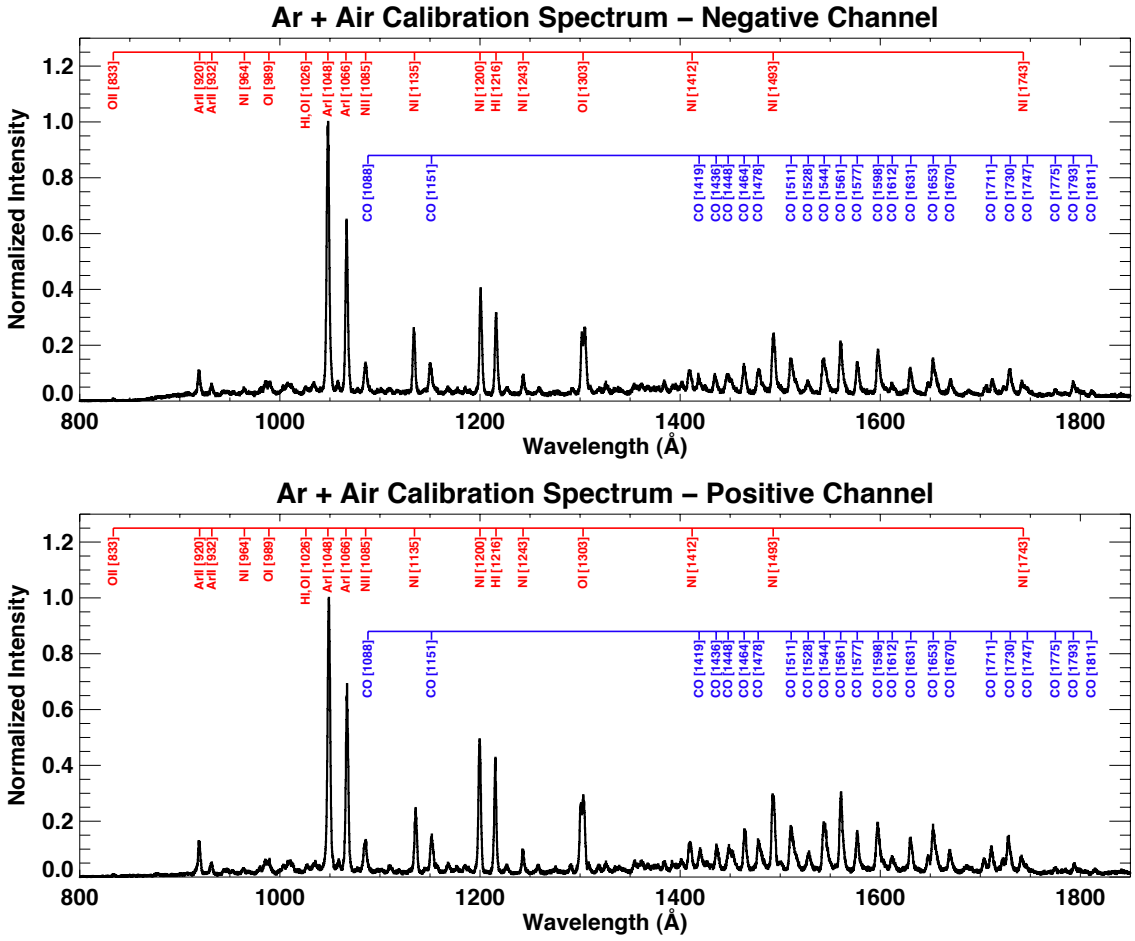

Figure 3.22: The positive and negative calibration spectra for a single point-source with lines identified.

and the centroids determined by fitting with Gaussian profiles. The wavelength solution is a 4^{th} order polynomial fit to the identified centroids and their approximate wavelengths. The centroids of the lines identified in the flat-field calibration spectrum for any given microshutter are then used to determine the necessary offsets for the nearest point-source wavelength solutions. Using this two-step method, we have successfully developed a routine that, for any imaging order pixel, can calculate a wavelength solution accurate to within $\pm$ 1.5 Å for 900 – 1700 Å for the central 90% of the field-of-view, with MCP distortion limiting the viability of this method for sources on the edge of the imaging detector. In both cases, the spectral channels were first corrected for the slight rotation in the grating, and then a second-degree, two-dimensional polynomial correction was applied using the IDL routines *Polywarp* and *Poly_2d* in order to reduce the effects of MCP distortion.

3.6.3 Zero Order Microshutter Interface (ZOMI)

Autonomous targeting is carried out by the *Zero-Order Microshutter Interface* (ZOMI). This custom JHU developed software runs as a subroutine of the onboard master microshutter control software, and interfaces directly to the MCP imaging detector. The data MUX has a separate parallel output for the most significant eight bits of the Y and X data coordinates from the zero-order MCP detector, which is fed into the cRIO as a single 16-bit data word. Each coordinate data point is degraded in resolution down to its corresponding location in an 88 $\times$ 42 grid, the

number of active shutters in the FORTIS array, and the resulting position in a memory block is incremented by 1, effectively accumulating an image of the FOV in the cRIO memory. When the appropriate command is sent via the *Command Uplink System* (CUS), a subroutine will analyze the memory block and generate a 128 × 128 bitmap (the shift registers are 128 bits long, even though the array is just 128 × 64) indicating the location of the brightest shutter in each row. When the ZOMI has completed the generation of the bitmap, the microshutter control software reads the corresponding memory location, initiates the motion of the magnet assembly, and sends the addressing bitmap to the HV584 shift registers on the "Big-D".

The 88 × 42 active area must be properly located within the 128 × 128 bitmap, therefore frequent optical alignments of the spectro-telescope need to be performed to insure that the prime focus location does not shift. To calibrate this alignment, a mask is applied to the MSA to allow only one column at a time to function (Fig. 3.16). The ZOMI is then asked to pick up on that column and open the correct column during addressing. If it opens the wrong column, then the x-alignment is shifted appropriately. Once the MSA is aligned in one dimension, all but a single row and single column are masked, allowing only one shutter to open when the array is latched, and the process is repeated for the other dimension. The MSA at the time of the first flight had a $\sim 1.2^{\circ}$ rotation relative to the detector plane, so a rotation transformation is applied to each coordinate to improve performance at the edges. Final calibration performance showed that the ZOMI is capable of selecting the proper

shutter across ∼90% of the MSA, however MCP distortion causes a 1 shutter error in the x-dimension in the lower-left and upper-right corners (Fig. 3.23).

Due to the large number of failed and intermittent shutters on the flight MSA, and the difficulty in addressing only a few shutters at a time, only ∼80% of the functional shutters selected to open during a ZOMI address successfully. For larger patterns involving more shutters, this success rate is closer to 90%. New arrays currently being fabricated by GSFC should improve that rate (Chapter 5.3). Once aligned, only a shift in the prime focus location can move the ZOMI out of alignment. During three rounds of vibration testing, this alignment was found to hold to within 0.5 shutter widths ($7\farcs5$).

3.7 Summary

FORTIS is a moderate resolution (R ≈ 377) far-ultraviolet spectroscopic telescope with a peak effective area at Lyα of ∼40 cm^2. At the conclusion of all testing prior to the first flight of FORTIS (Chapter 4), the instrument was capable of autonomously selecting the brightest regions of the 0.5° field-of-view and isolating those regions to take spectra of them. With the exception of lower spectral and spatial resolution due to the primary mirror PSF, all the design goals of FORTIS were met and the instrument calibrations are in line with the expectations. FORTIS is a powerful instrument for exploring atomic line emission in the FUV, especially to meet the

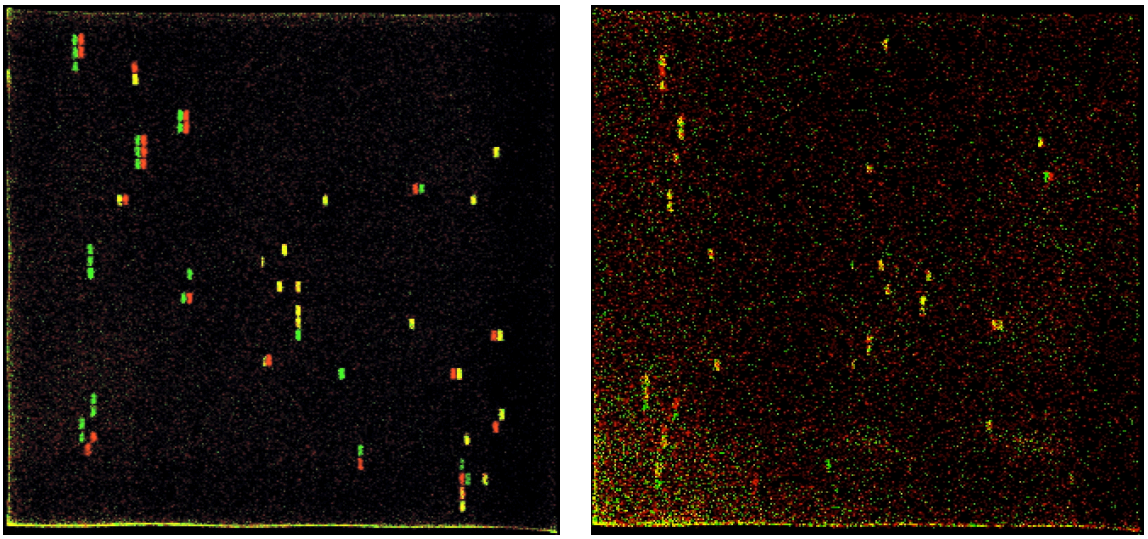

Figure 3.23: (Left) A mid-calibration image of a pattern of microshutters formed by a ZOMI address from an all open shutter array (red) and the ZOMI pattern generated when the ZOMI is ran on that same pattern (green). Misalignments are due to the effects of MSA rotation on the MCP and an inaccurate mapping of ZOMI pixels to microshutters. (Right) A more successful ZOMI pattern addressing after the parameters were set. This illumination is by an ion gauge, which has a lower countrate than the Hg pen-ray used for the image on the left. Only 3 of the 31 open shutters are incorrect, and 2 of those are in the region of high scattered light in the bottom left where the scatter is higher than the transmitted light through the open shutter for that row.

science goal of detecting Lyα escape from nearby low-redshift startforming galaxies. With measured efficiencies near the Lyman edge, and calibration spectra of lines at wavelengths as short as 833 Å FORTIS also serves as a pathfinder mission for enabling observations of Lyman Continuum (LyC) escape.

Chapter 4

JHU/NASA Mission 36.268UG

The launch of the NASA/JHU sounding rocket mission 36.268UG from the White Sands Missile Range (WSMR) occurred at 23:00 MST on May 10, 2013 powered by a Bristol Aerospace Black Brant IX with a Terrier first-stage booster. The primary science target was Messier 61 (M61), and the specific science goals are outlined in §4.1. An overview of the specific launch configuration and payload qualification is outlined in §4.2. §4.3 provides a brief summary of the launch night activities, including the partial failure of the science instrument and subsequent damage to the payload discovered during the post-flight payload recovery. The limited primary science results that could be extracted from the data are presented in §4.4.

4.1 Science Goals

This mission is the first in a program to investigate Lyα escape from nearby star-forming galaxies and to quantify its relationship to the local gas-to-dust ratio. This requires far-uv spectroscopy, which will permit simultaneous observations of both Lyα and the far-uv continuum, along with ancillary observations of optical Balmer lines acquired from ground-based observatories. Far-uv observations will be conducted using FORTIS; a multi-object spectro/telescope with a MSA designed to observe extended bright HII regions of low redshift star-forming galaxies (Chapter 3). The targets for the program have been selected to either maximize Lyα detection probability or to investigate gradients in the gas-to-dust ratio within a galaxy. The Lyα targets have redshifts sufficient to shift the emitted Lyα away from geocoronal Lyα and the Lyα absorption shadow of the Milky Way.

4.1.1 Target Selection

Potential targets were selected from the NGC catalog of galaxies. All targets with a spatial extent in any single axis of $\geq 4'$, and coordinates observable from WSMR during late spring/early summer timeframe, were ranked by suitability. Candidates were visually screened using data from the *Galaxy Evolution Explorer* (*GALEX*) survey archive to check for UV-bright knots and nearby UV-bright companions within the 0.5° FOV (Fig. 4.1). Promising candidates were fed into a simulation program

where the *GALEX* NUV (1771 – 2831 Å) and FUV (1344 – 1786 Å) images were used to estimate the slope of the fuv continuum (β) and generate synthetic FORTIS images and spectra (Fig. 4.2).

The target selected for the first launch was the star-forming galaxy Messier 61 (M61, a.k.a NGC 4303), a barred spiral galaxy in the Virgo cluster. Basic properties of M61 are listed in Table 4.1. M61 is a large ($\sim 7' \times 6'$), nearly face-on spiral galaxy with signs of new and ongoing star-formation in the spiral arms that dominate the UV luminosity [83–85]. The star-formation may have been triggered by the recent collision or interaction of gas clouds, or by interaction with companion galaxies [86]. The galacto-centric redshift of z $\sim$ 1560 km s^{-1} is low, but large enough to shift Lyα by $\sim$ 6 Å, enough to move the emission out to the edge of the geocoronal line profile for a filled microshutter. The nearby spiral companion NGC 4301 has a slightly lower galactocentric velocity, however it also features UV bright spiral arms and provides a secondary target $\sim 9.6'$ away to demonstate the abilities of the MSA and the ZOMI, and also to serve as another potential science target.

M61 is home to six supernovae in the past century, making it one of the most prolific sources of SNe in the local universe. The high SNe rate not only is evidence of the presence of massive young stars, but also increases the probability of a bubbles caused by SNe carving out pathways for Lyα and LyC photons to escape; one of the potential mechanisms. The relatively high HI fraction for galaxies of its type would make it a poor choice for a LyC search (unless there are SN bubbles), but offers a

Properties of Messier 61	
Angular Extent	$6.5' \times 5.8'$
Redshift	0.00522
Heliocentric Velocity	1566 km/s
Morphological Type	SABbc
RA (J2000)	12h 21m 54.895s
DEC (J2000)	$04^\circ\ 28'\ 25.13''$

Table 4.1: Basic properties of Messier 61. Source: NED

chance for FORTIS to test for resonant scattering as an escape mechanism and even the potential for Lyα equivalent width boosting (See Chapter 1). At the center of the galaxy is a LINER type AGN embedded in a cluster of young stars with ongoing star-formation [87]. This bright central core provides the possibility of secondary science for FORTIS as further proof of concept, if it is bright enough to be selected by the ZOMI.

The simulation of M61 indicates that it is possible for FORTIS to observe both M61 and NGC 4301 simultaneously despite a 4-shutter wide dead-zone of rows in the upper-middle of the MSA, and another 2-shutter wide set of dead rows near the top. By positioning the telescope so that M61 is slightly off-center, and including a rotation angle of -50°, NGC 4301 could be centered within an upper band of functioning microshutters. The flux estimations suggest that both galaxies should produce

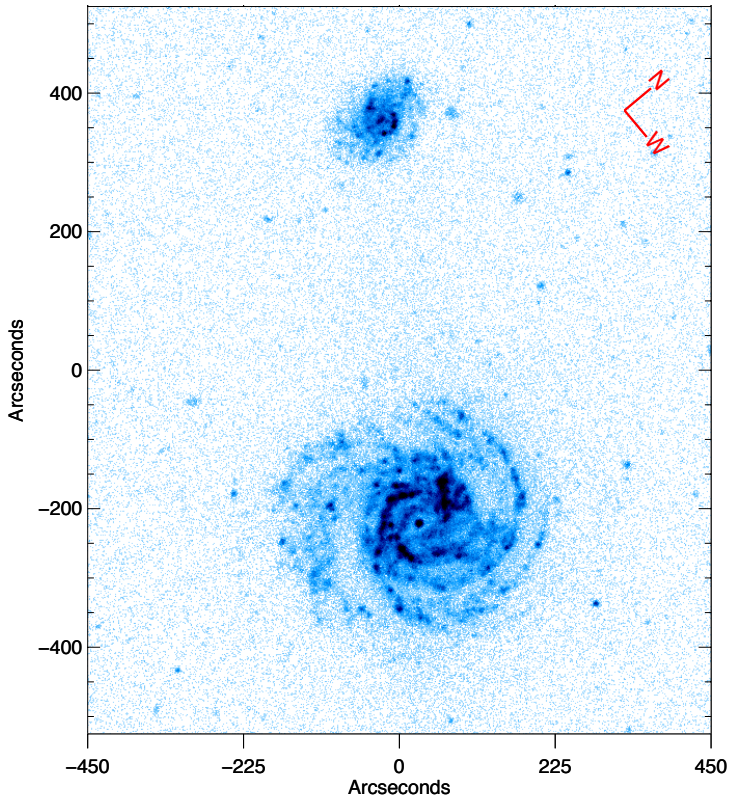

Figure 4.1: *GALEX* fuv image of M61 and nearby companion NGC 4301 at the FORTIS target roll angle

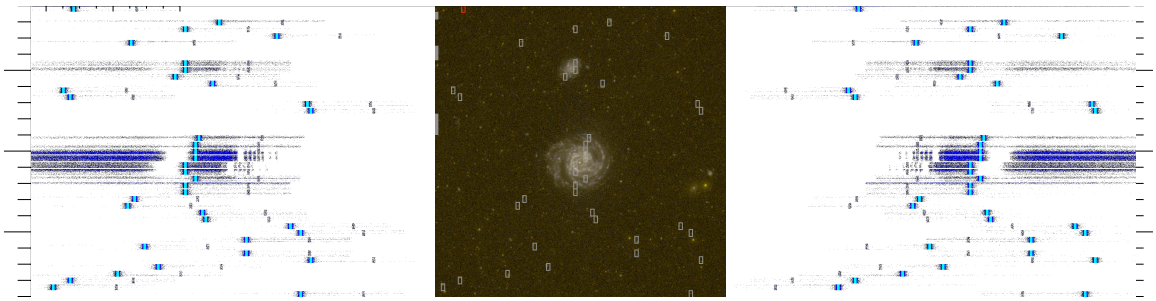

Figure 4.2: Simulated FORTIS observation of M61. Shutter overlay mask shows the anticipated ZOMI bitmap given the flux estimation derived from *GALEX*. Spectral channels include geocoronal Lyman α and β estimates.

measureable spectra within the $\sim$ 400 second timeframe of a sounding rocket mission. A single microshutter positioned on the bright inner arm $\sim$1.′5 to the north of the core would observe an estimated flux in the GALEX fuv bandpass of 2.94×10^{-14} erg cm^2 s^{-1} shutter^{-1} Å^{-1}. Equation 3.4, assuming a mean wavelength of 1500 Å, a bandpass spanning 400 Å, and a mean effective area of 10 cm^2, indicated this flux would generate a FORTIS count rate of $\sim$ 8.87 counts s^{-1} shutter^{-1} in the imaging order; far higher than the FORTIS background of 0.003 counts s^{-1} shutter^{-1}. The lower surface brightness outer arms feature an average flux of 2–5 $\times$ 10^{-15} erg cm^2 s^{-1} shutter^{-1} Å^{-1}, corresponding to count rates $\sim$ 0.6–1.5 count s^{-1} shutter^{-1}.

4.1.2 Apache Point 3.5m Observations of M61

M61 and nearby companion NGC 4301 were observed with the *Dual Imaging Spectrograph* on the 3.5m telescope at *Apache Point Observatory* during the second half nights on April 15th and 16th, 2013 (See Chapter 2.3 for a description of the instrument and data pipeline). The goal of the observation program was to determine the Balmer line ratio Hα/Hβ as a measure of the extinction, and to compare to the measured Lyα flux using Case B recombination theory. For both nights, the level of 1 μm dust particles was near the operational safety limit of the telescope, and winds were gusting at near 30 mph, all resulting in seeing that was never better than 2″. The high winds and poor seeing also affected the telescope tracking, resulting in erratic pointing. The second night was interrupted by intermittent clouds.

4.1.2.1 Observation and Reduction Strategy

Due to the large angular area of M61, a drift sequence was used in order to observe the bright central arms of the galaxy in the two half-nights allotted. The telescope was set to drift 13.″5 perpendicular to the slit per exposure, and then to reset to the original position. Three redundant 450 second exposures were taken for each drift sequence, with ∼60 seconds of overhead per exposure, covering $13.''5 \times 6'$ every 25.5 minutes. The target was not observable the entire half night due to low altitude, therefore all M61 observations occurred within $\sim$ 7 hours and covered $2.'2 \times 6'$. To avoid gaps in the coverage field, as the telescope tracking was uneven due to poor seeing conditions, step sizes of only 12.″5 were taken between drift sets. The outer spiral arms are unlikely to be selected by the FORTIS ZOMI for observation, therefore the goal of the program was to cover only the inner $3'$ of bright star-forming regions, with the rotation angle such that the slit would be oriented along the MSA columns in the FORTIS FOV (Fig. 4.3). A summary of the observations is given in Table 4.2.

Due to the limited observation time, no dither sequence was implemented to observe empty sky for airglow subtraction. Instead, the standard star Feige 67 was visited three times over the course of each night, and the airglow observed in each of those visits was used to estimate the airglow inherent to the galaxy observations. There were small off-target portions on the M61 exposures near the edge of the slits that were used to aid the subtraction. This airglow strategy performed poorly and the resulting spectra are heavily contaminated by airglow lines for wavelengths >

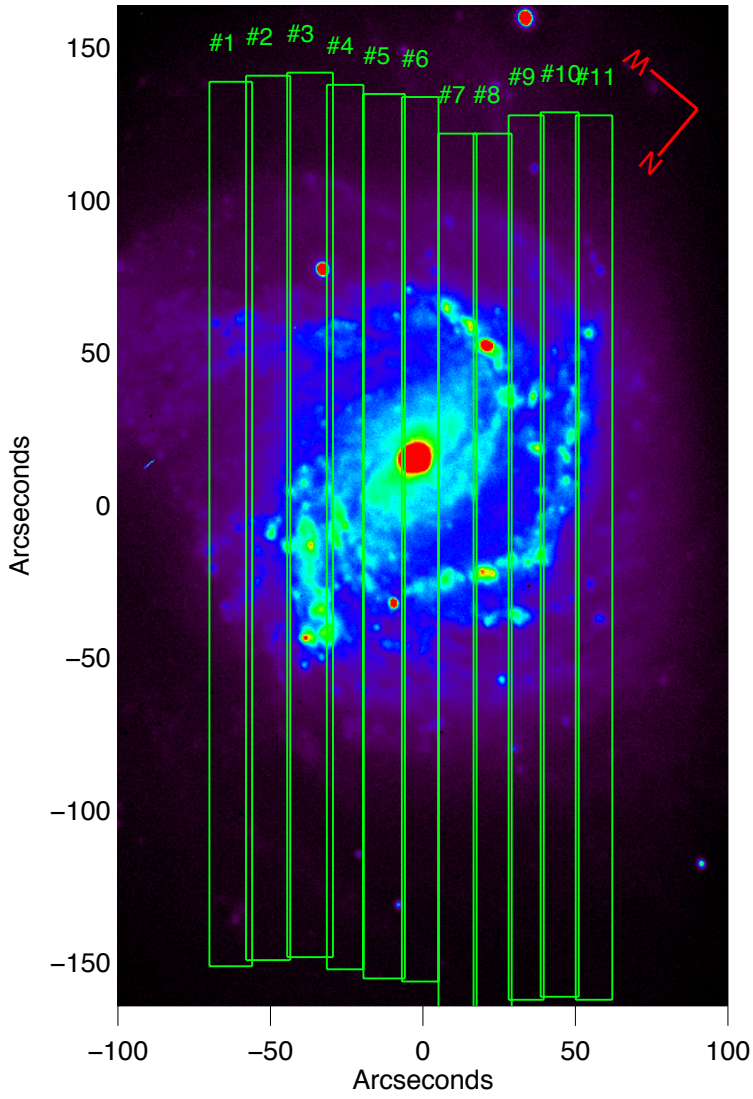

Figure 4.3: Estimated coverage area for each set of three drift exposures on the inner arms of M61. Image is a grating-less exposure taken in the blue channel of DIS. The slit-lengths are shortened from 6′ to reflect the useable area of the CCD in the spectral channels.

APO 3.5m DIS Observations	
Observation Dates	April 15-16, 2013
No. of Scan Regions	11
Redundant Exposures per Region	3×2 channels
Exposure Time	450 s
Scan Rate	$13.5''$ exposure^{-1}
Rotation Angle	$140°$
Starting RA (J2000)	12h 21m 52.97s
Starting Dec (J2000)	$04°\ 29'\ 36.01''$
Ending RA (J2000)	12h 21m 58.58s
Ending Dec (J2000)	$04°\ 27'\ 55.11''$
Flux Calibration Star	Feige 67

Table 4.2: DIS Observation Information

8000 Å, however the majority of the residual background airglow continuum has been removed, and only the Hγ line coincides with airglow line emission. Each set of three exposures for a given drift region were median filtered to produce a single 2-D spectra for each region (Fig. 4.4).

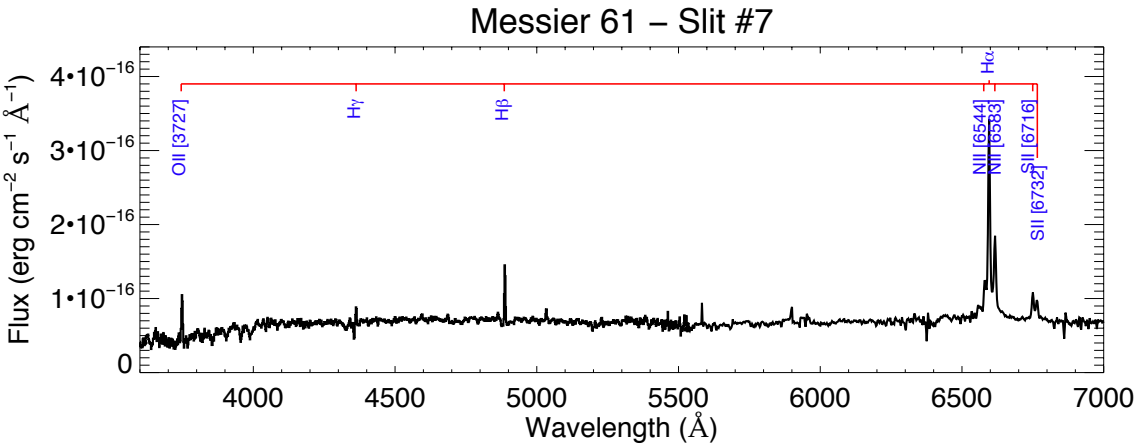

Figure 4.4: APO/DIS spectra from the seventh drift region in the observation program, covering a few bright star-forming regions.

4.1.2.2 Balmer Ratios

The guider camera images for a given drift set were used to determine the maximum displacement of the slits in the drift dimension, and the average position of the center of the slit. Due to the poor seeing conditions, the scatter in both dimensions was on the order of $4''$, therefore, a spectral map would be inaccurate. Instead, the data was divided into synthetic apertures of (drift width $\sim 13''$) $\times$ $19\overset{'}{.}3$, and the 1-dimensional spectra within were summed. This produced an 11 $\times$ 12 coarse data-cube of M61 that could be easily referenced with respect to a microshutter grid overlay with a pitch of $20'' \times 40''$.

The Hα flux for each synthetic aperture was calculated by integrating the measured flux between the [N II] $\lambda\lambda$ 6544,6583 doublet, minus the average continuum emission from either side. The Hβ flux was measured by integrating about the line after subtraction of the continuum, however the synthetic apertures often overlapped regions of emission and absorption, which may have led to an underestimation of the Hβ flux for specific star formation regions. Both the Hα and Hβ equivalent widths were increased by 2 Å to correct for stellar atmospheres [56], boosting the Hα and Hβ fluxes by an average of $\sim 1.8\%$ and $\sim$13% respectively. This is considered a first-order analysis only, to be used as a guide for the FORTIS observations. The Hα/Hβ values for each synthetic aperture are overlaid on the M61 image in Figure 4.5.

The average Balmer ratio for the entire observed galaxy, calculated by summing the entire observation into a single spectra, is 4.86 $\pm$ 0.24, whereas the Balmer ratio

for just the Hα and Hβ contained within the high signal-to-noise (SNR ≥ 5) synthetic apertures is totaled is 4.85 ± 0.24. The second method of summing all apertures where both Hα and Hβ are above the SNR threshold slightly undermeasures the Hα, as $\sim$ 0.2% of the Hα flux is not contained in the high SNR apertures, but it is a better comparison of just the bright star-forming regions.

4.2 Launch Readiness

In preparation for launch, FORTIS was subjected to a number of environmental tests to evaluate launch readiness. These tests were carried out at NASA *Wallops Island Flight Facility* (WFF). Independent electrical tests for the detector electronics and vibration testing of the MSA and telescope tower were carried out prior to full instrument integration. This section briefly describes the results of integration and testing at WFF, and then again at WSMR prior to launch. The evaluations carried out are listed in Table 4.3.

The first environmental tests involved the vibration of component parts at WFF. During the thrust axis vibration of the telescope section, with a dummy mirror and no MSA, the MSA mounting plate became loose. It was concluded that the presence of the MSA and magnet assembly would strengthen this assembly, and therefore no redesign would be needed. The MSA was housed in a special box for vibration in it's flight configuration with the magnet system installed. Plexiglass windows on the top

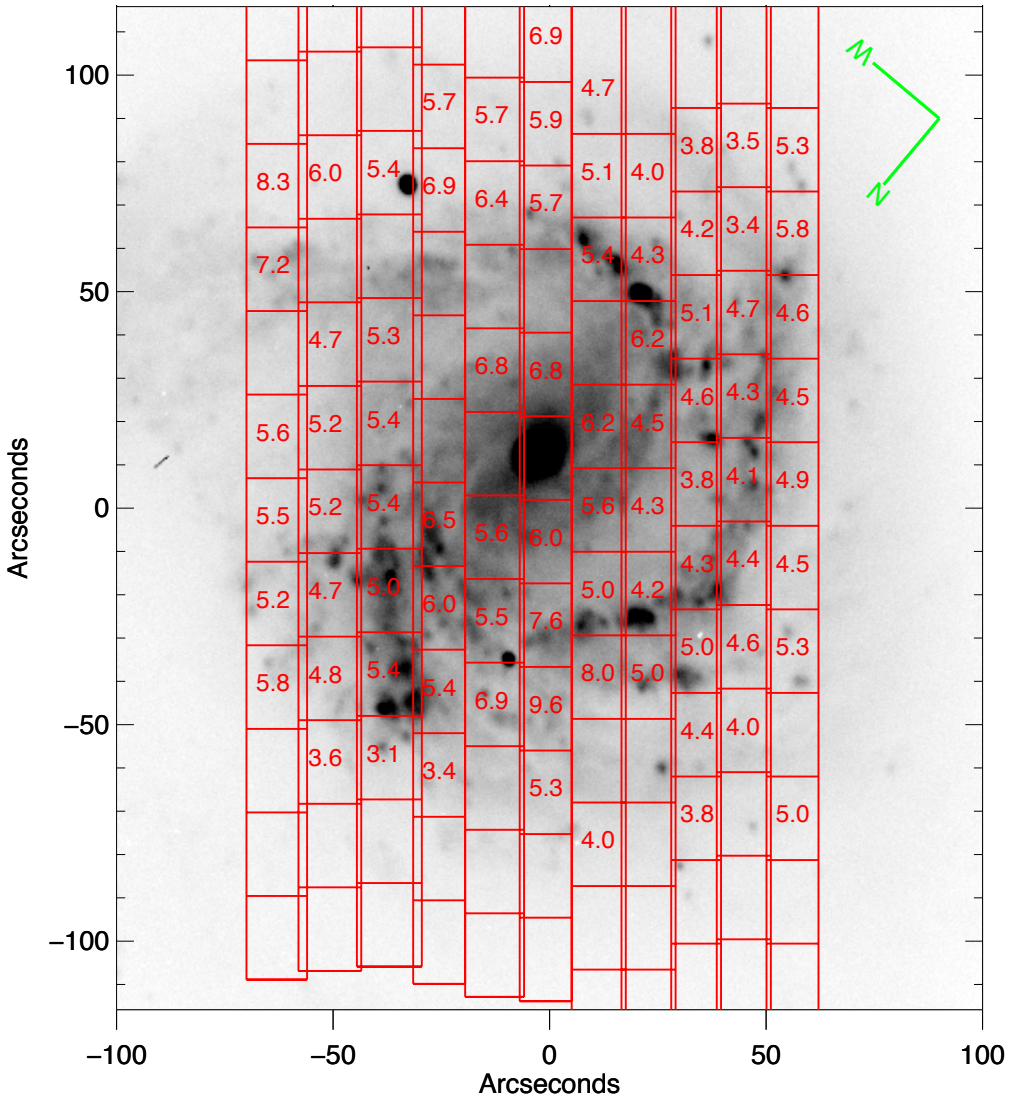

Figure 4.5: An overlay of the synthetic apertures, and the Balmer ratio Hα/Hβ contained within each one, on M61.

and sides of the box allowed viewing during testing. Resonance from the lid window caused pressure waves within the box, however, which damaged the MSA. The MSA was re-tested with this top cover off and showed no new damage.

Electrical handshaking of the detector system and telemetry required no major changes. Full payload integration in August of 2012 also led to no major changes, as all systems communicated successfully. During vibration testing, however, the detector system began to behave as if the operating HV was too high. Resulting examination revealed a loose screw within the detector itself that was shorting the anode to chassis, effectively increasing the HV applied by 600V. The detector was returned to the manufacturer for repair, and an insulator was added on top of the screws.

A second vibration test occurred after the repair of the detector. During a thrust axis sequence, the detector housing vacuum seal broke, bringing the housing up to atmospheric pressure. A pump-out port was found to be inadequately supported. A new support was built on-site and the system repaired for a third test. During the third test, the endcap of the magnet drive rod broke loose of the drive rod itself, leaving the magnet unsupported. The vibrations caused the magnet to impact the MSA repeatedly, destroying the array. A new array was installed and the magnet system redesigned to have a sturdier endcap that was pinned to the drive rod, and safety rails were added to constrain the magnet yolk. The fourth vibration test had no issues.

Environmental Testing Timeline

Date	Location	Test	Pass/Fail	Notes
August 2011	WFF	MSA Vibe	Fail	Pressure Damage
August 2011	WFF	Telescope Vibe	Pass	
Oct 2011	WFF	MSA Vibe	Pass	Window Removed
Dec 2011	WFF	MCP Handshake	Pass	Communication with TM
August 2012	WFF	Integration	Pass	Full Sequence
August 2012	WFF	Full Vibe	Fail	Detector Short
April 2013	WFF	Bend and MOI	Pass	Measurements
Oct 2012	WFF	Full Vibe	Fail	Pressure Loss
November 2012	WFF	Full Vibe	Fail	MSA Magnet Loss
January 2013	WFF	Full Vibe	Pass	Final WFF Test
April 2013	WSMR	Air Sequence	Pass	Not under Vacuum
April 2013	WSMR	Bend and MOI	Pass	Flight Measurements
April 2013	WSMR	Vac Sequence	Pass	Under vacuum
May 2013	WSMR	Horizontal	Pass	Full Launch Sim
May 2013	WSMR	Vertical	Pass	Full Launch Sim

Table 4.3: A list of environmental tests

4.3 Mission Summary

The team traveled to WSMR on April 21, 2013. The payload was integrated with the telemetry (TM), attitude control system (ACS), recovery system (ORSA), and other flight modules. Full sequence tests were carried out with the telescope section both at atmospheric pressure and under vacuum. During sequence tests, the flight timeline is executed (with the exception of altitude protected systems) on telemetry timers as things would run during flight. The flight timeline, only as is relevant to the experiment, is listed in Table 4.4. Final measurements of the bending moments and moments of inertia of the payload were conducted, and the integrated payload was assembled for launch on May 3rd, 2013. Connection to the motors on the launcher proceeded on May 5th. Final range testing, where the telemetry transmits data to the ground station from the launch rail, occurred on May 7th and 9th, with the launcher in the horizontal and vertical position respectively.

The launch of NASA/JHU 36.268UG went off on schedule at 23:00 MST on May 10, 2013. At 85.5 seconds into the flight, the MSA was addressed with a two-shutter wide slit. Once the ACS settled on target (position 1), all three MCP detectors were turned on. The imaging channel recorded at $\sim$11,000 counts per second, with the counts occurring primarily on the sides. The two spectral channels showed no apparent features and recorded at nearly the maximum countrate due to scattered geocoronal Lyα, with the bits that differentiate between X and Y coordinates being mis-allocated within the electronics (Fig. 4.6). The MSA was latched open and

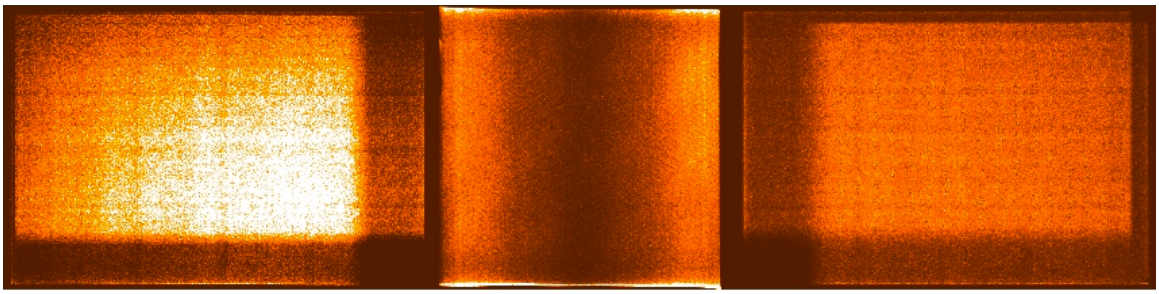

Figure 4.6: The raw flight data for the negative, imaging and positive channels. The spectral channels exhibit signs of the control bit, which identifies X and Y coordinates, being misallocated.

addressed again multiple times and no changes were apparent in the detector count rates. During this time, the spectral channels were set to the inactive standby voltage whenever the MSA was latched open. With 120 seconds remaining before the end of science operations, the payload was sent a $+3'$ pitch maneuver, and the MSA latched open and all detectors turned on, to validate any detected objects in post-flight analysis of the data (position 2).

4.3.1 Payload Recovery

The payload landed on parachute approximately 80 km uprange of the launch site. Recovery operations began at 06:00 on the morning of May 11. Upon arrival at the landing site, the payload shutter door, which isolates the vacuum telescope section, was found to have been shattered on touchdown. The catastrophic break in the vacuum caused an implosion of the telescope section, with an estimated 200 pounds of earth being sucked into the telescope. The impact drove the ACS startracker

camera into the secondary grating, ejecting the grating from its mount. The MSA was destroyed by high velocity gypsum. The post-flight analysis has led to the conclusion that the telescope carbon-fiber tower can never be repaired, therefore an entirely new telescope metering tower, MSA and magnet system, and startracker mount must be built before FORTIS can fly again. The cause of the shutter door failure is currently under investigation.

4.4 Science Data Analysis

The maximum count-rate for each detector, as defined by the telemetry parallel sample rate, was set to 62,500 counts s^{-1} per science channel, while the spectral channels recorded an average of ∼57,500 counts s^{-1} in flight. This rate is consistent with saturation, as saturation of the telemetry stream results in a large number of dropped counts. The imaging channel recorded between 11,800 counts s^{-1} and 14,100 counts s^{-1} over the course of the flight, as the corrector lens blocked the majority of the scattered Lyα, and the scatter profile reached a minimum at the center of the imaging channel due to shadowing by the baffling structure. Using the comparison of the pulse height distribution in the spectral channels taken during laboratory measurements for different count rates to those obtained during flight, we were able to estimate the peak countrate per pixel of the spectral microchannel plates to be between 1.4 – 3.6 counts s^{-1} $pixel^{-1}$ with an average of between 0.3 – 0.77 counts s^{-1} $pixel^{-1}$ (Fig. 4.7).

Assigning this average rate to the average pixel in the flight data and summing the entire detector, we estimate that the spectral channels were each recording an incident flux of between 7.1 – 18.7 Mcounts s^{-1} with a best estimate of ∼7.3 Mcounts s^{-1}. Measurements of the CaF_2/MgF_2 cylindrical corrector lens show ∼0.5% transmission at Lyα in the center, decreasing to 0.4% at the edges. We assume that the entire scattered light profile of the imaging detector is due to geocoronal Lyα transmitting through the achromat, and estimate an imaging countrate of 2.2 Mcounts s^{-1}.

The estimated total number of counts in the spectral channels recorded by the GSE computer exceeded that recorded by the ground station by 345,750, likely due to elements of the data matrix being rejected during reconstruction due to signal noise. This has proven for future missions that even at very high count rates, the GSE computer is capable of recording the entirety of the flight data, whereas on previous JHU payloads, only partial snapshots at lower countrates could be recorded by the GSE computer and displayed in real-time.

4.4.1 Spectral Data

The primary goal of activating the spectral channels for the last 120 seconds of flight was to obtain an image of diffracted geocoronal Lyα through the open MSA. An image of Lyα would verify not only microshutter operation, but also that the grating retained it's alignment and did not rotate during launch. During the flight there was no means of verifying any information in the spectral channels as the control bit,

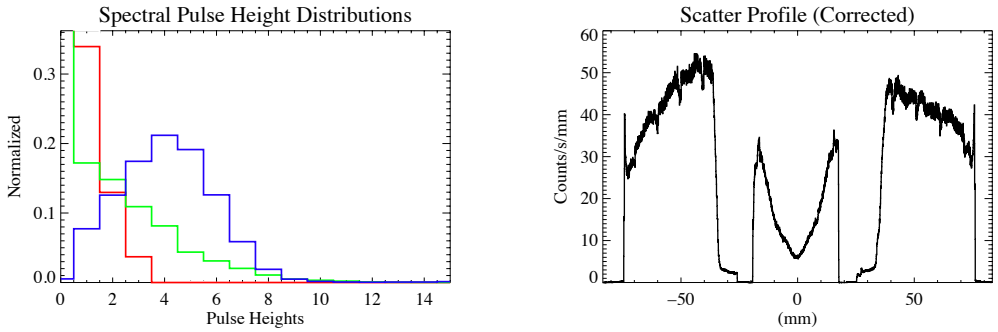

Figure 4.7: (Left) Pulse height distributions (PHD) for the negative spectral channel during the flight of 36.268 (Green), a nominal laboratory measurement of UV light at low count rates (Blue), and a laboratory measurement of a point source at 1.42 counts second^{-1} pixel^{-1}. (Right) Scatter profile across all three of the FORTIS detectors (negative-imaging-positive) during the flight of 36.268 in units of counts second^{-1} mm^{-1} in order to normalize the channels, which have different numbers of pixels. Each channel is 42mm in height.

which indicates whether each word is an X or Y coordinate, was being misassigned. This "bitflipping" resulted in a shift in the data stream, with the spectral data first being displayed in the proper orientation, and then after a bitflip appearing to be rotated 90° (Fig. 4.6). Subsequent analysis of the post-flight data products provided by the WSMR ground station verify that this bitflipping was not caused by the data GSE, but originated either in the data MUX or detector hardware.

This bitflipping occurred once before during integration testing with the telemetry section when the detectors were overwhelmed by an Hg pen-ray. To remedy that data, the moment the flip occurred was found in the time-tagged data, and all subsequent data was then reordered so that each X-coordinate was relabeled a Y-coordinate, and then paired with the Y-coordinate from the next count. This completely remedied

the data display at the cost of only two transitional counts where the bitflip occurred and there were no valid pairs. During this test, the control bit flipped only once.

An IDL program was developed to analyze the flight data in batches of 25 counts per iteration (there were a total of 11.7 Mcounts in each of the two spectral channels) and total the number of counts in two regions; one where statistics dictate that there should be < 1 count when the bits are properly aligned, but $\sim$4 counts when the control bit is flipped, and another region where there should be $\sim$3.3 counts when the control bit is proper and $<$1 when it is not. If the block of counts contained more than 3 counts in the first region and less than 1 in the second region, then it was assumed that the control bit has flipped and the coordinates are reordered starting at the 10th count in that block of 25. When the control bit flipped back to the original allocation, the same conditions would be met and the program would revert to the native ordering. The resulting image retained a residual level of misplaced counts, however summing the total counts in the forbidden region and extrapolating based on what proportion of the total area that represents, $\geq$96.2% of the total spectral counts are in their proper orientation (Fig. 4.8). The bitflip occurred an estimated 10,743 times in the negative channel and 26,505 times in the positive channel in 202.6 seconds of spectral channel integration.

The previously calculated geocoronal Lyα radiance through a completely open MSA (§3.3.1), when multiplied by the QE of the detector at Lyα (0.34) and by the ratio of functional microshutters on BD1 (0.677), predicts that each detector

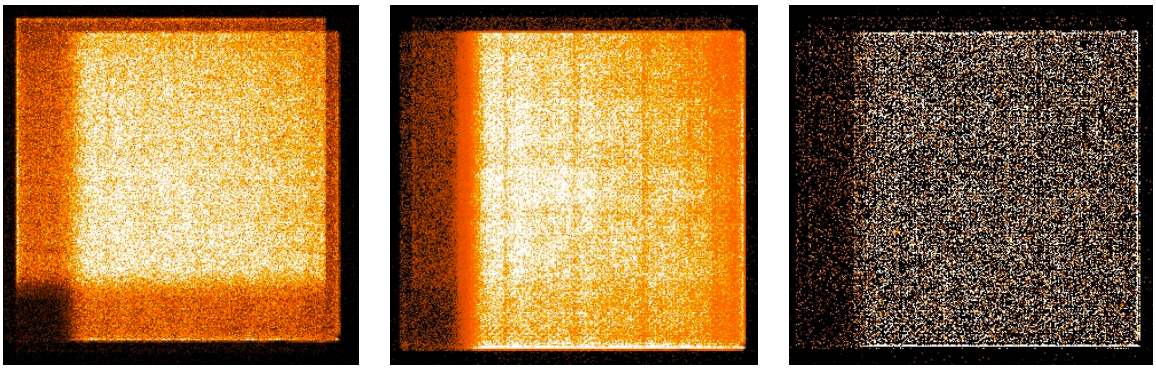

Figure 4.8: (Left) The raw data from the positive order spectral channel. (Center) The corrected positive order. (Right) Positive order data from when the MSA was latched with the data from when the MSA was addressed subtracted

should detect 4.1×10^5 photons s^{-1}, roughly 5.7% of the estimated scattered light radiance. Through the two-shutter wide slit, this number falls to ∼9,400, or 0.13%. Therefore when the array is latched open, ∼317,500 of the 5.6 Mcounts recorded by each channel over that integration should be geocoronal Lyα transmitting through the shutters, and the rest scattered light. To remove the background, the time-averaged data from when the MSA was addressed was subtracted from the time averaged data from when the MSA was open. If the Lyα transmitting through the open MSA is detectable, then this should produce the open MSA pattern with a two-shutter wide column missing, which would verify both latching and addressing. Unfortunately, no such pattern emerges, and no other analysis was able to prove if the MSA successfully addressed (Fig. 4.8).

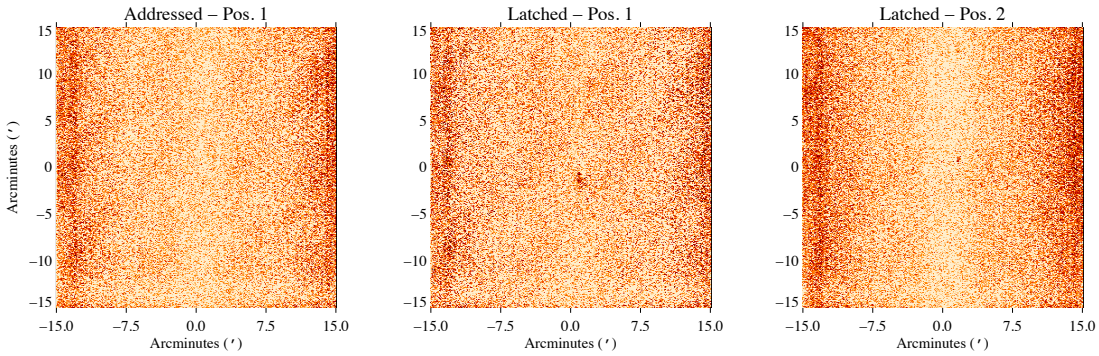

Figure 4.9: (Left) Time-averaged and background subtracted imaging channel MCP data for when the microshutter is addressed with a two shutter-wide slit (Center) When the microshutter is latched open at the original pointing of the telescope (Right) When the microshutter is latched open after a 3' pitch change.

4.4.2 Imaging Data

The imaging channel did successfully observe the target M61 through the latched microshutters despite the scattered light interference. The imaging data was parsed into three subgroups as determined by the pointing of the payload and the state of the MSA; addressed at Pos.1, latched at Pos.1, and latched at Pos.2. While the array was addressed at Pos.1 with the two shutter-wide slit, there was no detection of an overdensity of signal, however when the array was latched at Pos.1, a region $\sim 50''$ $\times$ $80''$ was observed. After the pitch maneuver of $3'$, this region mostly disappeared, however a small spot $\sim 15''$ $\times$ $20''$ was observed $\sim 2'$ higher on the detector than at Pos.1 (Fig. 4.9). There were three separate instances where the microshutter was latched at position 1 of 48, 31 and 27 seconds respectively, and in all three the overdensity is present. There was only one pointing at Pos. 2.

The inner central arms of M61 are ∼3' in diameter and would cover approximately a 6 × 4 microshutter footprint. Our estimated positioning of M61 on the MSA (Fig. 4.10) shows that more than half of the inner arms are located within a block of microshutter columns in which 3 out of 4 are not functional. The UV-bright core of the galaxy is also not visible. The portion of the inner arms observed corresponds to a star-forming region approximately $50'' \times 80''$ on the northern side of M61. The expected incident flux for this region, calculated from *GALEX* imaging and applying the MSA open area ratio of 73.3%, is 6.99×10^{-14} erg s^{-1} cm^{-2} Å^{-1}. The flux detected by FORTIS over the same angular extent at Pos.1 is $4.95\pm1.8\times10^{-14}$ erg s^{-1} cm^{-2} Å^{-1}. The discrepancy is potentially due to uncertainty in the pointing, as bright knots could be located between shutters. A surface brightness cut of 2.95×10^{-18} erg s^{-1} cm^{-2} pixel^{-1} was applied to the *GALEX* fuv image, which is consistent with the background limit for the FORTIS flight imposed by background subtraction of the scattered Lyα.

At Pos.2, the countrate is 1.28 counts s^{-1} arcminute^{-1} at the brightest shutter, however $3'$ south of that location is a damaged shutter that does not open. There is a smaller feature at Pos 1 with an almost identical 1.27 counts s^{-1} arcminute^{-1} offset ∼$20''$ to the right that is likely a different portion of the same feature (Fig. 4.10). Therefore, the portion of M61 seen at Pos.2 is not detected at Pos.1 for comparison. The companion NGC 4301 is not detected at any time due to its positioning within the non-functional MSA columns.

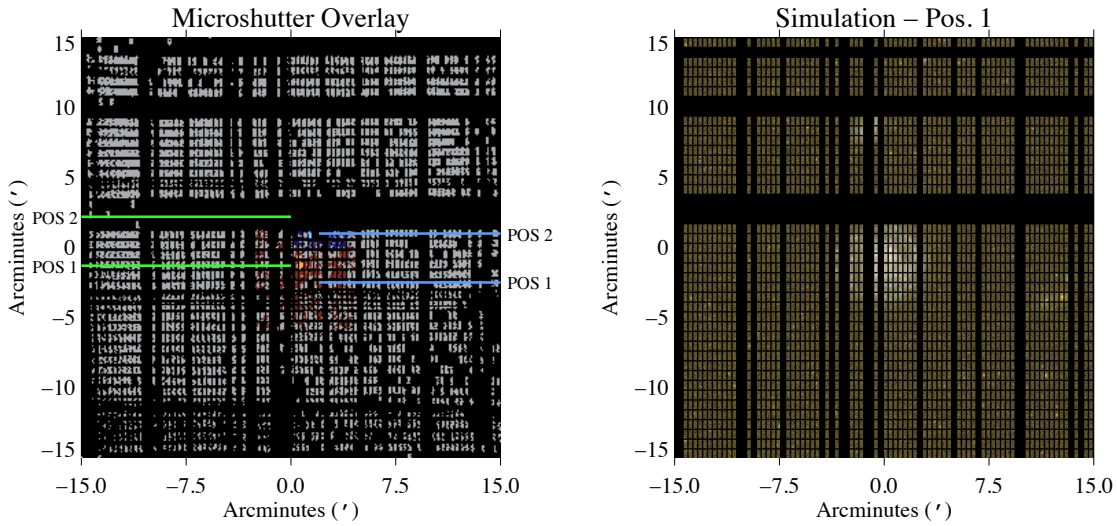

Figure 4.10: (Left) Overlay of a latched microshutter array with a flat-field illumination with the regions of interest from position 1 (Red) and position 2 (Blue) from the flight data overlaid. The Green horizontal lines indicate where the brightest region observed would have moved to at position 2, whereas the blue lines indicate where the brightest region at position 2 would have been at position 1 (Right) Simulated data using *GALEX* data to estimate where M61 was located at position 1.

The targeting guidelines set forth prior to launch called for M61 to be positioned approximately $2'$ to the right and $3'$ south of the center of the FORTIS FOV. If the observed part of M61 at Pos.1 is the star-forming region we have identified it to be, then the payload was offset from the optimum targeting position by $\sim 140'' \times 40''$, or $2.43'$. This is within the specified tolerance for the NSROC II Attitude Control System of less than $3'$, however the initial placement of the target relative to the MSA was unfortunate.

Time	**Event**	**Altitude**
T- 205 s	Exercise Detectors and MSA	0 km
T- 170 s	Switch to Internal Power	0 km
T- 160 s	Exercise Detectors and MSA	0 km
T+ 0 s	Liftoff	0 km
T+ 6.2 s	Terrier Burnout	3.2 km
T+ 12 s	Black Brant Ignition	6.3 km
T+ 46.2 s	Black Brant Burnout	47.7 km
T+ 83.5 s	Detector Gate Valve Open	117 km
T+102.0 s	Imaging Detector HV ON	135 km
T+105.0 s	MSA Latched Open	137 km
T+108.0 s	ZOMI Begin Exposure	140 km
T+135.0 s	ZOMI End Exposure - Address MSA	165 km
T+138.0 s	Spectral Detectors HV ON	167 km
T+272.3 s	Apogee	287.5 km
T+468.7 s	Detectors HV OFF	102 km
T+470.7 s	Gate Valve, Shutter Dorr Close	100 km
T+629.7 s	Parachute Deploy	5 km

Table 4.4: Experiment Flight Countdown

4.4.3 Comparison to APO Data

The region imaged by FORTIS coincides approximately with slits 1-4 on Figure 4.3. Due to the high background, it is not possible to determine the actual shutter locations on the galaxy. Had the ZOMI been run for the expected 30 seconds, this region would likely have subtended 2-3 rows of microshutters and would have been bright enough to overcome the non-scattered light background inherant to the detectors (0.003 counts s^{-1} $shutter^{-1}$). The average Balmer ratio for this region is 5.34 $\pm$ 0.25, higher than the galactic average. This corresponds to a total reddening E(B-V) = 0.60 $\pm$ 0.05 and a hydrogen column of $N_H \sim 3.5 \pm 0.24 \times 10^{21}$ cm^{-2} [40, 88]. On the surface, this high extinction and N_H suggest that there would be little possibility of LyC escape, and all Lyα would undergo countless resonant scatterings before escaping. Taking the total flux of all the Hα and Hβ in the first four APO slits masks variations in the Balmer ratio at smaller scales, however, with individual synthetic apertures in Figure 4.3 having reddening as low as E(B-V) $\sim$ 0.35, and likely even less at smaller scales.

For FORTIS to detect 100 Lyα photons during the 400 seconds of observation, the incident Lyα flux, using equation 3.4, would have to be $\geq 1.0 \times 10^{-13}$ erg cm^{-2} s^{-1}. The sum of the extinction corrected Hα flux across the synthetic apertures with listed Hα/Hβ ratios in slits 1-4 in figure 4.5 is 5.59×10^{-12} erg cm^{-2} s^{-1}, indicating that the minimum Lyα escape fraction necessary to have been detected by FORTIS with 100 counts, given an intrinsic Lyα/H_α ratio of 8.7, is 0.21%. This assumes 100

counts in the total area observed by FORTIS. The brightest synthetic aperture in slits 1-4 has an Hα flux of 6.91×10^{-13}, requiring an escape fraction of 1.66% for 100 counts in the angular area subtended by half a microshutter. The reddening is less in the star-forming regions that were not observed by FORTIS (Fig. 4.5), however similar detected Hα fluxes implies that the intrinsic Lyman and Balmer emission is also lower.

The estimated geocoronal Lyα countrate through the spatial length of 1/4 of a microshutter ($9''$) at a 3 kRayleigh brightness is 32.5 counts s^{-1}. By convolving a filled microshutter profile with the measured line-spread function of FORTIS and a voigt profile, the expected profile of geocoronal Lyα through the open slit can be caluculated. Using the highest extinction corrected synthetic aperture Hα flux from the region of M61 observed by FORTIS, and focusing that emission into a $5''$ wide spot offset from the center of the slit in the dispersion dimension by $4''$, we can model the expected Lyα line profile for various escape fractions (Fig. 4.11). We conclude that had the scattered geocoronal background not been present, FORTIS should have been able to detect an $f_{\mathrm{Ly}\alpha}$ of $\geq$5% from such a region. An improvement of the spectral resolution and imaging PSF would greatly increase this sensitivity.

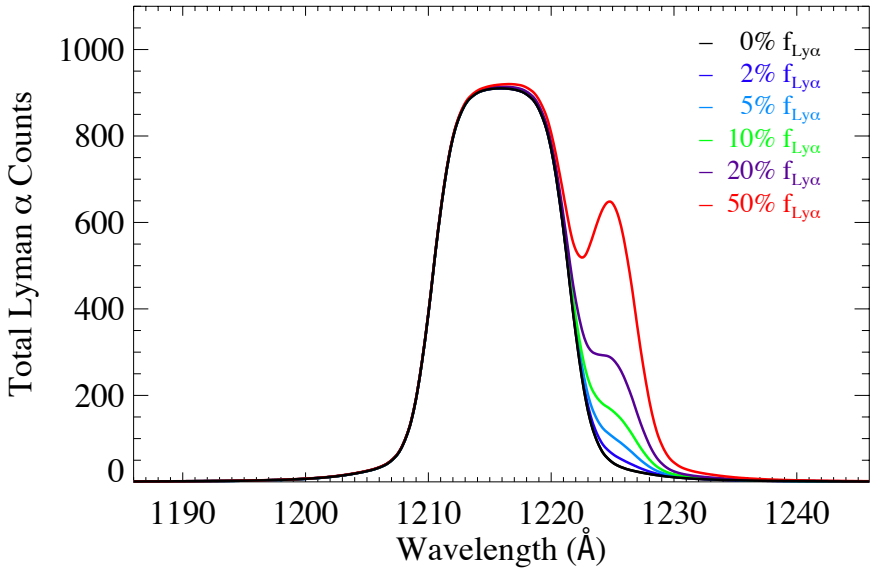

Figure 4.11: 3 kRayleighs of geocoronal Lyα emission through 1/4 of a microshutter with added Lyα escape fractions for the highest extinction corrected Hα flux measured in the region observed by FORTIS for a $5'' \times 9''$ emission region centered $4''$ off-center in a microshutter. The assumed redshift for M61 is 1550 km s^{-1}.

Chapter 5

Conclusions and Future Work

This thesis presented two separate projects with the same goal - to search for the escape of Lyα photons from nearby star-forming galaxies. The first project combined *HST* photometry and *APO* spectral mapping to measure the spatial variation of Lyα, and the escape fraction, $f_{Ly\alpha}$, in a set of 11 z = 0.02 – 0.045 galaxies. We showed that even though some galaxies do not show any net excess flux at 1216 Å relative to the expected continuum level, that there are individual sightlines into the galaxy with high $f_{Ly\alpha}$. The emission characteristics of Lyα appear to scale with the fuv surface luminosity, and inversely with metalicity, but they are not determining factors. While the galaxies in our sample all appear to trend towards bluer (m_{1416} - m_{1610}) fuv color with higher Lyα surface luminosity, when only cells showing Lyα emission are considered the colors of 9 of our 11 galaxies shift towards the red. This indicates that the Lyα flux is often, but not always, being emitted co-spatially with

regions that are redder than the galaxy as a whole.

The goal of the second project was to measure Lyα escape using the sounding rocket-borne multi-object imaging spectrograph FORTIS. This thesis showed that the capabilities of FORTIS should have achieved this goal during a recent mission, however the intensity of the background scattered light was too great.

5.1 Future Directions in $f_{Ly\alpha}$ and f_{esc}

While the science accomplishments of this thesis were directed towards quantifying the nature of $f_{Ly\alpha}$, the penultimate goal of this research is to better understand the relationship to f_{esc}. There have been a number of studies in the literature of LyC and Lyα escape, sometimes even on the same target, but not with the spatial resolution and quantity of supporting data that we have available from our *HST*/ACS-SBC + *APO*-DIS dataset. Our new measure, $f_{Ly\alpha,w}$, represents the optically brightest region that also has an appreciable $f_{Ly\alpha}$. We plan to investigate writing an *HST* proposal to target these regions with COS aperture in the new CENWAVE=800 Å mode [89]. These selected targets span a wide range of environments, from bright star-forming knots to diffuse continuum regions. If the mechanisms that govern $f_{Ly\alpha}$ and f_{esc} are similar, then we expect to see a similar f_{esc} from the bright star-forming regions as we do $f_{Ly\alpha}$. If the Lyα emission from the diffuse gas is due to resonant scattering processes, however, then we would expect no coincident LyC radiation from regions

not centered on star-formation.

There have been recent studies showing that outflows may play a dominant role in the enabling of high $f_{Ly\alpha}$ from bright star-forming regions [48]. We lacked the resolution to measure the gas kinematics from our sources for this study, but it is possible that the Lyα emitting star-forming regions show evidence of outflows, while those that have a net continuum deficit do not. It is a natural progression of this work to investigate the kinematics of our sample in greater detail.

5.2 FORTIS v2.0

Shortly after the nearly complete destruction of the telescope section of FORTIS in the New Mexico desert, the JHU sounding rocket program was awarded the chance to observe the target of opportunity comet ISON in November, 2013. The instrument is being reconstructed at a frenzied pace in order to meet an October 15th shipping deadline for travel to WSMR. Degradation of the detector and grating relative to before the flight of 36.268 has combined to lower the quantum throughput of FORTIS by a factor of 2/3, however the anticipated 150 kRayleighs of Lyα brightness of the comet would still overwhelm our existing data collection system. Therefore, in addition to re-fabricating the payload, we have also designed a filtering circuit to screen repeated words from the data stream, which should enable a higher count rate on the data GSE.

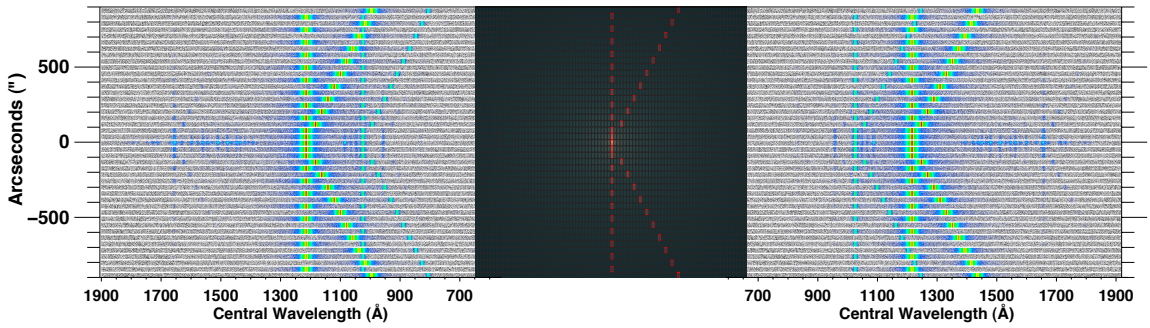

Figure 5.1: A simulated observation of Comet ISON by FORTIS with a "k"-shaped slit configuration

The brightest shutter per row ZOMI algorithm has also been rewritten to instead only find the brightest shutter, which should be the center of the comet, and overlay a "K"-shaped configuration of slits to measure the profile of the comet emission in 2-dimensions (Fig. 5.1).

This deviation from the design science of FORTIS is not permanent, however, and provided that scattered light problem has been solved and FORTIS survives the comet launch, the JHU rocket team should be back to searching for Lyα escape again shortly.

5.3 The Instrument of the Future

Great progress can be made in characterizing the escape properties of LyC and Lyα with current instrumentation, however it appears increasingly likely that large statistics will be necessary to fully understand the escape mechanisms, and to relate

the observations of the local universe back to the epoch of reionization. Despite the power of *HST*, the 2.″5 diameter aperture of COS, and the limited effective area ($\sim$ 10 cm^2) at the Lyman limit, make a project to map a significant number of nearby galaxies in the FUV infeasible. An orbital version of FORTIS, featuring the same 0.5° field-of-view, but with a larger *JWST* MSA that would enable observations on a smaller scale, would be ideally suited to carry out simultaneous observations of LyC and Lyα with only a limited survey mission timeline of 1-3 months. The targeting algorithm could be changed to find all galaxies within a FOV and to map them completely, providing comprehensive spectroscopic coverage of hundreds of galaxies with multiple sightlines. Such a mission would be invaluable for the understanding of Lyα and LyC escape, and the greater FUV research community.

Appendix A

Spectral Maps

This appendix contains all of the ACS-b images, spectral lines and diagnostic maps, and Lyα escape maps for each target.

A.1 ACS-b Images

Each of these images represents the difference between the ACS F125LP and ACS F140LP images.

A.2 Spectral Line and Diagnostic Maps

In this section are the spectral line and diagnostic maps for each galaxy in the sample.

N01 features an anomaly one the second night of observation that results in spikes

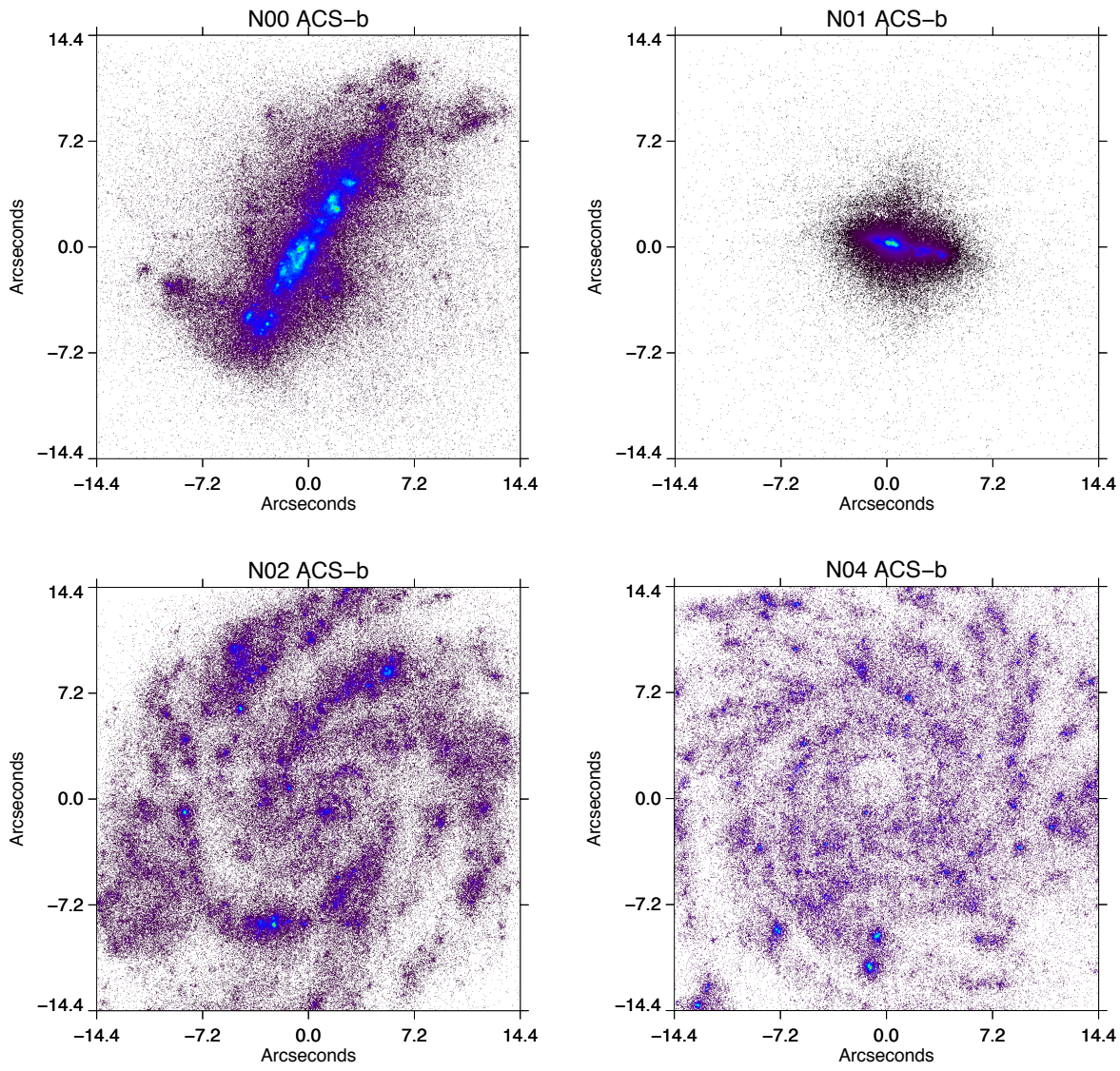

Figure A.1: ACS-b images for N00, N01, N02 and N04.

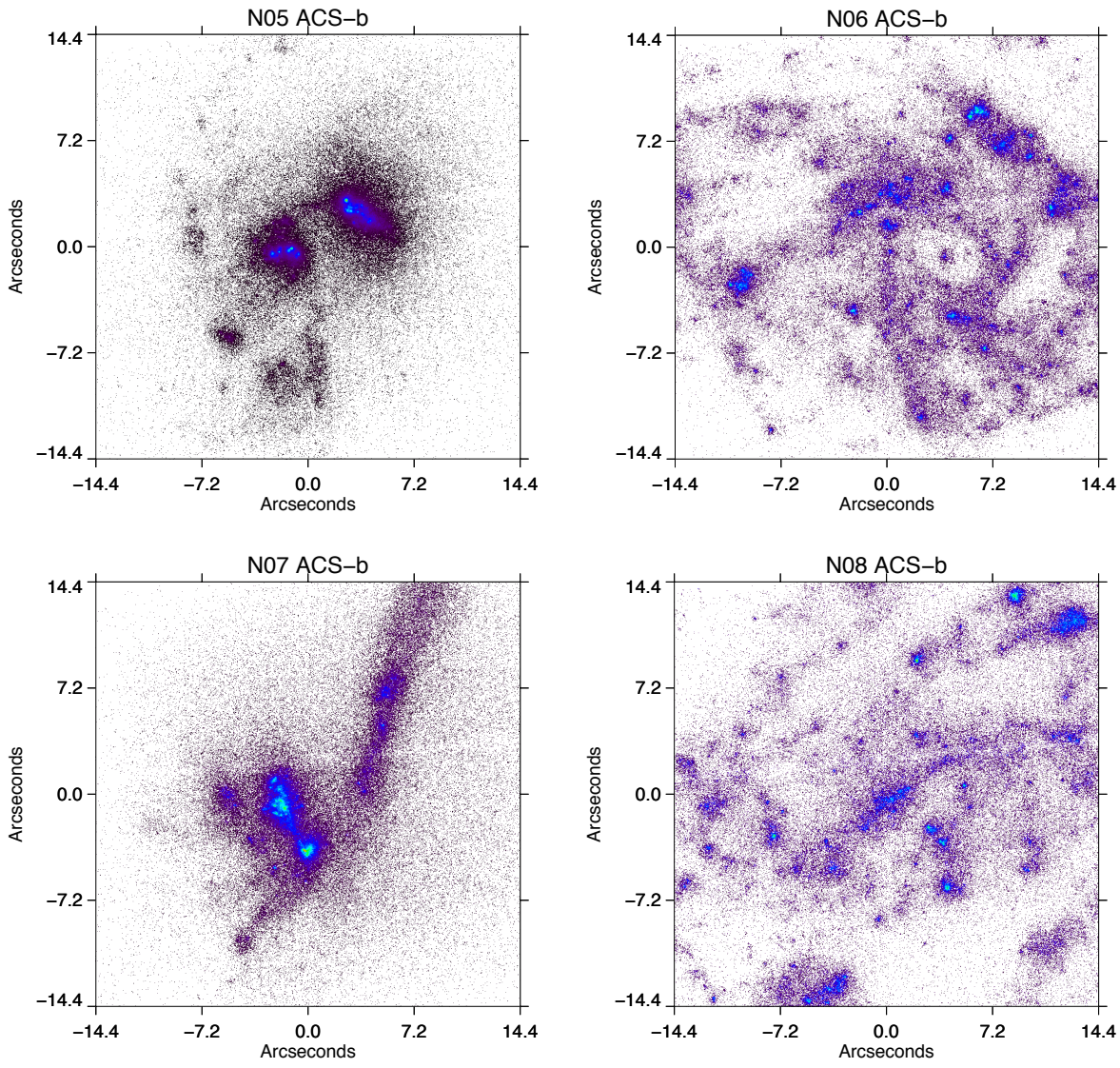

Figure A.2: ACS-b images for N05, N06, N07 and N08.

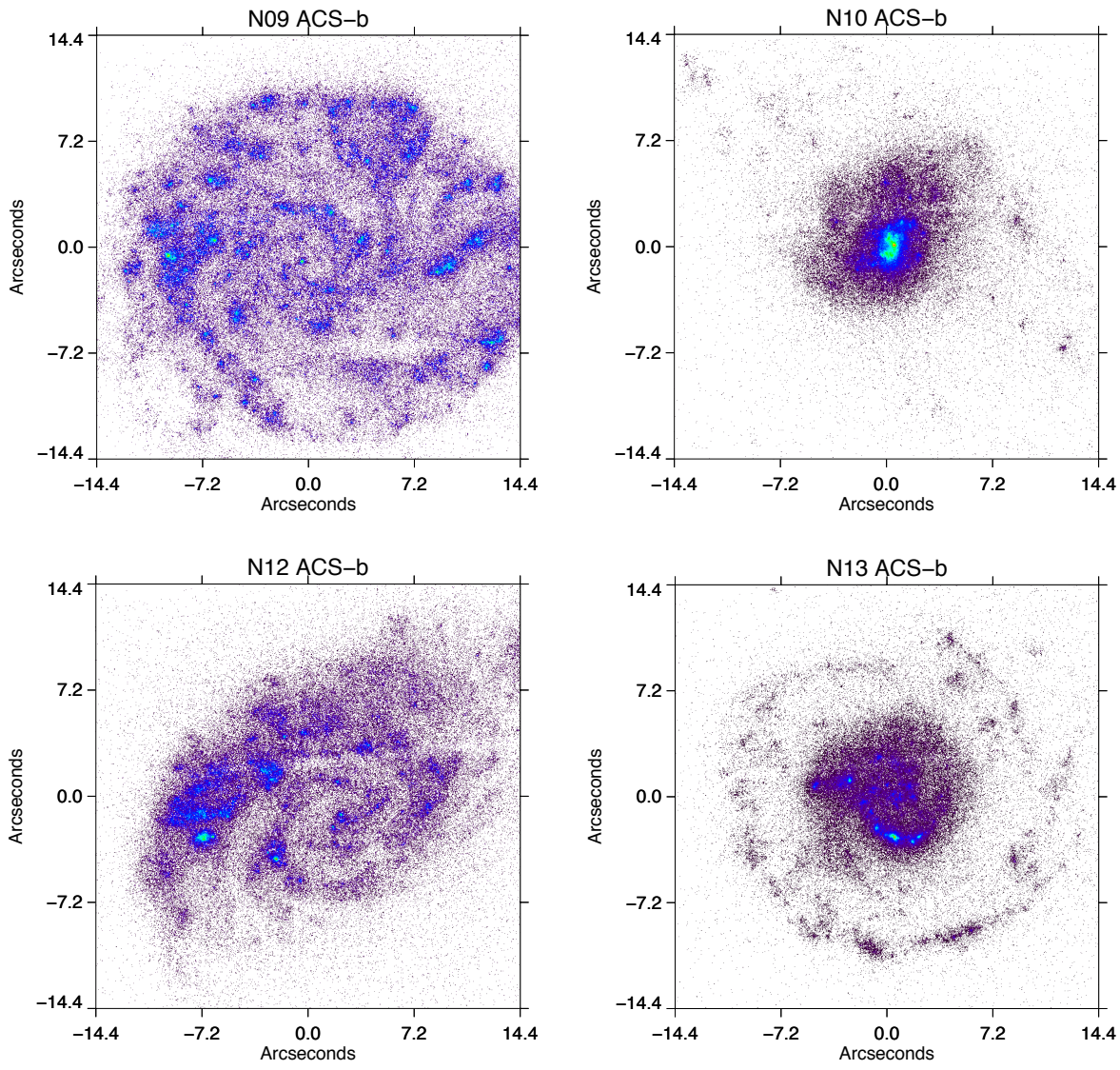

Figure A.3: ACS-b images for N09, N10, N12 and N13.

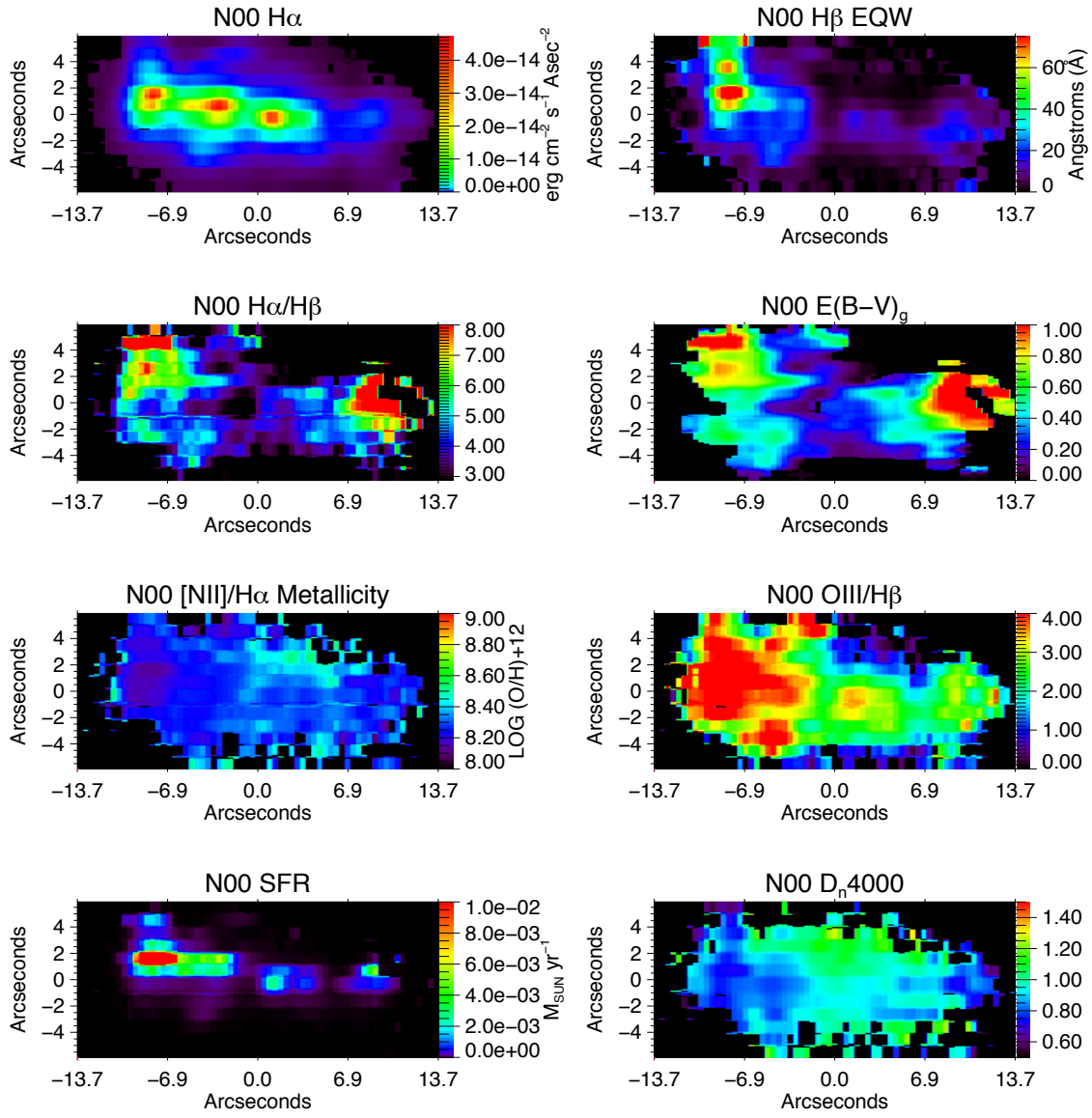

Figure A.4: Milky Way extinction corrected Hα flux and diagnostic maps from N00

in the continuum spectrum. These spikes prevent the data pipeline from properly scaling the red and blue fluxes to the same level. A subroutine was written to find and smooth these continuum anomalies, however it is possible that the scaling is still wrong. The E(B-V)$_g$ maps shows a band of very high extinction to the top, and a lesser on to the bottom of the map which could be the result of a slight underscaling of the blue channel. The continuum emission for N01 is so low in these regions that a small offset would result in a large miscalculation of Hβ.

There may be a slit misalignment at the bottom of the N03 spectral maps. The lower spiral arm appears to need to be further down to match with the SDSS.

Very poor observation conditions occurred on day 5 of the N04 campaign. As a result, the weak continuum and line emission at the bottom of N04 was not recoverable in many cases. This is why the lower part of N04 shows little to no emission of interest.

The spatial scale on the first night of observing N08 was set to bin the images by 2, therefore the spatial resolution of N08 is half that of the other targets. This has resulted in some Hα knots appearing stretched.

A.3 Lyα Escape Maps

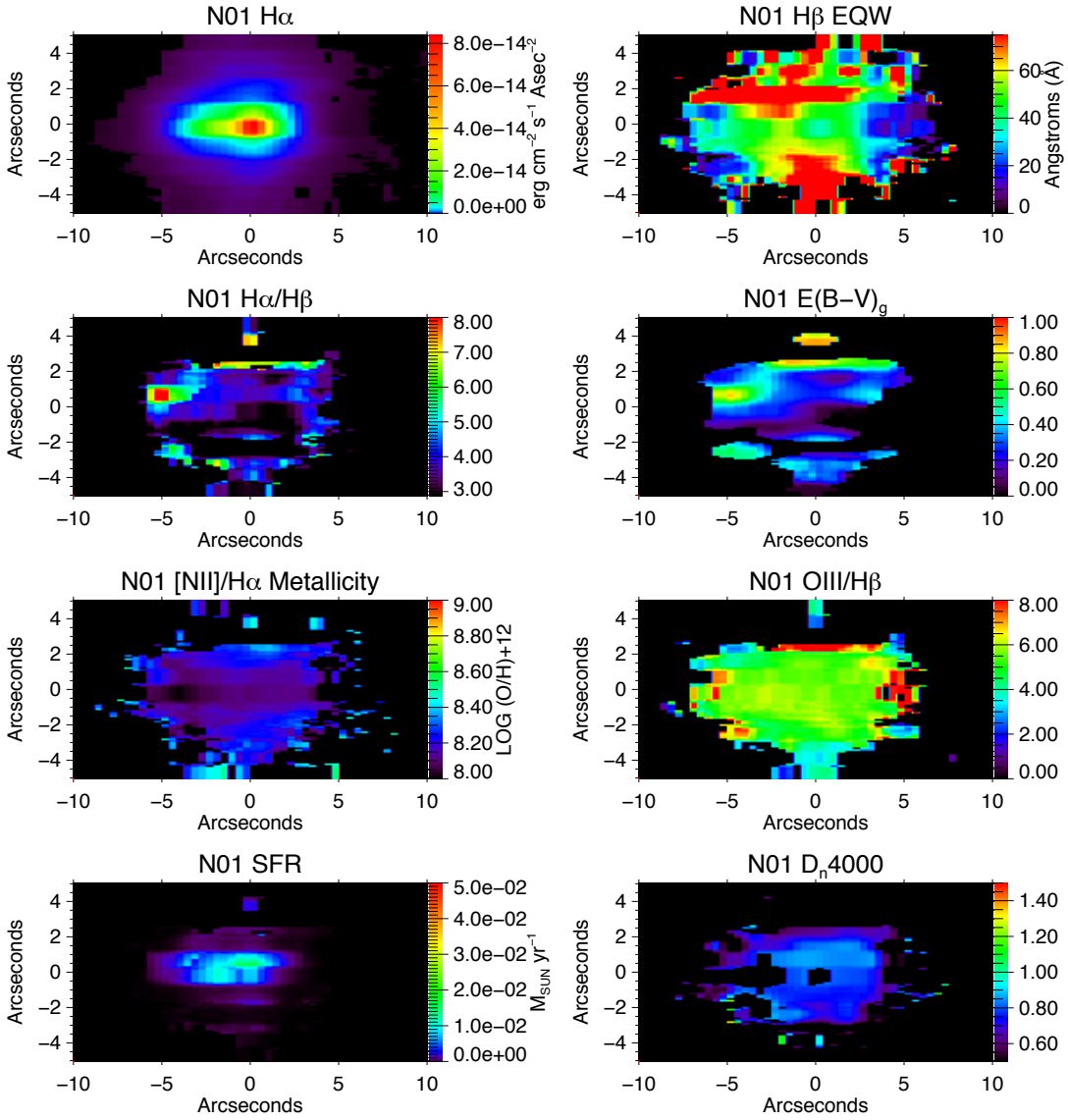

Figure A.5: Milky Way extinction corrected Hα flux and diagnostic maps from N01

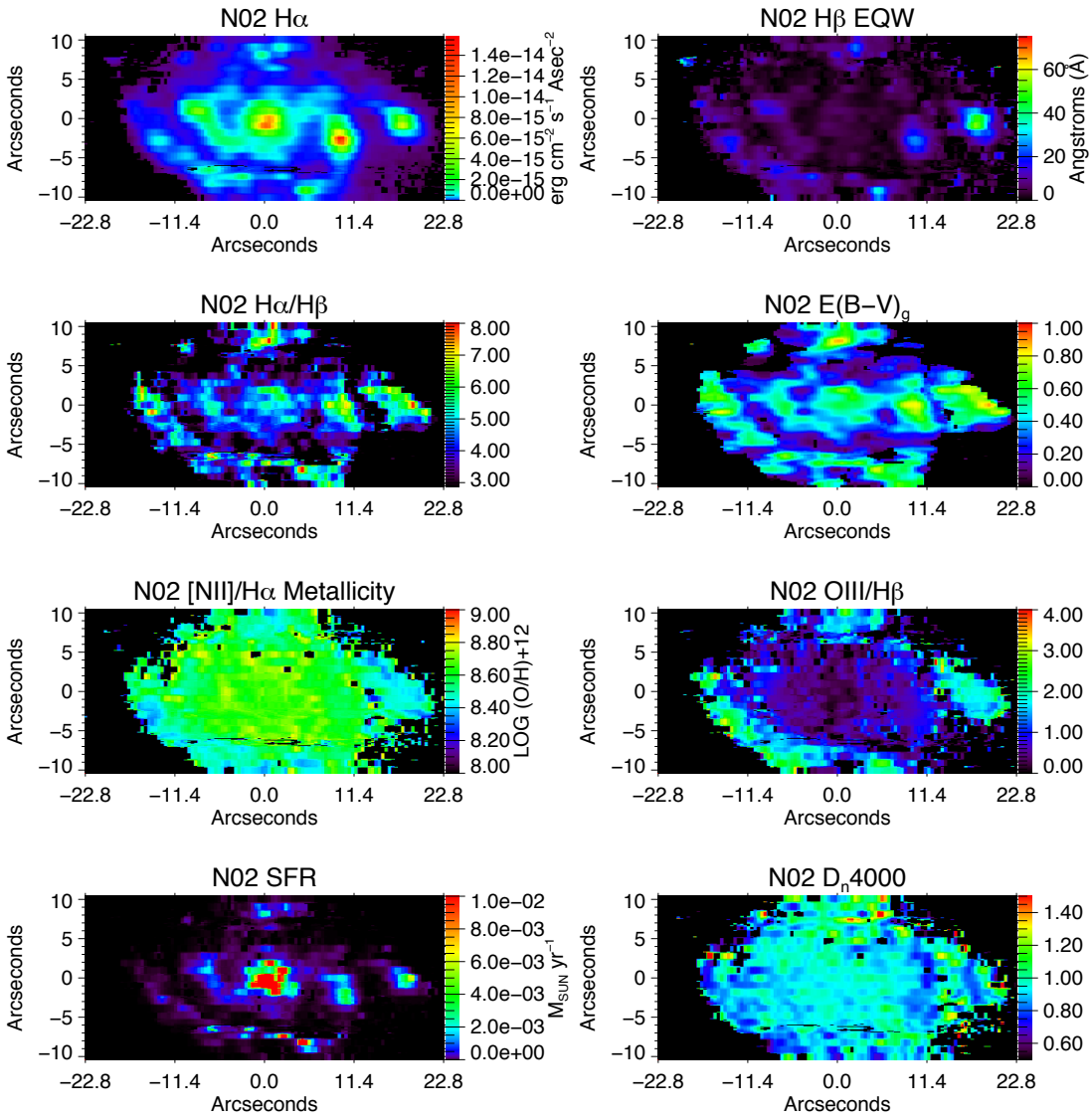

Figure A.6: Milky Way extinction corrected Hα flux and diagnostic maps from N02

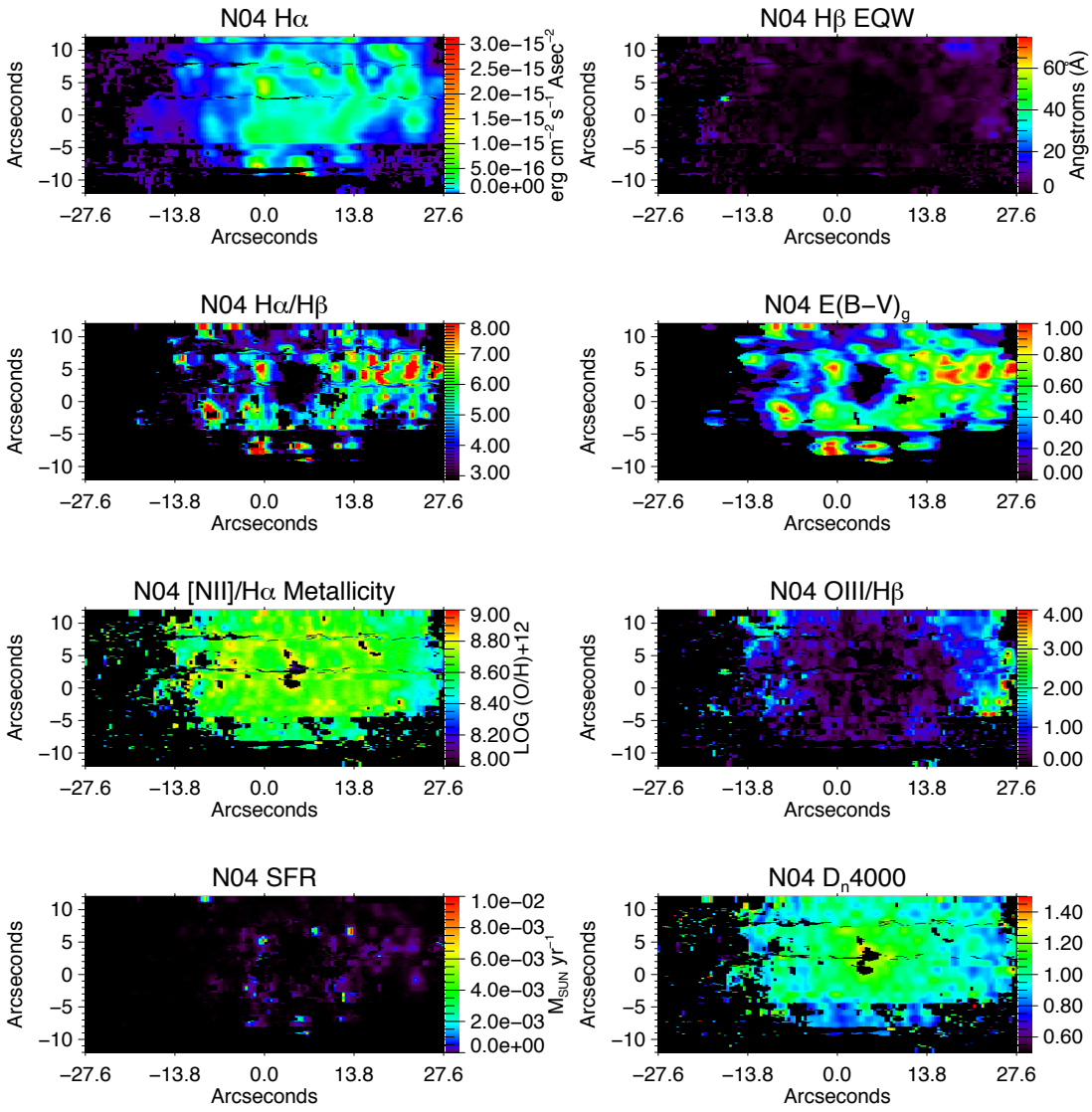

Figure A.7: Milky Way extinction corrected Hα flux and diagnostic maps from N04

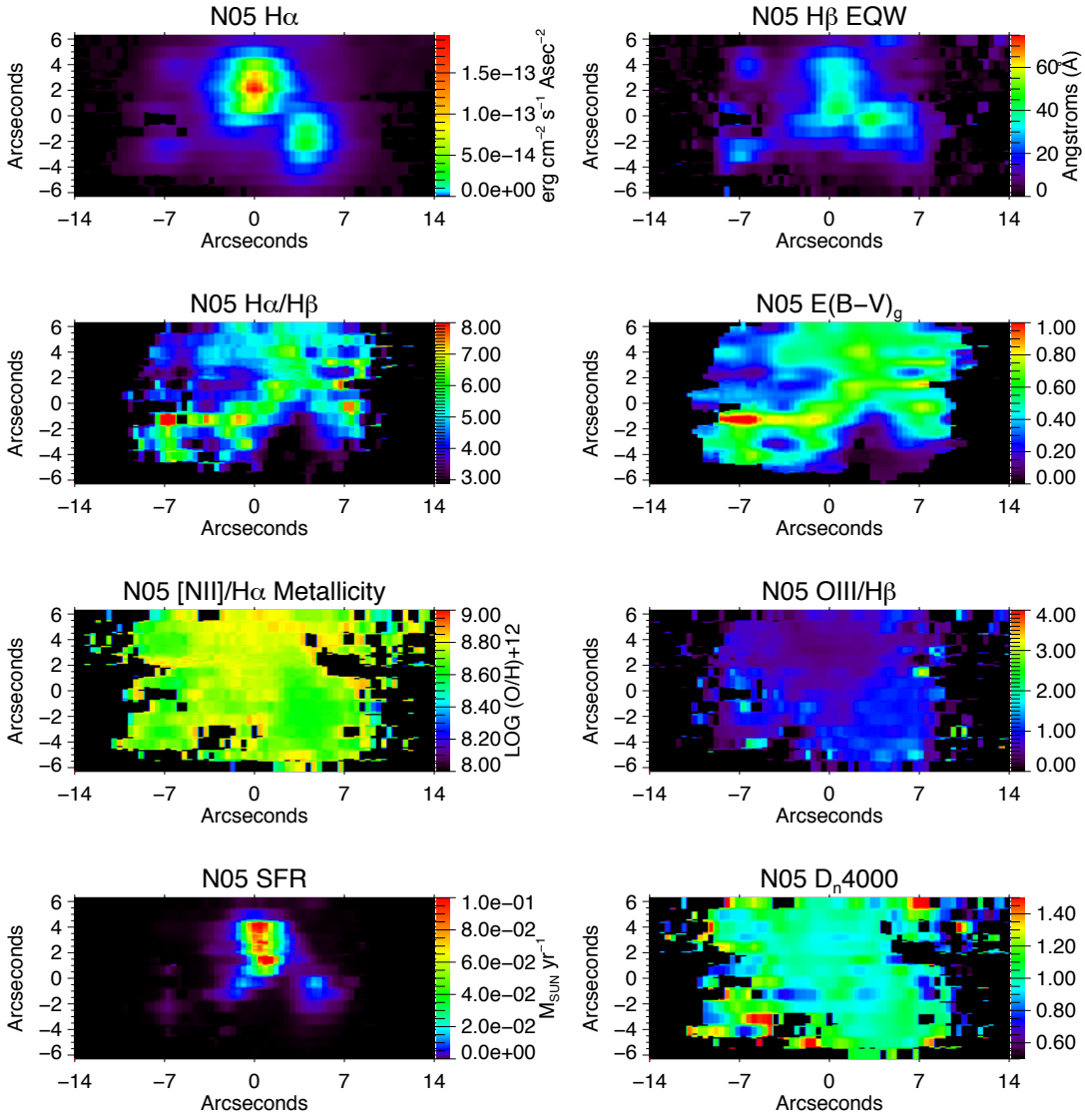

Figure A.8: Milky Way extinction corrected Hα flux and diagnostic maps from N05

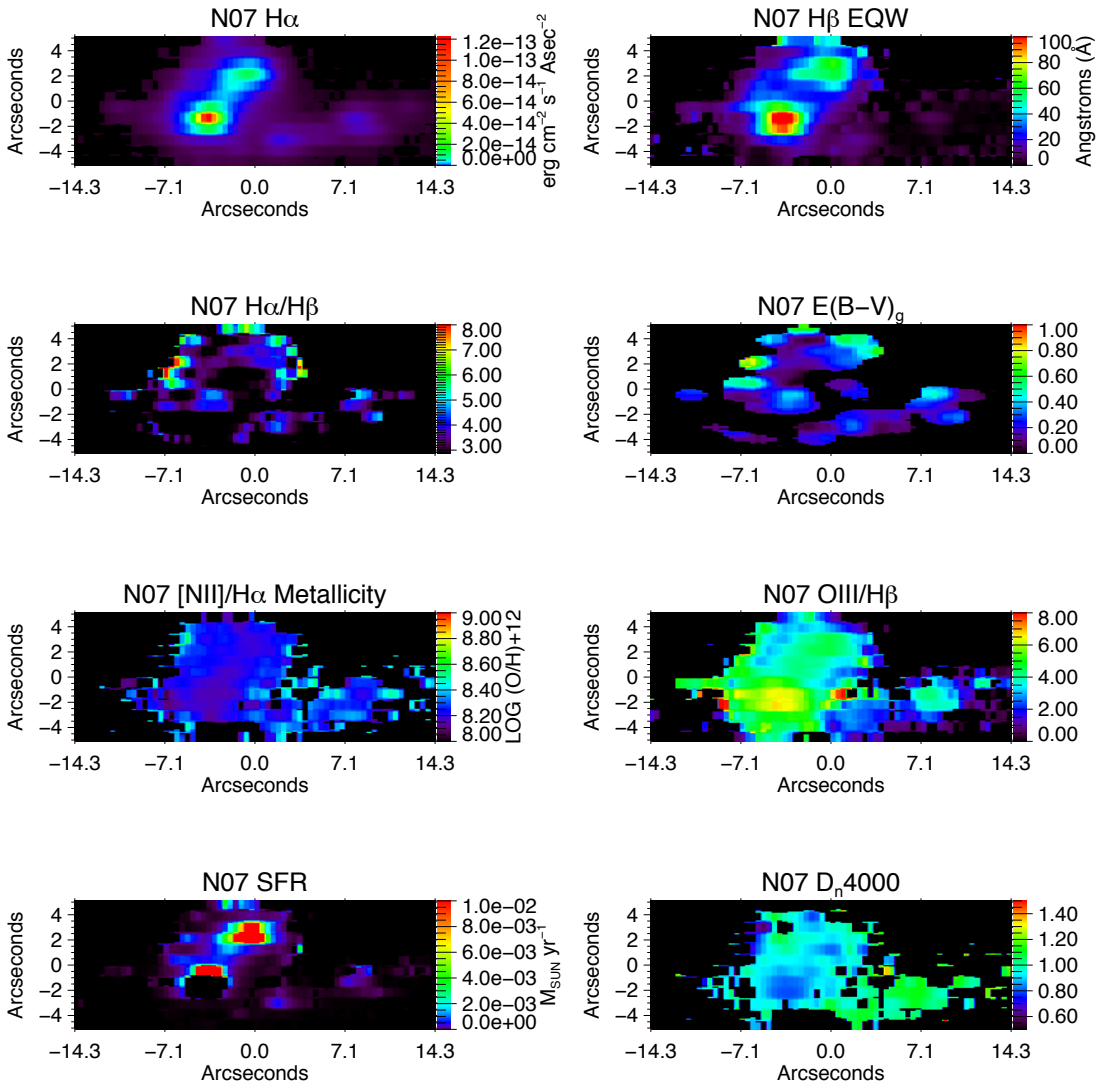

Figure A.9: Milky Way extinction corrected Hα flux and diagnostic maps from N07

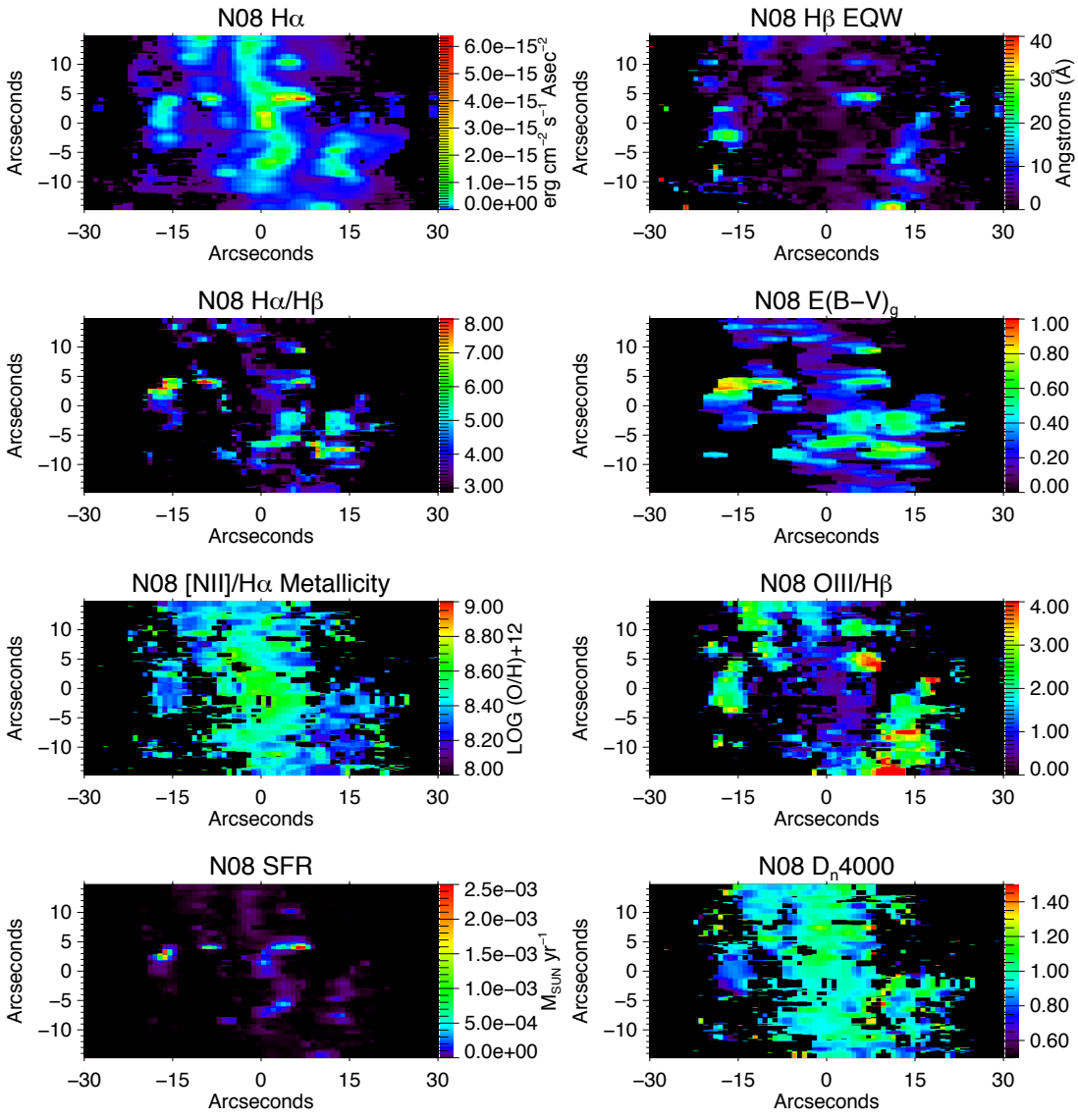

Figure A.10: Milky Way extinction corrected Hα flux and diagnostic maps from N08

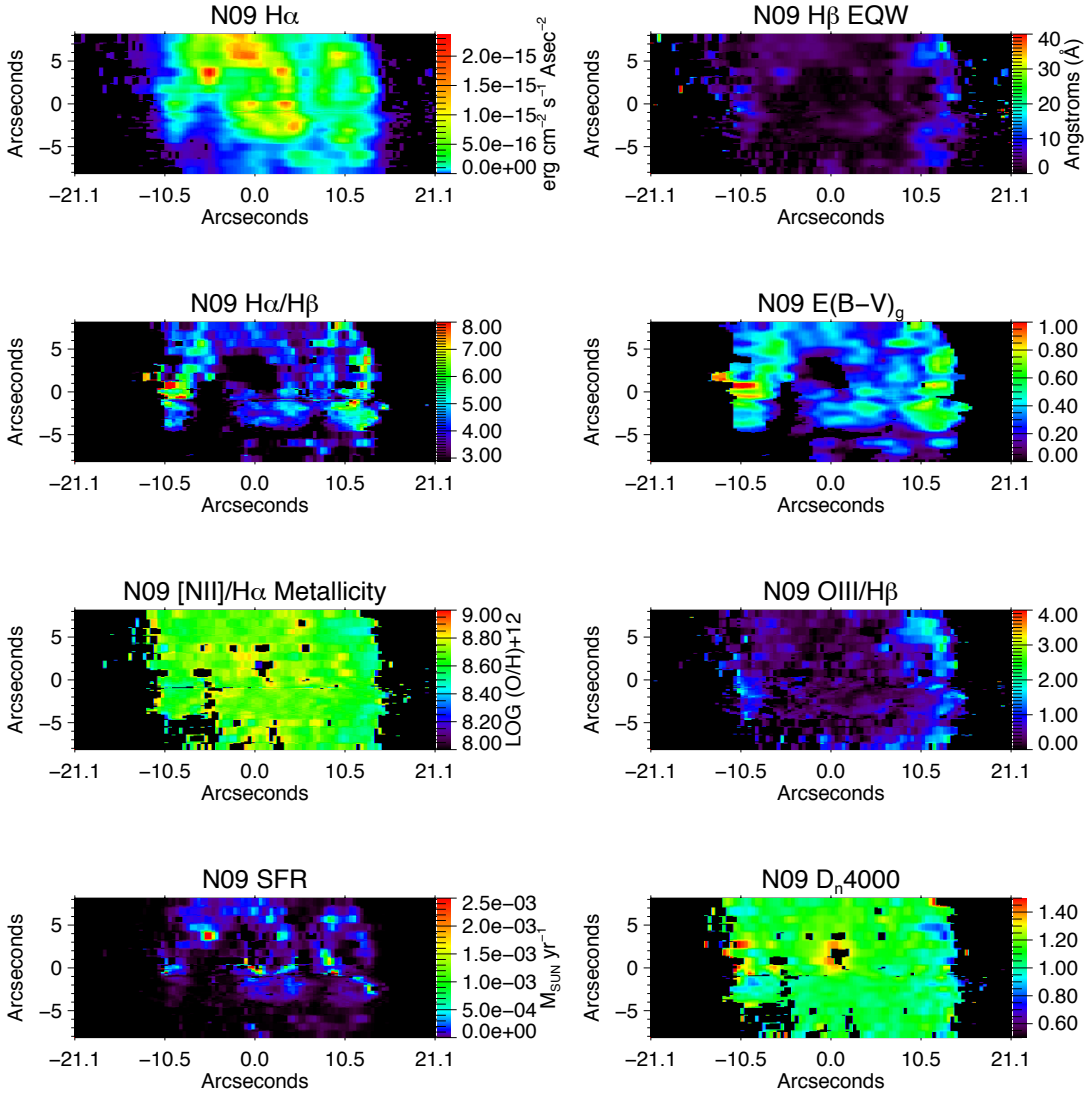

Figure A.11: Milky Way extinction corrected Hα flux and diagnostic maps from N09

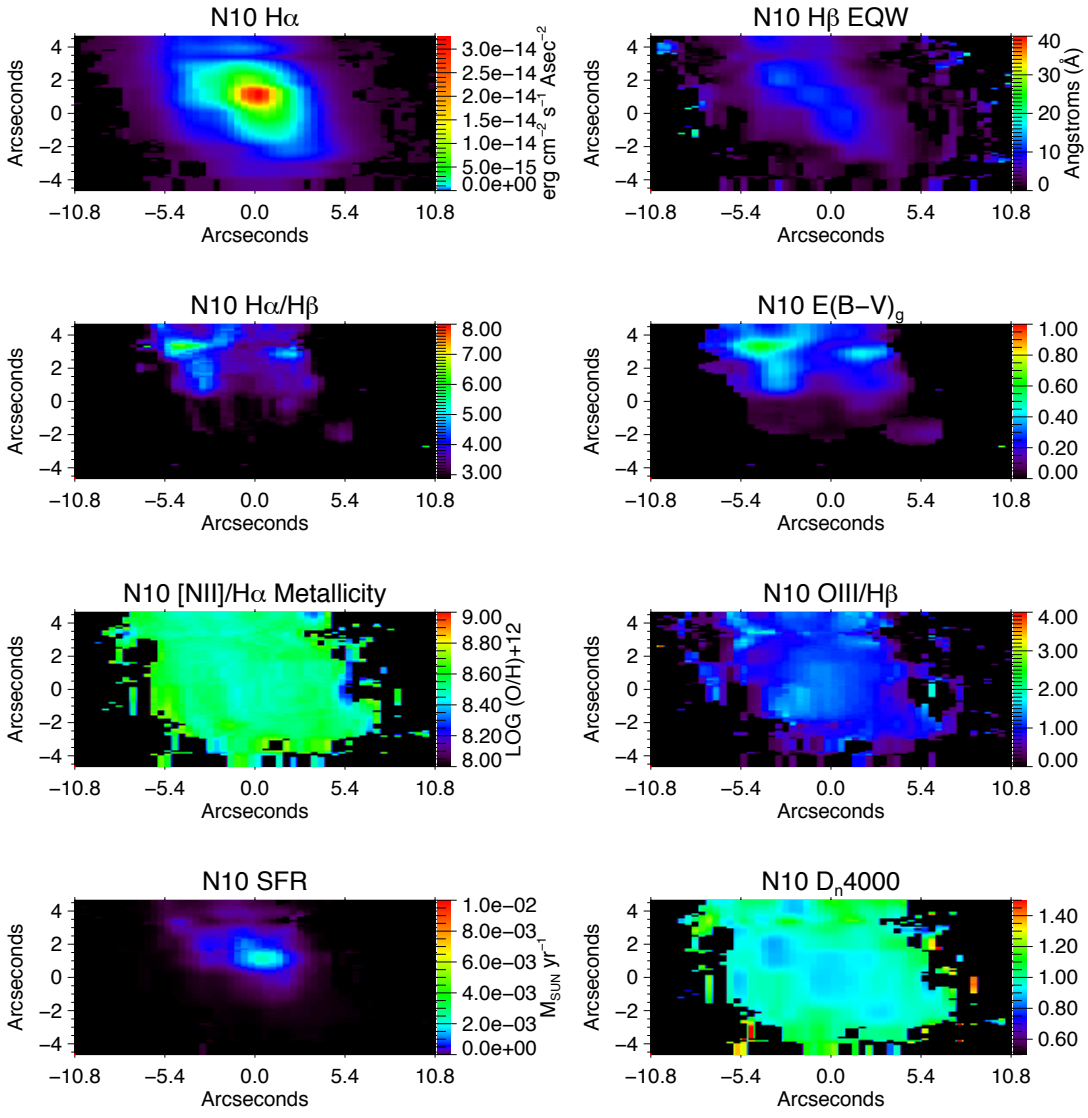

Figure A.12: Milky Way extinction corrected Hα flux and diagnostic maps from N10

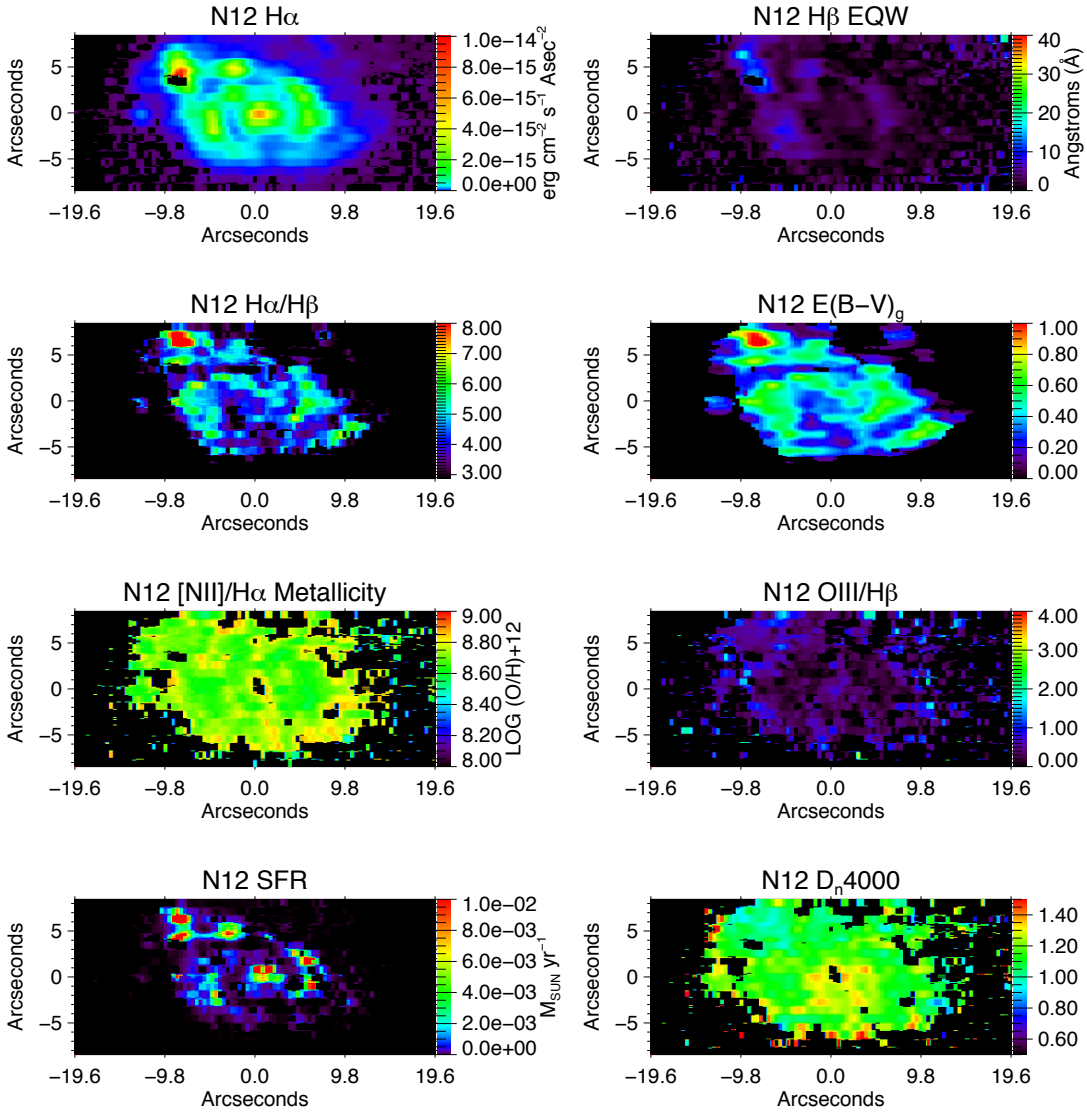

Figure A.13: Milky Way extinction corrected Hα flux and diagnostic maps from N12

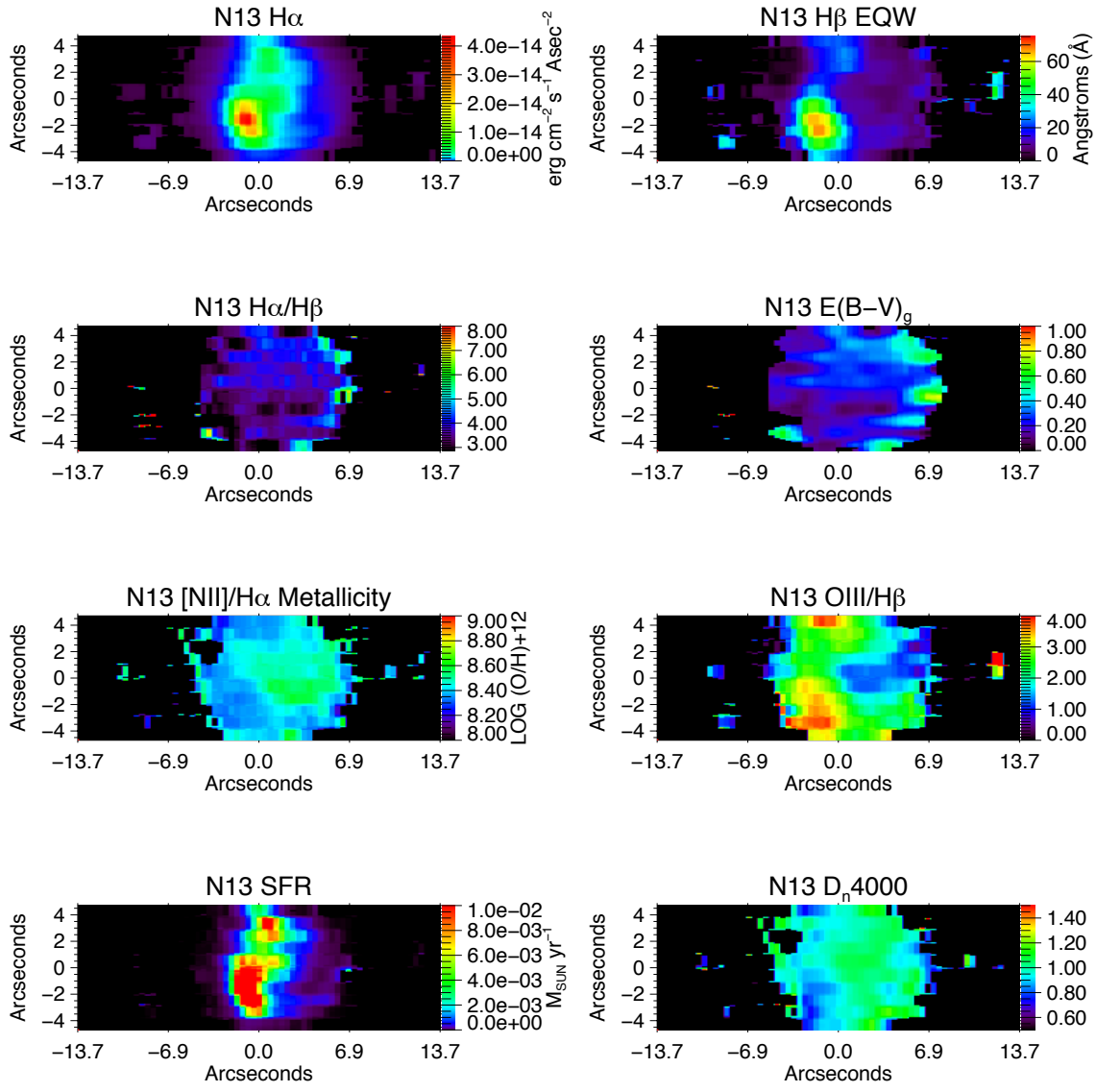

Figure A.14: Milky Way extinction corrected Hα flux and diagnostic maps from N13

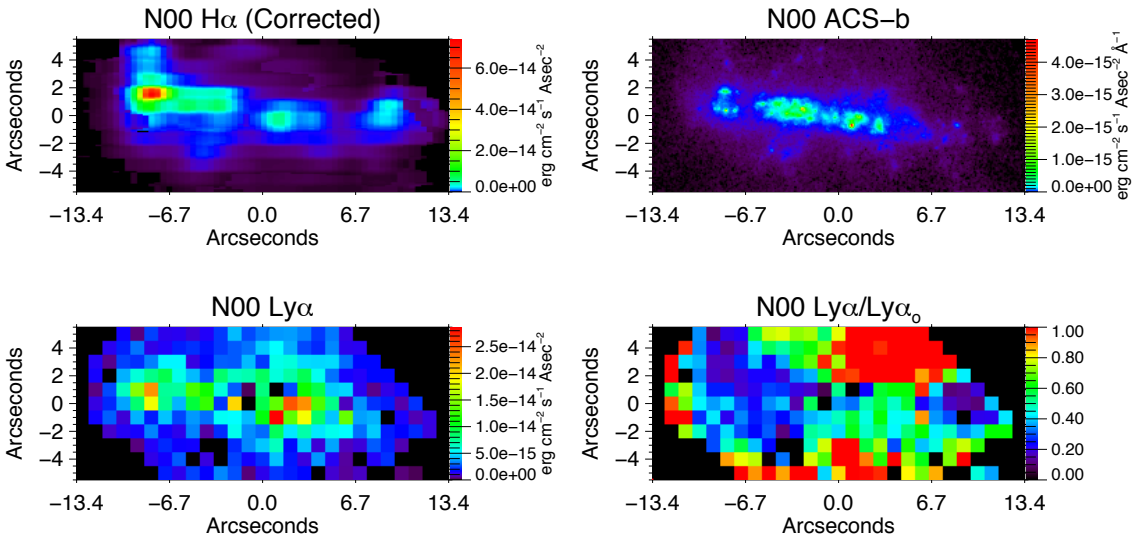

Figure A.15: Corrected Hα, ACS-b filter, Lyα emission, and $f_{Ly\alpha}$ maps for N00

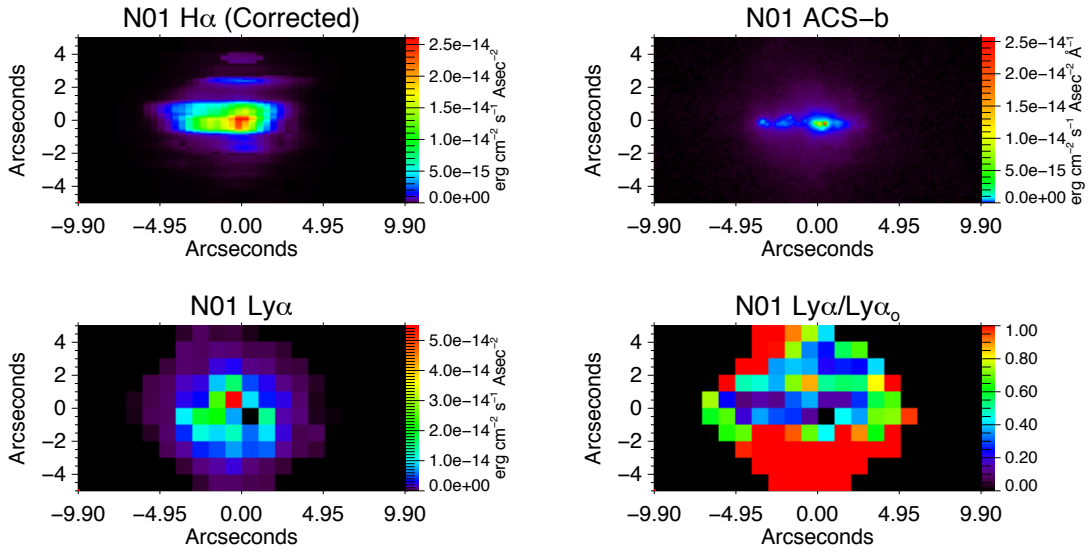

Figure A.16: Corrected Hα, ACS-b filter, Lyα emission, and $f_{Ly\alpha}$ maps for N01

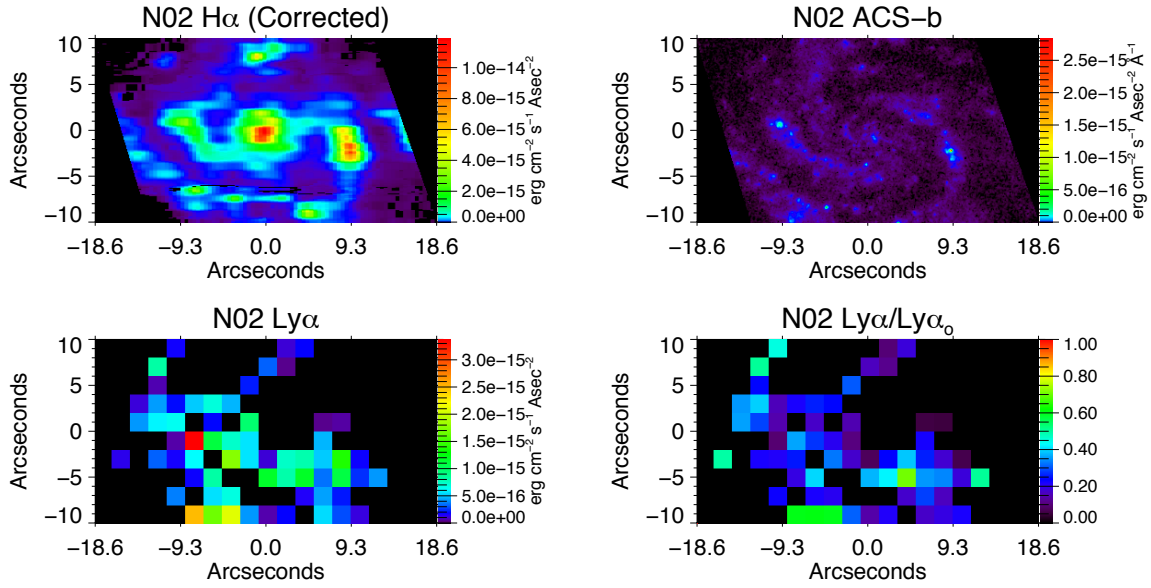

Figure A.17: Corrected Hα, ACS-b filter, Lyα emission, and $f_{Ly\alpha}$ maps for N02

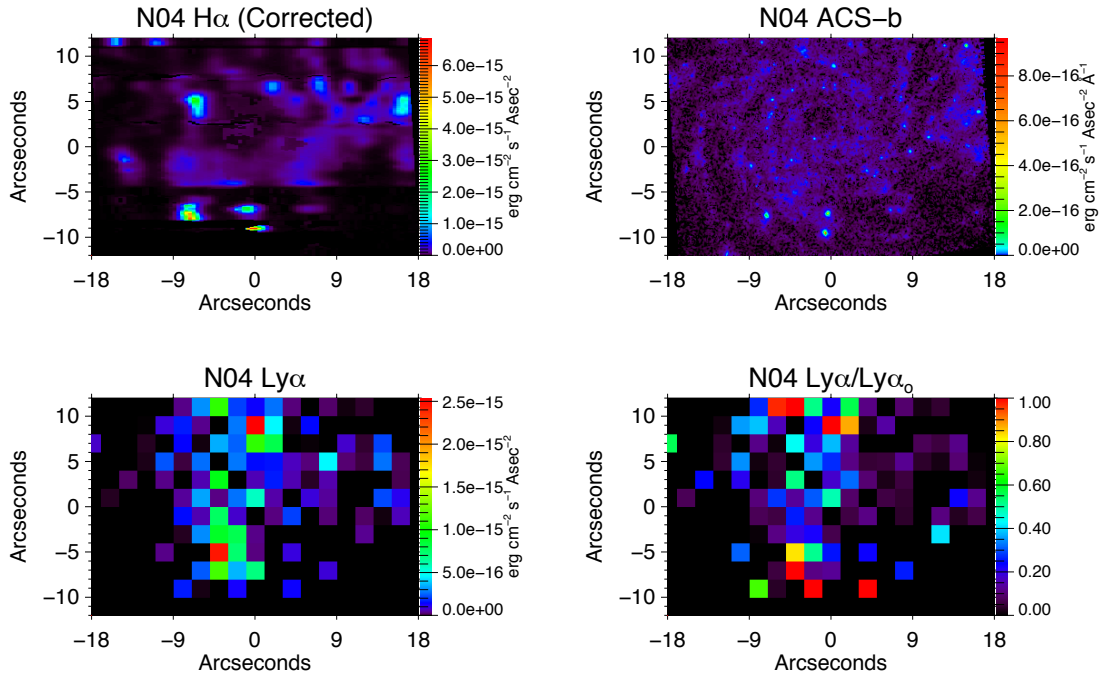

Figure A.18: Corrected Hα, ACS-b filter, Lyα emission, and $f_{Ly\alpha}$ maps for N04

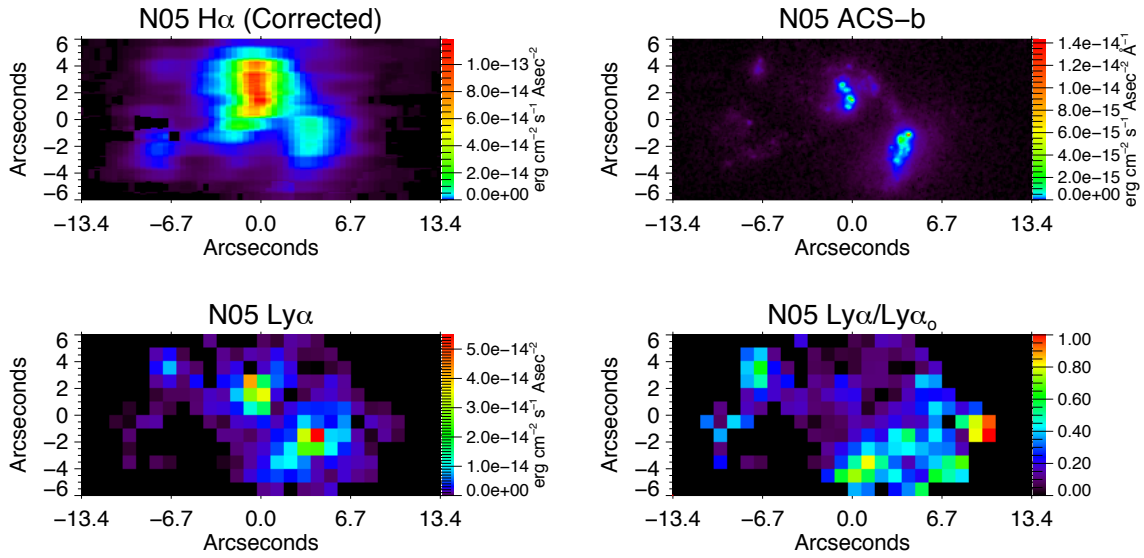

Figure A.19: Corrected Hα, ACS-b filter, Lyα emission, and $f_{Ly\alpha}$ maps for N05

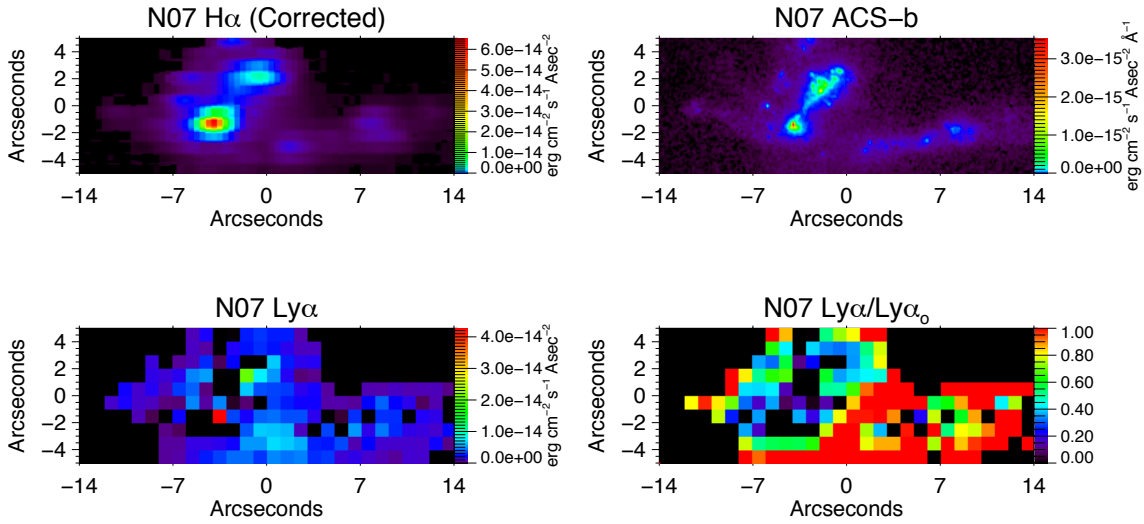

Figure A.20: Corrected Hα, ACS-b filter, Lyα emission, and $f_{Ly\alpha}$ maps for N07

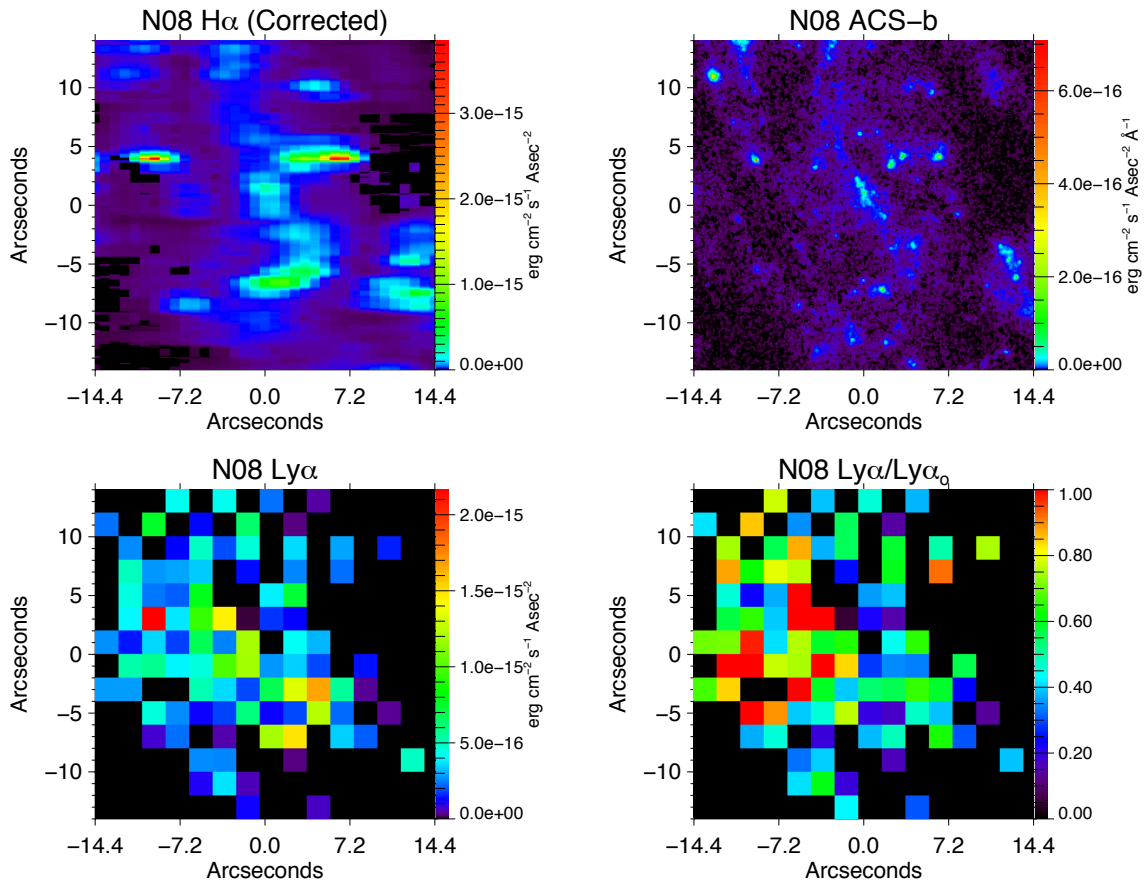

Figure A.21: Corrected Hα, ACS-b filter, Lyα emission, and $f_{Ly\alpha}$ maps for N08

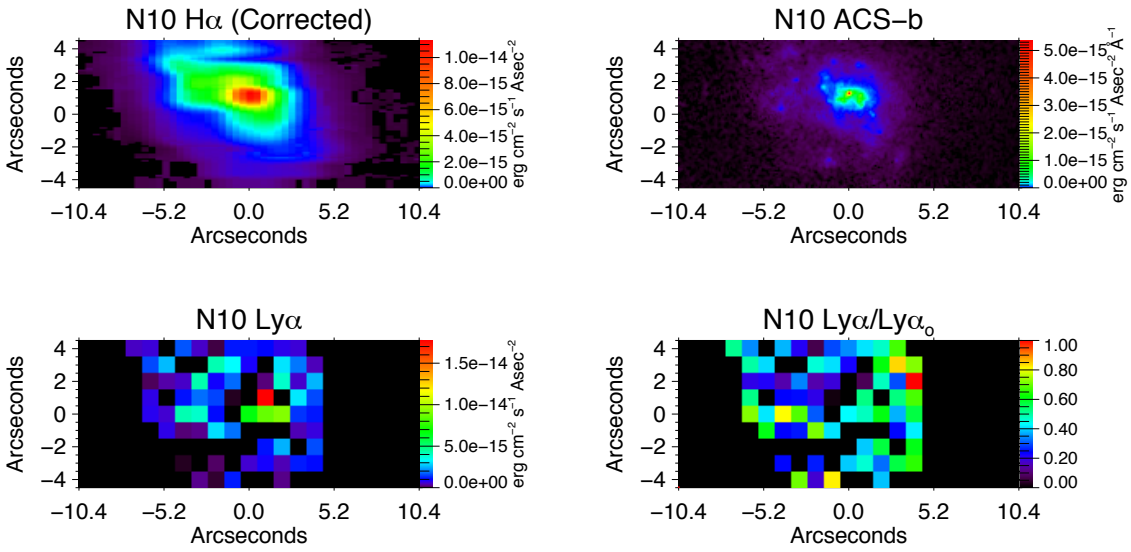

Figure A.22: Corrected Hα, ACS-b filter, Lyα emission, and $f_{Ly\alpha}$ maps for N10

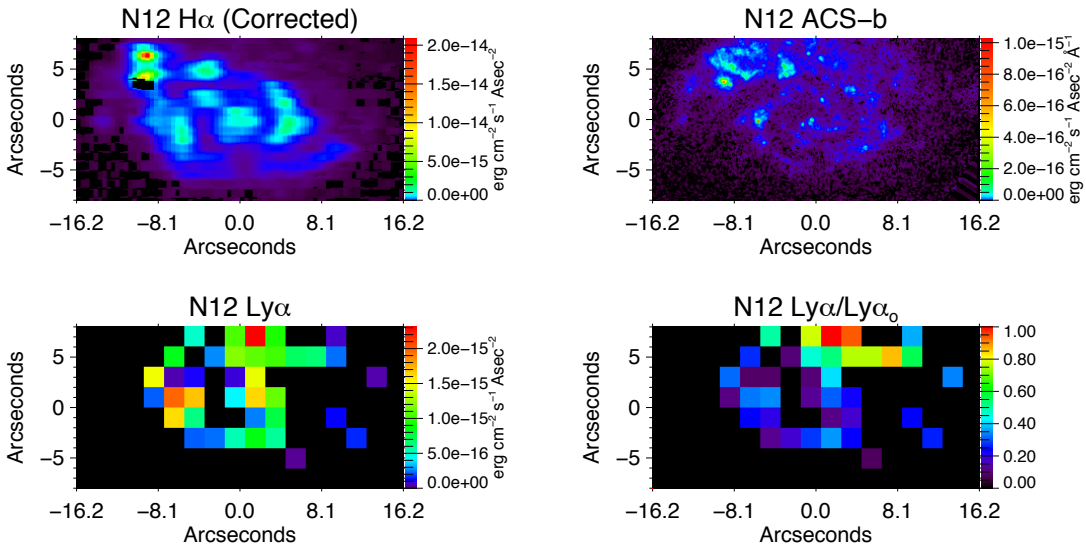

Figure A.23: Corrected Hα, ACS-b filter, Lyα emission, and $f_{Ly\alpha}$ maps for N12

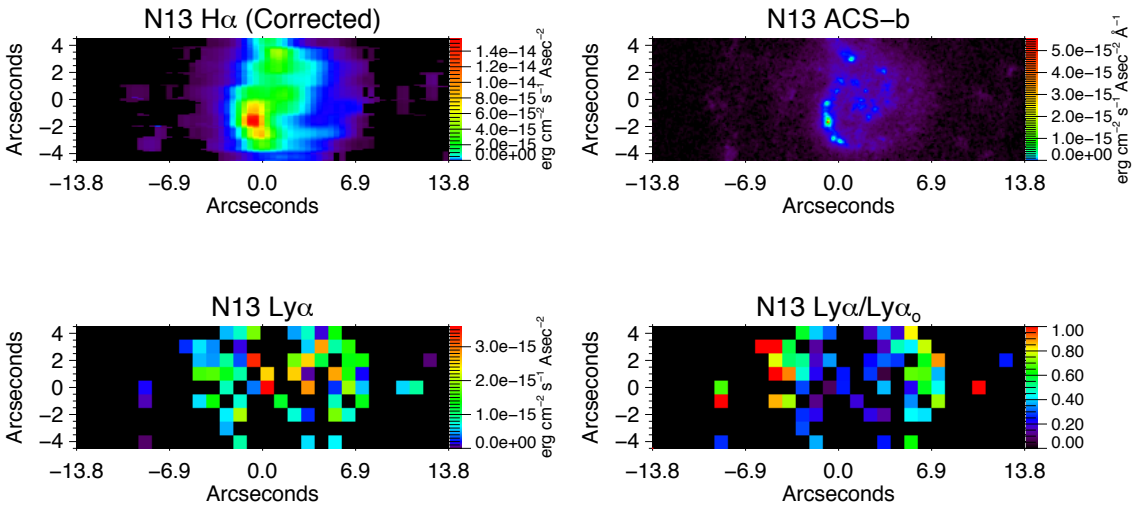

Figure A.24: Corrected Hα, ACS-b filter, Lyα emission, and $f_{Ly\alpha}$ maps for N13

Bibliography

[1] R. S. Ellis, R. J. McLure, J. S. Dunlop, B. E. Robertson, Y. Ono, M. A. Schenker, A. Koekemoer, R. A. A. Bowler, M. Ouchi, A. B. Rogers, E. Curtis-Lake, E. Schneider, S. Charlot, D. P. Stark, S. R. Furlanetto, and M. Cirasuolo, "The Abundance of Star-forming Galaxies in the Redshift Range 8.5-12: New Results from the 2012 Hubble Ultra Deep Field Campaign," *ApJL*, vol. 763, p. L7, Jan. 2013.

[2] J. E. Gunn and B. A. Peterson, "On the Density of Neutral Hydrogen in Intergalactic Space." *ApJ*, vol. 142, pp. 1633–1641, Nov. 1965.

[3] R. H. Becker, X. Fan, R. L. White, M. A. Strauss, V. K. Narayanan, R. H. Lupton, J. E. Gunn, J. Annis, N. A. Bahcall, J. Brinkmann, A. J. Connolly, I. Csabai, P. C. Czarapata, M. Doi, T. M. Heckman, G. S. Hennessy, Ž. Ivezić, G. R. Knapp, D. Q. Lamb, T. A. McKay, J. A. Munn, T. Nash, R. Nichol, J. R. Pier, G. T. Richards, D. P. Schneider, C. Stoughton, A. S. Szalay, A. R. Thakar, and D. G. York, "Evidence for Reionization at z˜6: Detection of a Gunn-Peterson

Trough in a z=6.28 Quasar," *AJ*, vol. 122, pp. 2850–2857, Dec. 2001.

[4] G. Hinshaw, J. L. Weiland, R. S. Hill, N. Odegard, D. Larson, C. L. Bennett, J. Dunkley, B. Gold, M. R. Greason, N. Jarosik, E. Komatsu, M. R. Nolta, L. Page, D. N. Spergel, E. Wollack, M. Halpern, A. Kogut, M. Limon, S. S. Meyer, G. S. Tucker, and E. L. Wright, "Five-Year Wilkinson Microwave Anisotropy Probe Observations: Data Processing, Sky Maps, and Basic Results," *ApJS*, vol. 180, pp. 225–245, Feb. 2009.

[5] C. L. Bennett, M. Bay, M. Halpern, G. Hinshaw, C. Jackson, N. Jarosik, A. Kogut, M. Limon, S. S. Meyer, L. Page, D. N. Spergel, G. S. Tucker, D. T. Wilkinson, E. Wollack, and E. L. Wright, "The Microwave Anisotropy Probe Mission," *ApJ*, vol. 583, pp. 1–23, Jan. 2003.

[6] Z. Haiman and A. Loeb, "Observational Signatures of the First Quasars," *ApJ*, vol. 503, p. 505, Aug. 1998.

[7] X. Fan, V. K. Narayanan, R. H. Lupton, M. A. Strauss, G. R. Knapp, R. H. Becker, R. L. White, L. Pentericci, S. K. Leggett, Z. Haiman, J. E. Gunn, Ž. Ivezić, D. P. Schneider, S. F. Anderson, J. Brinkmann, N. A. Bahcall, A. J. Connolly, I. Csabai, M. Doi, M. Fukugita, T. Geballe, E. K. Grebel, D. Harbeck, G. Hennessy, D. Q. Lamb, G. Miknaitis, J. A. Munn, R. Nichol, S. Okamura, J. R. Pier, F. Prada, G. T. Richards, A. Szalay, and D. G. York, "A Survey of z>5.8 Quasars in the Sloan Digital Sky Survey. I. Discovery of Three New

Quasars and the Spatial Density of Luminous Quasars at z˜6," *AJ*, vol. 122, pp. 2833–2849, Dec. 2001.

[8] P. Madau, F. Haardt, and M. J. Rees, "Radiative Transfer in a Clumpy Universe. III. The Nature of Cosmological Ionizing Sources," *ApJ*, vol. 514, pp. 648–659, Apr. 1999.

[9] K. Wood and A. Loeb, "Escape of Ionizing Radiation from High-Redshift Galaxies," *ApJ*, vol. 545, pp. 86–99, Dec. 2000.

[10] E. Giallongo, A. Fontana, and P. Madau, "The Stellar UV Background at z<1.5 and the Baryon Density of Photoionized Gas," *MNRAS*, vol. 289, pp. 629–633, Aug. 1997.

[11] J. M. Shull, D. Roberts, M. L. Giroux, S. V. Penton, and M. A. Fardal, "The Metagalactic Ionizing Radiation Field at Low Redshift," *AJ*, vol. 118, pp. 1450–1460, Oct. 1999.

[12] Z. Haiman and A. Loeb, "Signatures of Stellar Reionization of the Universe," *ApJ*, vol. 483, p. 21, Jul. 1997.

[13] C. C. Steidel, K. L. Adelberger, M. Giavalisco, M. Dickinson, and M. Pettini, "Lyman-Break Galaxies at z<˜4 and the Evolution of the Ultraviolet Luminosity Density at High Redshift," *ApJ*, vol. 519, pp. 1–17, Jul. 1999.

BIBLIOGRAPHY

[14] R. C. Kennicutt, Jr., "The Global Schmidt Law in Star-forming Galaxies," *ApJ*, vol. 498, p. 541, May 1998.

[15] C. C. Steidel, M. Pettini, and K. L. Adelberger, "Lyman-Continuum Emission from Galaxies at Z ˜= 3.4," *ApJ*, vol. 546, pp. 665–671, Jan. 2001.

[16] M. Pettini, M. Kellogg, C. C. Steidel, M. Dickinson, K. L. Adelberger, and M. Giavalisco, "Infrared Observations of Nebular Emission Lines from Galaxies at Z ˜= 3," *ApJ*, vol. 508, pp. 539–550, Dec. 1998.

[17] T. M. Heckman, "Starburst-Driven Galactic Winds," in *Revista Mexicana de Astronomia y Astrofisica Conference Series*, ser. Revista Mexicana de Astronomia y Astrofisica, vol. 27, V. Avila-Reese, C. Firmani, C. S. Frenk, and C. Allen, Eds., vol. 17, Jun. 2003, pp. 47–55.

[18] M. D. Lehnert and T. M. Heckman, "Ionized Gas in the Halos of Edge-on Starburst Galaxies: Evidence for Supernova-driven Superwinds," *ApJ*, vol. 462, p. 651, May 1996.

[19] J. B. Dove, J. M. Shull, and A. Ferrara, "The Escape of Ionizing Photons from OB Associations in Disk Galaxies: Radiation Transfer through Superbubbles," *ApJ*, vol. 531, pp. 846–860, Mar. 2000.

[20] P. Boisse, "Radiative transfer inside clumpy media - The penetration of UV photons inside molecular clouds," *AAp*, vol. 228, pp. 483–502, Feb. 1990.

[21] C. Leitherer, H. C. Ferguson, T. M. Heckman, and J. D. Lowenthal, "The Lyman Continuum in Starburst Galaxies Observed with the Hopkins Ultraviolet Telescope," *ApJL*, vol. 454, p. L19, Nov. 1995.

[22] J.-M. Deharveng, V. Buat, V. Le Brun, B. Milliard, D. Kunth, J. M. Shull, and C. Gry, "Constraints on the Lyman continuum radiation from galaxies: First results with FUSE on Mrk 54," *AAp*, vol. 375, pp. 805–813, Sep. 2001.

[23] T. M. Heckman, K. R. Sembach, G. R. Meurer, C. Leitherer, D. Calzetti, and C. L. Martin, "On the Escape of Ionizing Radiation from Starbursts," *ApJ*, vol. 558, pp. 56–62, Sep. 2001.

[24] J. P. Grimes, T. Heckman, A. Aloisi, D. Calzetti, C. Leitherer, C. L. Martin, G. Meurer, K. Sembach, and D. Strickland, "Observations of Starburst Galaxies With Far-Ultraviolet Spectrographic Explorer: Galactic Feedback in the Local Universe," *ApJS*, vol. 181, pp. 272–320, Mar. 2009.

[25] H. C. Ferguson, "The Hubble Deep Field in the Far Ultraviolet," in *Deep Fields*, S. Cristiani, A. Renzini, and R. E. Williams, Eds., 2001, p. 54.

[26] B. Siana, H. I. Teplitz, H. C. Ferguson, T. M. Brown, M. Giavalisco, M. Dickinson, R.-R. Chary, D. F. de Mello, C. J. Conselice, C. R. Bridge, J. P. Gardner, J. W. Colbert, and C. Scarlata, "A Deep Hubble Space Telescope Search for Escaping Lyman Continuum Flux at z ˜ 1.3: Evidence for an Evolving Ionizing Emissivity," *ApJ*, vol. 723, pp. 241–250, Nov. 2010.

[27] A. E. Shapley, C. C. Steidel, M. Pettini, K. L. Adelberger, and D. K. Erb, "The Direct Detection of Lyman Continuum Emission from Star-forming Galaxies at z˜3," *ApJ*, vol. 651, pp. 688–703, Nov. 2006.

[28] D. B. Nestor, A. E. Shapley, C. C. Steidel, and B. Siana, "Narrowband Imaging of Escaping Lyman-continuum Emission in the SSA22 Field," *ApJ*, vol. 736, p. 18, Jul. 2011.

[29] B. T. Fleming, S. R. McCandliss, M. E. Kaiser, J. Kruk, P. D. Feldman, A. S. Kutyrev, M. J. Li, D. A. Rapchun, E. Lyness, S. H. Moseley, O. Siegmund, J. Vallerga, and A. Martin, "Fabrication and calibration of FORTIS," in *Society of Photo-Optical Instrumentation Engineers (SPIE) Conference Series*, ser. Society of Photo-Optical Instrumentation Engineers (SPIE) Conference Series, vol. 8145, Sep. 2011.

[30] E. R. Fernandez and J. M. Shull, "The Effect of Galactic Properties on the Escape Fraction of Ionizing Photons," *ApJ*, vol. 731, p. 20, Apr. 2011.

[31] A. Benson, A. Venkatesan, and J. M. Shull, "The Escape Fraction of Ionizing Radiation from Galaxies," *ApJ*, vol. 770, p. 76, Jun. 2013.

[32] H. Yajima, J.-H. Choi, and K. Nagamine, "Escape fraction of ionizing photons from high-redshift galaxies in cosmological SPH simulations," *MNRAS*, vol. 412, pp. 411–422, Mar. 2011.

[33] N. Y. Gnedin, A. V. Kravtsov, and H.-W. Chen, "Escape of Ionizing Radiation from High-Redshift Galaxies," *ApJ*, vol. 672, pp. 765–775, Jan. 2008.

[34] J. M. Shull, A. Harness, M. Trenti, and B. D. Smith, "Critical Star Formation Rates for Reionization: Full Reionization Occurs at Redshift z $\approx$ 7," *ApJ*, vol. 747, p. 100, Mar. 2012.

[35] J. H. Wise and R. Cen, "Ionizing Photon Escape Fractions From High-Redshift Dwarf Galaxies," *ApJ*, vol. 693, pp. 984–999, Mar. 2009.

[36] M. Ricotti and J. M. Shull, "Feedback from Galaxy Formation: Escaping Ionizing Radiation from Galaxies at High Redshift," *ApJ*, vol. 542, pp. 548–558, Oct. 2000.

[37] B. E. Robertson, S. R. Furlanetto, E. Schneider, S. Charlot, R. S. Ellis, D. P. Stark, R. J. McLure, J. S. Dunlop, A. Koekemoer, M. A. Schenker, M. Ouchi, Y. Ono, E. Curtis-Lake, A. B. Rogers, R. A. A. Bowler, and M. Cirasuolo, "New Constraints on Cosmic Reionization from the 2012 Hubble Ultra Deep Field Campaign," *ApJ*, vol. 768, p. 71, May 2013.

[38] A. K. Inoue and I. Iwata, "A Monte Carlo simulation of the intergalactic absorption and the detectability of the Lyman continuum from distant galaxies," *MNRAS*, vol. 387, pp. 1681–1692, Jul. 2008.

[39] M. Stiavelli, S. M. Fall, and N. Panagia, "Observable Properties of Cosmological Reionization Sources," *ApJ*, vol. 600, pp. 508–519, Jan. 2004.

[40] D. E. Osterbrock and G. J. Ferland, *Astrophysics of gaseous nebulae and active galactic nuclei*, 2006.

[41] C. Gronwall, R. Ciardullo, T. Hickey, E. Gawiser, J. J. Feldmeier, P. G. van Dokkum, C. M. Urry, D. Herrera, B. D. Lehmer, L. Infante, A. Orsi, D. Marchesini, G. A. Blanc, H. Francke, P. Lira, and E. Treister, "Lyα Emission-Line Galaxies at z = 3.1 in the Extended Chandra Deep Field-South," *ApJ*, vol. 667, pp. 79–91, Sep. 2007.

[42] Z.-Y. Zheng, S. Malhotra, J.-X. Wang, J. E. Rhoads, S. L. Finkelstein, E. Gawiser, C. Gronwall, L. Guaita, K. K. Nilsson, and R. Ciardullo, "X-Ray Constraints on the Lyα Escape Fraction," *ApJ*, vol. 746, p. 28, Feb. 2012.

[43] D. Schaerer, "On the properties of massive Population III stars and metal-free stellar populations," *AAp*, vol. 382, pp. 28–42, Jan. 2002.

[44] S. Malhotra and J. E. Rhoads, "Large Equivalent Width Lyα line Emission at z=4.5: Young Galaxies in a Young Universe?" *ApJL*, vol. 565, pp. L71–L74, Feb. 2002.

[45] S. L. Finkelstein, S. H. Cohen, S. Malhotra, and J. E. Rhoads, "Evolution of

Lyα Galaxies: Stellar Populations at z ˜ 0.3," *ApJ*, vol. 700, pp. 276–283, Jul. 2009.

[46] D. A. Neufeld, "The escape of Lyman-alpha radiation from a multiphase interstellar medium," *ApJL*, vol. 370, pp. L85–L88, Apr. 1991.

[47] M. Dijkstra, Z. Haiman, and M. Spaans, "Lyα Radiation from Collapsing Protogalaxies. I. Characteristics of the Emergent Spectrum," *ApJ*, vol. 649, pp. 14–36, Sep. 2006.

[48] A. Wofford, C. Leitherer, and J. Salzer, "Lyα Escape from z ˜ 0.03 Star-forming Galaxies: The Dominant Role of Outflows," *ApJ*, vol. 765, p. 118, Mar. 2013.

[49] M. Hansen and S. P. Oh, "Lyman α radiative transfer in a multiphase medium," *MNRAS*, vol. 367, pp. 979–1002, Apr. 2006.

[50] C. C. Steidel, M. Bogosavljević, A. E. Shapley, J. A. Kollmeier, N. A. Reddy, D. K. Erb, and M. Pettini, "Diffuse Lyα Emitting Halos: A Generic Property of High-redshift Star-forming Galaxies," *ApJ*, vol. 736, p. 160, Aug. 2011.

[51] N. Kashikawa, T. Nagao, J. Toshikawa, Y. Ishizaki, E. Egami, M. Hayashi, C. Ly, M. A. Malkan, Y. Matsuda, K. Shimasaku, M. Iye, K. Ota, T. Shibuya, L. Jiang, Y. Taniguchi, and Y. Shioya, "A Lyα Emitter with an Extremely Large Rest-frame Equivalent Width of ˜900 Å at z = 6.5: A Candidate Population III-dominated Galaxy?" *ApJ*, vol. 761, p. 85, Dec. 2012.

[52] J. Mao, A. Lapi, G. L. Granato, G. de Zotti, and L. Danese, "The Role of the Dust in Primeval Galaxies: A Simple Physical Model for Lyman Break Galaxies and Lyα Emitters," *ApJ*, vol. 667, pp. 655–666, Oct. 2007.

[53] B. Fleming, K. France, R. E. Lupu, and S. R. McCandliss, "Spitzer Mapping of Polycyclic Aromatic Hydrocarbon and H_2 Features in Photodissociation Regions," *ApJ*, vol. 725, pp. 159–172, Dec. 2010.

[54] C. Leitherer, D. Schaerer, J. D. Goldader, R. M. González Delgado, C. Robert, D. F. Kune, D. F. de Mello, D. Devost, and T. M. Heckman, "Starburst99: Synthesis Models for Galaxies with Active Star Formation," *ApJS*, vol. 123, pp. 3–40, Jul. 1999.

[55] D. J. Schlegel, D. P. Finkbeiner, and M. Davis, "Maps of Dust Infrared Emission for Use in Estimation of Reddening and Cosmic Microwave Background Radiation Foregrounds," *ApJ*, vol. 500, p. 525, Jun. 1998.

[56] M. L. McCall, P. M. Rybski, and G. A. Shields, "The chemistry of galaxies. I - The nature of giant extragalactic H II regions," *ApJS*, vol. 57, pp. 1–62, Jan. 1985.

[57] H. Atek, D. Kunth, D. Schaerer, J. M. Mas-Hesse, M. Hayes, G. Ostlin, J.-P. Kneib, and ., "On the influence of physical galaxy properties on Lyman-alpha escape in star-forming galaxies," *ArXiv e-prints*, Aug. 2013.

[58] L. Mattsson and N. Bergvall, "Correcting emission line data in the SDSS for underlying stellar absorption," in *IAU Symposium*, ser. IAU Symposium, J. Andersen, Nordströara, B. m, and J. Bland-Hawthorn, Eds., vol. 254, Mar. 2009, p. 44P.

[59] G. Bruzual A., "Spectral evolution of galaxies. I - Early-type systems," *ApJ*, vol. 273, pp. 105–127, Oct. 1983.

[60] M. L. Balogh, S. L. Morris, H. K. C. Yee, R. G. Carlberg, and E. Ellingson, "Differential Galaxy Evolution in Cluster and Field Galaxies at z˜0.3," *ApJ*, vol. 527, pp. 54–79, Dec. 1999.

[61] L. J. Kewley and S. L. Ellison, "Metallicity Calibrations and the Mass-Metallicity Relation for Star-forming Galaxies," *ApJ*, vol. 681, pp. 1183–1204, Jul. 2008.

[62] G. Worthey and D. L. Ottaviani, "H gamma and H delta Absorption Features in Stars and Stellar Populations," *ApJS*, vol. 111, p. 377, Aug. 1997.

[63] M. Pettini and B. E. J. Pagel, "[OIII]/[NII] as an abundance indicator at high redshift," *MNRAS*, vol. 348, pp. L59–L63, Mar. 2004.

[64] L. J. Kewley and M. A. Dopita, "Using Strong Lines to Estimate Abundances in Extragalactic H II Regions and Starburst Galaxies," *ApJS*, vol. 142, pp. 35–52, Sep. 2002.

[65] J. A. Baldwin, M. M. Phillips, and R. Terlevich, "Classification parameters for

the emission-line spectra of extragalactic objects," *PASP*, vol. 93, pp. 5–19, Feb. 1981.

[66] S. Charlot and M. Longhetti, "Nebular emission from star-forming galaxies," *MNRAS*, vol. 323, pp. 887–903, May 2001.

[67] J. Brinchmann, S. Charlot, S. D. M. White, C. Tremonti, G. Kauffmann, T. Heckman, and J. Brinkmann, "The physical properties of star-forming galaxies in the low-redshift Universe," *MNRAS*, vol. 351, pp. 1151–1179, Jul. 2004.

[68] U.-L. Pen, "Analytical Fit to the Luminosity Distance for Flat Cosmologies with a Cosmological Constant," *ApJS*, vol. 120, pp. 49–50, Jan. 1999.

[69] B. E. J. Pagel, M. G. Edmunds, D. E. Blackwell, M. S. Chun, and G. Smith, "On the composition of H II regions in southern galaxies. I - NGC 300 and 1365," *MNRAS*, vol. 189, pp. 95–113, Oct. 1979.

[70] C. A. Tremonti, T. M. Heckman, G. Kauffmann, J. Brinchmann, S. Charlot, S. D. M. White, M. Seibert, E. W. Peng, D. J. Schlegel, A. Uomoto, M. Fukugita, and J. Brinkmann, "The Origin of the Mass-Metallicity Relation: Insights from 53,000 Star-forming Galaxies in the Sloan Digital Sky Survey," *ApJ*, vol. 613, pp. 898–913, Oct. 2004.

[71] M. Ando, K. Ohta, I. Iwata, C. Watanabe, N. Tamura, M. Akiyama, and K. Aoki,

"Lyman Break Galaxies at z˜5: Rest-Frame Ultraviolet Spectra," *ApJ*, vol. 610, pp. 635–641, Aug. 2004.

[72] C. Tapken, I. Appenzeller, S. Noll, S. Richling, J. Heidt, E. Meinköhn, and D. Mehlert, "Lyα emission in high-redshift galaxies," *AAp*, vol. 467, pp. 63–72, May 2007.

[73] S. R. McCandliss, K. France, P. D. Feldman, K. Glazebrook, G. Meurer, L. Bianchi, H. W. Moos, J. W. Kruk, W. P. Blair, and I. Baldry, "FORTIS: pathfinder to the Lyman continuum," in *Society of Photo-Optical Instrumentation Engineers (SPIE) Conference Series*, ser. Society of Photo-Optical Instrumentation Engineers (SPIE) Conference Series, G. Hasinger & M. J. L. Turner, Ed., vol. 5488, Oct. 2004, pp. 709–718.

[74] M. J. Li, N. Acuna, E. Amatucci, M. Beamesderfer, R. A. Boucarut, S. Babu, S. Bajikar, A. J. Ewin, R. Fettig, D. E. Franz, L. Hess, R. Hu, M. D. Jhabvala, D. Kelly, T. T. King, G. Kletetschka, C. A. Kotechi, A. Kutyrev, J. P. Loughlin, B. A. Lynch, H. Moseley, B. Mott, B. Newell, L. Oh, D. A. Rapchun, C. Ray, C. Sappington, E. Schulte, S. Schwinger, W. Smith, S. Snodgrass, L. M. Sparr, R. Steptoe-Jackson, L. L. Wang, Y. Zheng, and C. A. Zincke, "Microshutter array development for the James Webb space telescope," in *Society of Photo-Optical Instrumentation Engineers (SPIE) Conference Series*, ser. Society of

Photo-Optical Instrumentation Engineers (SPIE) Conference Series, J.-C. Chiao, D. N. Jamieson, L. Faraone, & A. S. Dzurak, Ed., vol. 5650, Feb. 2005, pp. 9–16.

[75] B. W. Ballard, R. Barkhouser, B. Kean, Jr., and M. Romelfanger, "The Hopkins Ultraviolet Telescope Engineering Report for the Astro-2 Mission," Tech. Rep., Sep. 1995.

[76] S. R. McCandliss, K. France, P. D. Feldman, and R. Pelton, "Long-slit imaging dual-order spectrograph: LIDOS," in *Society of Photo-Optical Instrumentation Engineers (SPIE) Conference Series*, ser. Society of Photo-Optical Instrumentation Engineers (SPIE) Conference Series, J. C. Blades & O. H. W. Siegmund, Ed., vol. 4854, Feb. 2003, pp. 385–396.

[77] W. G. Fastie and D. E. Kerr, "Spectroradiometric calibration techniques in the far ultraviolet - A stable emission source for the Lyman bands of molecular hydrogen," *Applied Optics*, vol. 14, pp. 2133–2142, Sep. 1975.

[78] G. Reichardt and F. Schäfers, "Laminar versus trapezoidal grating profiles: AFM measurements and efficiency simulations [3150-16]," in *Society of Photo-Optical Instrumentation Engineers (SPIE) Conference Series*, ser. Society of Photo-Optical Instrumentation Engineers (SPIE) Conference Series, W. R. McKinney and C. A. Palmer, Eds., vol. 3150, 1997, p. 121.

[79] O. Siegmund, J. Vallerga, A. Tremsin, and J. McPhate, "Microchannel plates: recent advances in performance," in *Society of Photo-Optical Instrumentation*

Engineers (SPIE) Conference Series, ser. Society of Photo-Optical Instrumentation Engineers (SPIE) Conference Series, vol. 6686, Sep. 2007.

[80] J. V. Vallerga, J. B. McPhate, A. P. Martin, G. A. Gaines, O. H. Siegmund, E. Wilkinson, S. Penton, and S. Beland, "HST-COS far-ultraviolet detector: final ground calibration," in *Society of Photo-Optical Instrumentation Engineers (SPIE) Conference Series*, ser. Society of Photo-Optical Instrumentation Engineers (SPIE) Conference Series, O. H. Siegmund, S. Fineschi, and M. A. Gummin, Eds., vol. 4498, Dec. 2001, pp. 141–151.

[81] M. J. Li, A. D. Brown, A. S. Kutyrev, H. S. Moseley, and V. Mikula, "JWST microshutter array system and beyond," in *Society of Photo-Optical Instrumentation Engineers (SPIE) Conference Series*, ser. Society of Photo-Optical Instrumentation Engineers (SPIE) Conference Series, vol. 7594, Feb. 2010.

[82] E. B. Burgh, S. R. McCandliss, R. Pelton, K. France, and P. D. Feldman, "Windowless vacuum ultraviolet collimator," in *Society of Photo-Optical Instrumentation Engineers (SPIE) Conference Series*, ser. Society of Photo-Optical Instrumentation Engineers (SPIE) Conference Series, O. H. Siegmund, S. Fineschi, and M. A. Gummin, Eds., vol. 4498, Dec. 2001, pp. 296–302.

[83] L. Colina, M. L. Garcia Vargas, J. M. Mas-Hesse, A. Alberdi, and A. Krabbe, "Nuclear Spiral and Ring Star-forming Structures and the Starburst–Active

Galactic Nucleus Connection in Barred Spirals NGC 3351 and NGC 4303," *ApJL*, vol. 484, p. L41, Jul. 1997.

[84] E. Schinnerer, W. Maciejewski, N. Scoville, and L. A. Moustakas, "Toward the Secondary Bar: Gas Morphology and Dynamics in NGC 4303," *ApJ*, vol. 575, pp. 826–844, Aug. 2002.

[85] R. A. Koopmann and J. D. P. Kenney, "Hα Morphologies and Environmental Effects in Virgo Cluster Spiral Galaxies," *ApJ*, vol. 613, pp. 866–885, Oct. 2004.

[86] V. Cayatte, J. H. van Gorkom, C. Balkowski, and C. Kotanyi, "VLA observations of neutral hydrogen in Virgo Cluster galaxies. I - The Atlas," *AJ*, vol. 100, pp. 604–634, Sep. 1990.

[87] E. Jiménez-Bailón, M. Santos-Lleó, J. M. Mas-Hesse, M. Guainazzi, L. Colina, M. Cerviño, and R. M. González Delgado, "Nuclear Activity and Massive Star Formation in the Low-Luminosity Active Galactic Nucleus NGC 4303: Chandra X-Ray Observations," *ApJ*, vol. 593, pp. 127–141, Aug. 2003.

[88] D. E. Osterbrock, *Astrophysics of gaseous nebulae and active galactic nuclei*, 1989.

[89] S. R. McCandliss, K. France, S. Osterman, J. C. Green, J. B. McPhate, and E. Wilkinson, "Far-Ultraviolet Sensitivity of the Cosmic Origins Spectrograph," *ApJL*, vol. 709, pp. L183–L187, Feb. 2010.

Vita

Brian Fleming received B.S. degrees in Aerospace Engineering and Physics from the Illinois Institute of Technology in 2005. He enrolled in the PhD program at Johns Hopkins in 2006 along with his wife, who he met as an undergraduate. During their time as graduate students they have had two children while managing an often-times chaotic work-life balance. Brian has been interested in the design and construction of space vehicles and systems since he was a child, and has paper records outlining his desire to be either an Astrophysicist (which I think he thought meant Astronaut), a jet pilot, or a teacher going all the way back to 1989. In addition to dreaming about space, Brian is also an avid hiker, fisherman, and nature enthusiast. He hopes that someday he can find his way back to his home state of Alaska. Until then, Brian will be moving to a post-doctoral research position at the University of Colorado.